

Development of Radiotracers for Neuroimaging

Niral Patel

Submitted for the degree of Doctor of Philosophy

Department of Medical Physics and Biomedical Engineering

University College London

Declaration

I, Niral Patel, confirm that the work presented in this thesis is my own. Where information has been derived from other sources, I confirm that this has been referenced accordingly. This thesis is based on research conducted between September 2011 to May 2014 at the Chemistry Department and Centre for Advanced Biomedical Imaging (CABI), University College London, U.K.

Niral Patel

Abstract

Nuclear imaging enables quantitative measurements of biological processes *in vivo* and has revolutionised biomedical research, drug development and clinical practice. Despite the advances made in this field, the ability to image fundamental aspects of neurological diseases remains a challenge. This is partly due to the limited availability of radiotracers for imaging excitatory neurotransmission and detection of inflammation as well as an array of other biochemical processes central to the operational function of the brain. The aim of this research was to expand the arsenal of radiotracers available for neuroimaging in order to study key pathological processes involved in neurological diseases.

With the aim to target neuronal Voltage Gated Sodium Channels (VGSCs), Vascular Cell Adhesion Molecule – 1 (VCAM-1) and N-methyl-D-Aspartate Receptors (NMDARs), radiotracers have been synthesised and evaluated. Abnormal expression of these receptors has been implicated in a number of pathological conditions including epilepsy, multiple sclerosis and neurodegeneration. The radiotracers were characterised and evaluated via *in vivo* imaging (MRI and SPECT/CT) and *ex-vivo* studies (phosphorimaging, biodistribution and metabolite analysis) in order to determine if they hold significant potential as tools to study neuronal pathways as well as for diagnostic imaging and treatment monitoring.

Iodinated analogues of the iminodihydroquinoline WIN17317-3, and the 1-benzazepin-2-one BNZA have been evaluated as neuronal VGSC tracer candidates in healthy mice. Whilst the WIN17317-3 analogue suffered from poor brain uptake and was rapidly metabolised *in vivo*, the BNZA analogue exhibited excellent *in vivo* stability and its promising uptake in the brain warrants further investigations.

Even though *N*-(1-Naphthyl)-*N'*-(3-[¹²³I]-iodophenyl)-*N'*-methylguanidine ([¹²³I]CNS-1261) has demonstrated favourable pharmacokinetics for brain imaging in clinical studies, [¹²⁵I]CNS-1261 was not successful in discriminating NMDAR expression between naïve rats and those induced with status epilepticus using lithium and pilocarpine.

Promisingly, a multi modal contrast agent comprising micron sized particles of iron oxide conjugated to I-125 radiolabelled antibodies, highlighted the up-regulation of VCAM-1 in rat models of cerebral inflammation and in the lithium pilocarpine model of status epilepticus. This versatile imaging agent presents an exciting opportunity to identify an early biomarker for epileptogenesis.

Acknowledgements

I would like to begin by acknowledging the invaluable support of my supervisors: Erik Årstad has been an inspiration due to his breadth of knowledge and my accomplishments over the last 4 years would not have been possible without his guidance; I am indebted to Adam Badar for teaching me about biological evaluations and for ongoing support both academically and personally; and Mark Lythgoe whose passion fostered an incredible environment for learning and for wonderful insight that has driven my research.

Many people have also actively contributed to the work contained within this thesis and therefore their help is greatly appreciated: Carlos Perèz-Medina for help with radiolabelling, Eva Galante for assistance with HPLC and LC-MS, Ben Duffy for teaching me the animal models and collaborating on a VCAM-1 project, Mathew Robson, Valerie Taylor and Asif Machhada for help with animal models and radiotracer administrations, Abil Aliev for help with NMR acquisition and Vineeth Rajkumar for help with phosphorimaging. I am also thankful to Kerstin Sander, Ran Yan, Thibault Gendron and Tammy Kalber for their in depth discussions and advice.

I wish to thank the people who have surrounded me during my years at UCL: Vincent Gray and Rachel Lannigan from the Chemistry department: Vessela Vassileva from the Cancer Institute and the past and current members of CABI: Adrienne Campbell, Angela D'Esposito, Ben Duffy, Bernard Siow, Daniel Stuckey, Holly Holmes, Isabel Christie, Jack Wells, James O'Callaghan, Johannes Riegler, Katherine Ordidge, Laurence Jackson, Louise Kiru, Miguel Goncalves, Morium Ali, Ozama Ismail, Peter Johnson, Ruth Oliver, Rupinder Ghatrora, Simon Walker-Samuel, Thomas Roberts and Yanan Zhu.

My close friends have been a great support system and I wish to thank them dearly: Rajiv Ramasawmy for introducing me to your uniqueness and creative outlook on life, Carlos Perèz-Medina for always inspiring me, Elena Yiannaki for sharing this PhD journey with me through tears and laughter and Anthony Price for encouraging me throughout. Also, Ahmed Akhbar, Atif Elahi and Bhavesh Premdjee have been the best friends whose love and support I will always cherish.

Finally, my deepest gratitude goes to my family who have been my backbone and whose unconditional love and support have allowed me to achieve this.

Table of Contents

Abstract	3
Acknowledgements	5
List of Figures	11
List of Tables	12
List of Schemes	12
List of Equations	13
Abbreviations	14
Publications arising from this thesis	17
Conference Poster	17
Conference Presentation	17
Thesis Outline	18
Chapter 1 Introduction	19
1.1 Nuclear Imaging.....	19
1.1.1 SPECT.....	20
1.1.2 PET	22
1.1.3 PET vs. SPECT, Clinical vs. Pre-Clinical.....	24
1.1.4 Autoradiography and Phosphorimaging	26
1.2 Radiotracers	27
1.2.1 Radionuclides.....	27
1.2.2 Isotopes and Radioisotopes of Iodine	28
1.2.3 Pharmacokinetics	29
1.3 Radiotracer Development	36
1.4 Radiotracers for Neuroimaging.....	38
1.5 Summary	39
Chapter 2 Experimental Methods for Radiolabelling and Quantitative Analysis	40
2.1 Radiolabelling with Iodine.....	40
2.1.1 Radioiodination of Small Organic Molecules.....	43
2.2 Radio - High Performance Liquid Chromatography.....	44
2.3 Specific Activity	46
2.4 Quantitative Accuracy for Imaging.....	47
2.4.1 <i>In Vivo</i> SPECT	47

2.4.2 Phosphorimaging	50
2.4.3 Biodistribution	51
2.5 Summary	52
Chapter 3 Evaluation of Voltage Gated Sodium Channel Blockers for Imaging with SPECT and PET	53
3.1 Aim and Hypothesis.....	53
3.2 Sodium Channels	53
3.2.1 Structure and Function	53
3.2.2 VGSCs in Disease	56
3.3 VGSC Blockers.....	58
3.4 Benzazepinone Derived VGSC Blocker for SPECT Imaging	61
3.4.1 BNZA.....	61
3.4.2 Results	62
3.4.3 Discussion	67
3.5 Evaluation of an Iminodihydroquinoline Tracer for Imaging of VGSCs	72
3.5.1 WIN17317-3	72
3.5.2 Results.....	73
3.5.3 Discussion	77
3.6 Conclusion	78
Chapter 4 Multimodal Imaging of Neuroinflammation	79
4.1 Aims and Hypothesis	79
4.2 Neuroinflammation	79
4.3 Study Outline	81
4.4 Results.....	82
4.4.1 Conjugation Radiochemistry.....	82
4.4.2 Blood Clearance and Biodistribution.....	83
4.4.3 Dose Optimisation.....	84
4.4.4 Qualitative Comparison of MRI, SPECT/CT and Phosphorimaging	85
4.4.5 Quantitative Comparison of MRI and SPECT.....	86
4.4.6 Distribution of [¹²⁵ I]VCAM-MPIO within the Brain Vasculature	89
4.5 Discussion.....	90
4.6 Conclusion	93
Chapter 5 Multimodal Imaging of Seizure-Induced Inflammation	95
5.1 Aim and Hypothesis.....	95

5.2 Epilepsy.....	95
5.2.1 Status Epilepticus.....	97
5.2.2 Animal Models.....	98
5.3 Neuroimaging the Epileptogenic Process	100
5.4 Study Outline	102
5.5 Results.....	103
5.6 Discussion.....	106
5.7 Conclusion	108
Chapter 6 Synthesis and Evaluation of [¹²⁵I]CNS-1261 for Targeting Activated NMDA Receptors	109
6.1 Aim and Hypothesis.....	109
6.2 NMDA Receptors	109
6.3 [¹²⁵ I]CNS-1261.....	112
6.4 Study Outline	113
6.4.1 Animal Model.....	113
6.4.2 Phosphorimaging	114
6.4.3 Phosphorimaging Quantification	114
6.5 Results.....	115
6.5.1 Radiolabelling.....	115
6.5.2 Animal Model.....	118
6.5.3 Phosphorimaging	118
6.6 Discussion.....	119
6.6.1 Radiochemistry	119
6.6.2 Phosphorimaging	120
6.7 Conclusion	121
Chapter 7 Summary and Further Work.....	122
Chapter 8 Materials and Methods.....	127
8.1 Chemistry.....	127
8.1.1 3-azido-4,5-dihydro-1H-benzo[b]azepin-2(3H)-one	127
8.1.2 3-amino-4,5-dihydro-1H-benzo[b]azepin-2(3H)-one	128
8.1.3 3-(tritylamino)-4,5-dihydro-1H-benzo[b]azepin-2(3H)-one.....	129
8.1.4 Propane-1,3-diyl dimethane sulfonate	130
8.1.5 Attempts to synthesise the precursor for ¹⁸ F- Radiolabelling	130
8.1.6 VCAM-MPIO.	132

8.2 Radiochemistry	132
8.2.1 Radioiodinated BNZA Analogue.....	133
8.2.2 [¹²⁵ I]VCAM-MPIO	134
8.2.3 [¹²⁵ I]CNS- 1261 ([¹²⁵ I]19)	134
8.3 Biological Evaluations	136
8.3.1 General.....	136
8.3.2 Radioiodinated BNZA and WIN17317-3 Analogues	138
8.3.3 [¹²⁵ I]VCAM-MPIO	140
8.3.4 [¹²⁵ I]CNS-1261	143
References.....	144

List of Figures

Figure 1. The detection of gamma rays in SPECT.....	21
Figure 2. The processing of detected gamma rays.	22
Figure 3. Coincident detection in PET.	23
Figure 4. Spatial resolution across clinical and pre-clinical PET and SPECT scanners.....	24
Figure 5. Comparison of multi-pinhole and parallel-hole collimators.....	25
Figure 6. A two compartment model representing the influence of plasma protein binding on drug distribution.	33
Figure 7. Graph of bound versus free drug showing relationship between K_d and B_{max}	34
Figure 8. The process of radiotracer development.....	37
Figure 9. The chemical structure of Iodogen™.	41
Figure 10. Radioiodination of proteins using pre-coated iodination tubes.....	42
Figure 11. Schematic representation of HPLC.	45
Figure 12. Graphical representation of the FWHM.	48
Figure 13. Quantification phantoms used for rat and mouse apertures on the SPECT/CT scanner.....	50
Figure 14. Results of the gamma counter after normalisation.....	52
Figure 15. Conformational states of VGSCs.	54
Figure 16. Structural representation of VGSCs.	55
Figure 17. Structures of VGSC blockers.....	60
Figure 18. Structure of BNZA and one of its analogues.....	61
Figure 19. HPLC chromatograms for the synthesis of [125 I] 4	63
Figure 20. HPLC radioactivity profiles of plasma and brain samples after [125 I] <i>h-4</i> injection	66
Figure 21. SPECT/CT images showing the distribution of [125 I] 4	67
Figure 22. BNZA and its derivatives evaluated <i>in vitro</i>	68
Figure 23. A possible product formed in the attempts to obtain a precursor for 18 F radiolabelling.	72
Figure 24. HPLC radioactivity profiles of plasma samples after [125 I] 17 administration.....	76
Figure 25. SPECT/CT image showing the distribution of [125 I] 17	76
Figure 26. Blood clearance and biodistribution of [125 I]VCAM-MPIO.....	83
Figure 27. Dose optimisation studies of [125 I]VCAM-MPIO for <i>in vivo</i> imaging.	85
Figure 28. Multimodal imaging of VCAM-1 expression.	86
Figure 29. Illustration of the procedure for MRI quantification.	86
Figure 30. 3-D representation and quantitation of CA binding..	88

Figure 31. Dynamic SPECT following administration of the CA.	89
Figure 32. CA distribution within the brain vasculature.	90
Figure 33. The stages of epileptogenesis following SE.	97
Figure 34. Structures of radiotracers used for imaging TSPO expression in epilepsy patients.	102
Figure 35. Evaluation of [¹²⁵ I]VCAM-MPIO in the lithium -pilocarpine model of SE.....	104
Figure 36. Bimodal <i>in vivo</i> imaging of seizure induced inflammation.	105
Figure 37. The distribution of the CA assessed by phosphorimaging.	105
Figure 38. Dynamic SPECT following administration of the CA in seizure induced rats.	106
Figure 39. Representation of NMDA receptors.	110
Figure 40. Representation of ROIs selected for quantification of phosphorimaging signals.	114
Figure 41. Analytical Radio-HPLC chromatograms for the radiolabelling of CNS-1261.....	117
Figure 42. Quantification of the phosphorimaging signals.....	119
Figure 43. Polymerisation of VCAM-MPIO.....	124

List of Tables

Table 1. The properties of common SPECT and PET radioisotopes.	29
Table 2. VGSC subtypes located throughout the body.	56
Table 3. Biodistribution of [¹²⁵ I]h-4 and [¹²⁵ I]l-4.....	65
Table 4. Biodistribution of [¹²⁵ I]17.	75
Table 5. Analytical radiochemical yields (RCY) for the radiolabelling of CNS-1261.....	116

List of Schemes

Scheme 1. (Radio)iodination of tyrosine.	43
Scheme 2. (Radio)iodination of organotin compounds.	44
Scheme 3. Radiolabelling of the trimethyl tin precursor to obtain a radioiodinated derivative of BNZA.	62
Scheme 4. Retrosynthetic analysis to obtain [¹⁸ F]14.....	70
Scheme 5. Attempts to obtain the precursor for ¹⁸ F radiolabelling.	71
Scheme 6. ¹²⁵ I Radiolabelling of WIN17317-3.....	73
Scheme 7. Radiolabelling of the tributyl tin precursor to obtain [¹²⁵ I]CNS-1261	115
Scheme 8.....	127
Scheme 9.....	128

Scheme 10.....	129
Scheme 11.....	130
Scheme 12.....	130
Scheme 13.....	131
Scheme 14.....	132
Scheme 15.....	133
Scheme 16.....	135

List of Equations

Equation 1	23
Equation 2	30
Equation 3	32
Equation 4	33
Equation 5	34
Equation 6	34
Equation 7	35
Equation 8	35

Abbreviations

2D	Two - Dimensional
3D	Three - Dimensional
ach	anterior choroidal arteries
AED	Anti-Epileptic Drug
AMPA	α -amino-3-hydroxy-5-methyl-4-isoxazolepropionate
astr	anterior striate arteries
AUC	Area Under Curve
BBB	Blood Brain Barrier
BOC	<i>tert</i> -butyloxycarbonyl
BP	Binding Potential
BTX	Batrachotoxin
CA	Contrast Agent
CB ₁	Cannabinoid subtype 1
cBZR	central Benzodiazepine Receptor
CHO	Chinese Hamster Ovary Cells
CNS	Central Nervous System
CPM	Counts Per Minute
CSE	Convulsive Status Epilepticus
CT	Computerised Tomography
DCM	Dichloromethane
DMF	Dimethylformamide
DMSO	Dimethyl Sulfoxide
EAE	Experimental Autoimmune Encephalomyelitis
EEG	Electroencephalography
FDG	Fluorodeoxyglucose
FOV	Field of View
FWHM	Full Width at Half Maximum
GABA (A)	Gamma-Amino butyric Acid type A
HE	Hematoxylin and Eosin
HMBG-1	High Mobility Group Box protein 1
HPLC	High Performance Liquid Chromatography

HS	Hippocampal Sclerosis
[¹²⁵ I]CNS-1261	<i>N</i> -(1-Naphthyl)- <i>N'</i> -(3-[¹²⁵ I]-iodophenyl)- <i>N''</i> -methylguanidine
ID	Injected Dose
IgG	Immunoglobulin G
Il-1β	Interleukin-1β
Iodogen	1,3,4,6-tetrachloro-3α, 6α-diphenylglycouril
i.p	Intraperitoneal
i.v	Intravenous
KA	Kainic Acid
LC-MS	Liquid Chromatography- Mass Spectrometry
LG	Leaving Group
Log D	Distribution coefficient
Log P	Partition coefficient
MES	Maximal Electroshock
MK-801	Dizocilpine
MPIO	Micron Sized Particles of Iron Oxide
MRI	Magnetic Resonance Imaging
MS	Multiple Sclerosis
MsCl	Methanesulfonyl Chloride
NCX	Sodium Calcium Exchanger
NIS	Sodium Iodide Symporter
NMDA	<i>N</i> -methyl- <i>D</i> -aspartate
NMR	Nuclear Magnetic Resonance
Nu	Nucleophile
PBR	Peripheral benzodiazepine receptor
PBS	Phosphate-buffered saline
PET	Positron Emission Tomography
PFA	Paraformaldehyde
PMTs	Photomultiplier Tubes
PPM	Parts Per Million
RCY	Radiochemical yield
ROI	Region of Interest
RT	Room Temperature

SA	Specific Activity
scol	Supracollicular network
SD	Standard Deviation
SE	Status Epilepticus
SEM	Standard Error of the Mean
SNR	Signal-to-Noise Ratio
SPECT	Single Photon Emission Computed Tomography
SRS	Spontaneous Recurrent Seizures
SUV	Standardised Uptake Value
TEA	Triethylamine
TFA	Trifluoroacetic acid
TLE	Temporal Lobe Epilepsy
TNF- α	Tumour Necrosis Factor - alpha
tosyl	p-Toluenesulfonyl
trhi	Transverse hippocampal arteries
TsCl	Toluenesulfonyl Chloride
TSPO	Translocator Protein
TTX	Tetrodotoxin
UV	Ultraviolet
VCAM-1	Vascular Cell Adhesion Molecule-1
VGSCs	Voltage Gated Sodium Channels

Publications arising from this thesis

1. Perèz-Medina C, **Patel N**, Robson M, Badar A, Lythgoe M F, Årstad E. ‘Evaluation of a ^{125}I -labelled Benzazepinone Derived Voltage-Gated Sodium Channel Blocker for Imaging With SPECT’, *Org. Biomol. Chem.* **2012**, (10), 9474 – 9480
2. Perèz-Medina C, **Patel N**, Robson M, Lythgoe M F, Årstad E. ‘Synthesis and Evaluation of a ^{125}I -labelled Iminodihydroquinoline-Derived Tracer for Imaging of Voltage-Gated Sodium Channels’, *Bioorg. Med. Chem. Lett.* **2013**, (23), 5170 – 5173
3. **Patel N**, Duffy B, Badar A, Lythgoe M F, Årstad E. ‘Multimodal Imaging of Neuroinflammation with SPECT/CT and MRI using VCAM-1 Antibody – Microparticle Conjugates Labelled with Iodine-125’

Conference Poster

1. **Patel N**, Duffy B, Badar A, Lythgoe M F, Årstad E. ‘Bimodal Imaging of Inflammation with SPECT and MRI using ^{125}I -labelled VCAM-1 Antibody – Nanoparticle Conjugates’, World Molecular Imaging Congress, **2012**, Dublin

Conference Presentation

1. **Patel N**, Duffy B, Badar A, Lythgoe M F, Årstad E. ‘Bimodal Imaging of Inflammation with SPECT and MRI using ^{125}I -labelled VCAM-1 Antibody – Nanoparticle Conjugates’, European Molecular Imaging Meeting, **2014**, Antwerp

Thesis Outline

The focus of this thesis is on the development and evaluation of radiotracers for neuroimaging in order to increase our understanding of key pathological processes involved in neurological diseases. The emphasis is on identifying early biomarkers for diagnosis and treatment monitoring. In chapter 1, the basic principles of nuclear imaging and radiotracer development are introduced, with focus on the properties to which radiotracers must adhere to successfully target the brain. Chapter 2 begins with a brief discussion on the factors governing purity and yields in radiochemical reactions, and the mechanisms underlying radio-iodination of chemical moieties. The second part of chapter 2 details the experimental methods by which imaging systems were calibrated to allow for accurate quantification of the signals detected. In chapter 3, the focus is on two radiotracers for imaging of neuronal VGSC expression. Inspired by the results from one of these radiotracers, the attempts to synthesise a fluorinated derivative are discussed in the latter part of chapter 3. In the subsequent chapter, the synthesis of a radiolabelled VCAM-1 targeting iron oxide particle is discussed. The ability of this probe to image VCAM-1 expression in a rat model of cerebral inflammation (chapter 4) and in the lithium pilocarpine model of status epilepticus (chapter 5) is described. To study the interplay between neuroinflammation and dysfunction of fast neurotransmission in diseases of the brain, the suitability of [¹²⁵I]CNS-1261 to detect changes in expression of NMDA receptors between healthy rats and those that have been induced with (status epilepticus) seizures has been investigated (chapter 6). The overall results have been summarized in chapter 7 and ideas have been presented for future endeavors. The experimental methods conducted as part of this research are outlined in chapter 8.

Chapter 1 Introduction

In vivo imaging is a powerful tool to evaluate structure and function non-invasively in a living subject. Multiple techniques are available, which can be divided into two main groups: those that primarily provide structural information such as Magnetic Resonance Imaging (MRI) and Computerised Tomography (CT), and those that predominantly give functional and molecular information, for example Single Photon Emission Computed Tomography (SPECT) and Positron Emission Tomography (PET). Nuclear imaging, principally SPECT is the core imaging modality used in the work presented herein. In this chapter, the principles behind nuclear imaging and the process of radiotracer development are presented. The properties required for a brain targeting tracer are also described.

1.1 Nuclear Imaging

Nuclear imaging involves detection of radioactive materials to identify signatures of diseases and quantify biochemical processes and has been pivotal in:

- Improving the accuracy with which disease can be detected¹
- Determining the extent and severity of disease^{2, 3}
- Monitoring patient response to therapy^{3, 4}

The three principal nuclear imaging modalities are SPECT, PET, and Autoradiography/Phosphorimaging. Since the 1970s, X-Ray, CT and MRI dominated the imaging of human anatomy. Nonetheless, functional or metabolic changes do occur in the absence of a corresponding anatomical correlate. Therefore, nuclear imaging provides critical information that otherwise would be unavailable and require invasive surgery or more expensive diagnostic tests.⁵

Nuclear imaging provides information about the distribution of a radioactive tracer (radiotracer) over time and can importantly show how this distribution differs between physiological and pathological conditions. This can aid in understanding biochemical properties under certain conditions. It is also vital to identify the exact anatomic location of radiotracer distribution in order to determine the proper course

of therapy. The pioneering work of Hasegawa and colleagues in the late 1980s^{6, 7} set the stage for integrated SPECT/CT⁸, PET/CT⁹ and PET/MRI¹⁰ systems. Such complementary, bi-modal scanners make it possible to acquire both anatomical and functional images. However in most systems, simultaneous acquisition of the anatomy and radiotracer distribution is not feasible. This means that artefacts can arise from patient movement between the two sets of scans.

With the advancements in imaging technology, it is now possible to image the distribution of picomolar amounts of radiotracers.¹¹ Therefore, SPECT and PET are highly sensitive techniques which are distinguished by the detection principles of gamma rays emitted, either when radioactive nuclei decay (SPECT) or from an annihilation event (PET).¹² Radioactive decay is the process where unstable atomic nuclei spontaneously emit ionizing radiation. The unit of radioactivity is the *Becquerel* (Bq) and is defined as one nuclear disintegration per second (s^{-1}).

1.1.1 SPECT

Radionuclides used for SPECT decay by emitting (single photon) gamma rays that are measured directly by the scanner. Collimators, which are honeycomb shaped lead blocks, have small holes designed to allow only gamma rays with a parallel trajectory to pass through and reach the detector (Figure 1a). Gamma rays which deviate from a parallel trajectory are attenuated by the lead and remain undetected. The angle of the emitted gamma rays must fall within a small range for detection, thus SPECT cameras generally exhibit lower sensitivity compared to PET (section 1.1.2). The size and density of holes on the collimators can vary to suit particular imaging requirements: collimators with numerous small diameter holes (Figure 1b) produce images with higher resolution whilst larger diameter punctuations (Figure 1c) offer greater sensitivity.

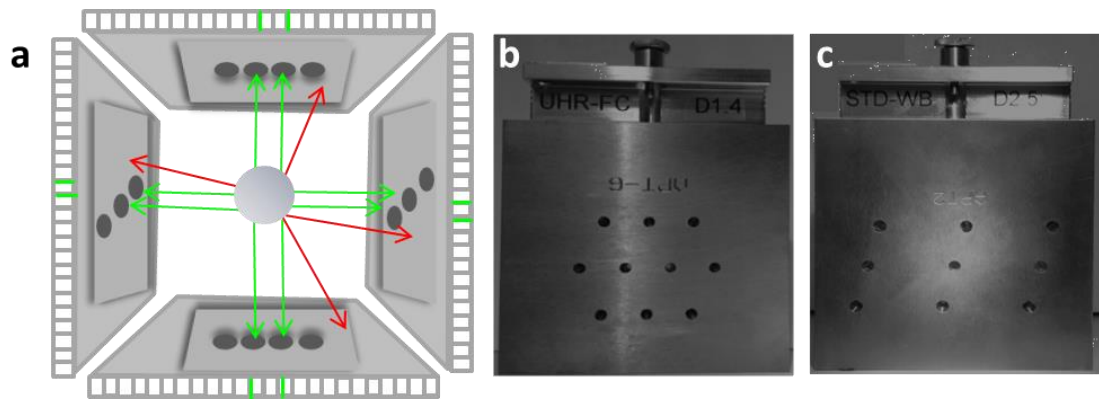


Figure 1. The detection of gamma rays in SPECT. Collimation detection (a): only gamma rays with a parallel trajectory (green) pass through the collimators and are detected. Gamma rays which deviate from a parallel trajectory (red) remain undetected. Collimators can be designed with numerous small diameter holes (b) or sparser large diameter holes (c) to provide higher resolution or offer greater sensitivity.

Gamma rays which pass through the collimators are detected by a solid state scintillator, which typically is a crystal structure that converts the energy of ionising radiation into light in the visible spectrum (scintillation). Different scintillator materials are used depending on the energy of the gamma rays detected as well as the speed required for processing. As the photon energies involved in SPECT are lower than PET, there is a wider range of materials that can be used for detector designs. For SPECT, gamma rays are best detected with crystals of thallium-activated sodium iodide which is dense enough to absorb energetic rays.¹² The energy of each gamma photon is absorbed by the scintillator which results in excitation of the crystal (an electron is removed from an iodine atom). Upon de-excitation (the dislocated electron finds a minimal energy state), the crystal re-emits the absorbed energy in the form of light where there is a direct correlation between the amount of light produced and the energy of the gamma ray absorbed. The scintillation photons are then processed through photomultiplier tubes (PMTs) which convert the light energy into electrical impulses, that become amplified to enable each radioactive decay event to be registered and measured (Figure 2). Initially, multiple 2-dimensional projections are acquired from various angles. These events are stored and the data subsequently fed into mathematical algorithms, which through a process called tomographic reconstruction, creates a 3-dimensional image of the radioactive spatial distribution in the field of view.

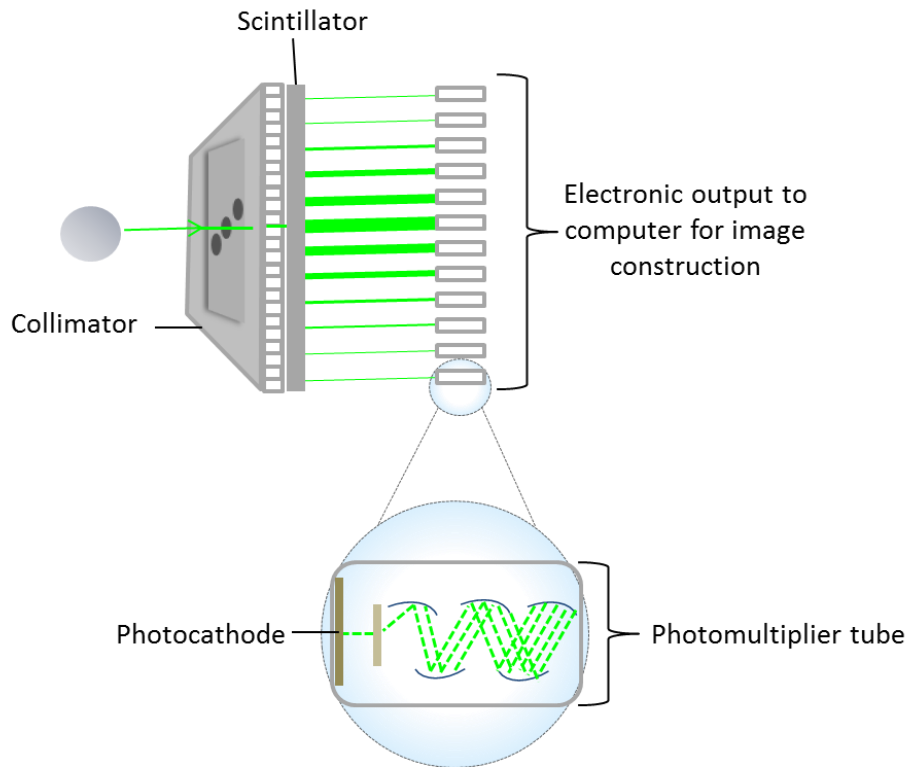


Figure 2. The processing of detected gamma rays. All PMTs simultaneously detect the (presumed) same flash of light from the scintillator. The intensity of the light detected at each PMT depends on its position from the actual incident event. The location of the incident event can be found by weighting the position of each PMT from the strength of its signal and a mean position is determined from the different locations and strengths of signals detected.

1.1.2 PET

Radionuclides used for PET decay by emitting a positron, which travels a short distance before annihilating with an electron. In doing so, the combined energy of the two particles is converted into two gamma rays that travel at 180° to each other. PET scanners consist of a circular array of detectors designed specifically to only detect linear pairs of gamma rays within a short time of each other (typically within 8 - 12 nanoseconds). Therefore, PET scanners produce images via coincidence detection (Figure 3). Gamma rays arising from positron annihilation are less prone to attenuation than gamma rays emitted by SPECT radionuclides due to their higher energies (511 KeV vs. 80 – 160 KeV). Once detected, the gamma rays undergo a similar process of signal processing and amplification as the SPECT signals described in section 1.1.1.

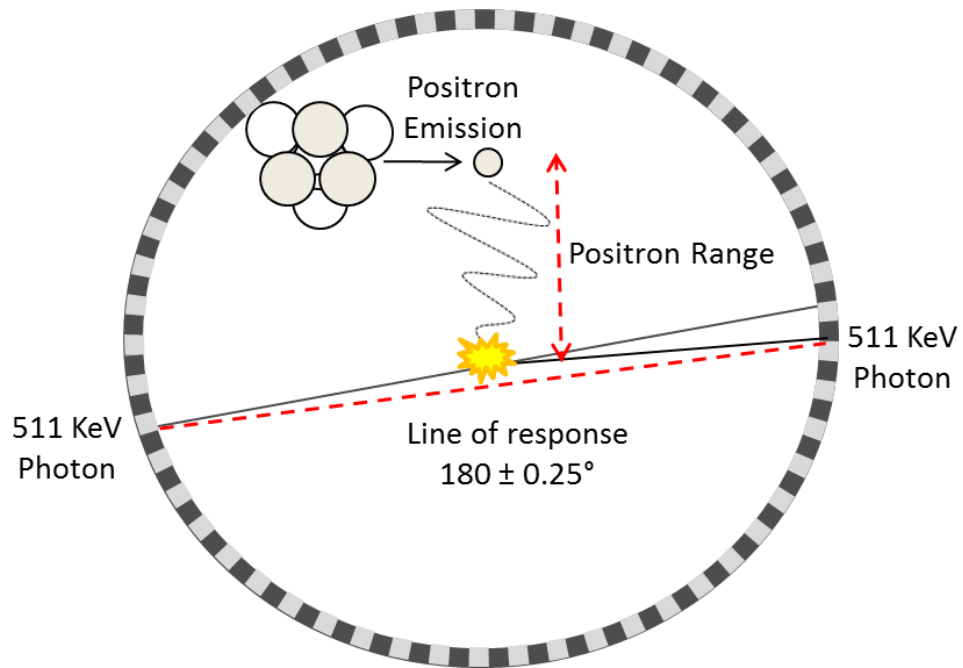


Figure 3. Coincident detection in PET. An emitted positron annihilates with an electron, creating two 511 KeV gamma rays. Represented are the finite positron range and the non-collinearity of the annihilation photons. For diagrammatic purposes, positron range and the angle between the two emitted photons have been to a great extent exaggerated.

Positron range is the distance from the site of positron emission to the annihilation site. PET scanners detect the annihilation photons which define the line of response as opposed to the location of the decaying radionuclide. Therefore, positrons which travel a longer distance will result in a higher degree of image blurring.

A positron and an electron are not completely at rest when they annihilate. The small net momentum of these particles means that the annihilated photons will not be exactly at 180° and this is referred to as non-collinearity. If the difference in the time of detection of these photons is smaller than a predetermined value (typically ≤ 12 ns) then the two detectors define a line of response. PET systems assume that gamma rays are emitted at exactly 180° , resulting in a small error in locating the point of annihilation. Blurring of images caused by non-collinearity can be estimated by:

$$\Delta_{nc} = 0.0022 \times D \quad \text{Equation 1}$$

Where D is the distance between the two coincidence detectors.

The annihilated photons travel towards the detectors positioned around the subject, where they get absorbed and produce an electrical signal. As mentioned, the absorbing material of the detector is important for determining the interaction probability and the accuracy by which the system can measure the photons energy and time of contact.¹³ Consequently, the materials commonly used for PET scintillators are bismuth germanate,¹⁴ lutetium oxyorthosilicate, or gadolinium orthosilicate due to their high γ -ray stopping power and speed of signal processing.

1.1.3 PET vs. SPECT, Clinical vs. Pre-Clinical

Spatial resolution and detection sensitivity are important performance characteristics for imaging systems.¹⁵ In general, clinical PET scanners offer superior spatial resolution compared to SPECT systems, whereas in the pre-clinical setting SPECT scanners display higher resolution capabilities compared to PET (Figure 4).¹⁶ This is mainly due to the fact that SPECT systems are not affected by physical limitations that hinder PET cameras to reach sub-millimetre ranges.

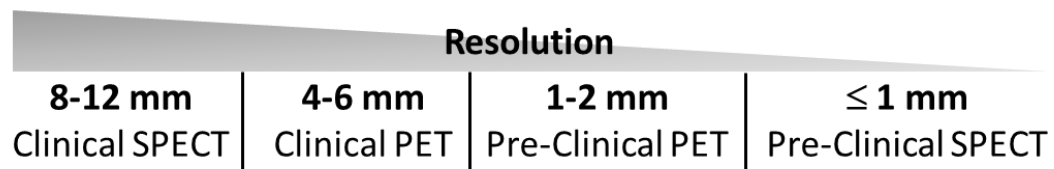


Figure 4. Spatial resolution across clinical and pre-clinical PET and SPECT scanners.

Many factors affect the quality of the final re-constructed PET images.¹⁷ These include the size of the crystal detectors, positron range, photon non-collinearity, the total number of events that occur during the acquisition time and the reconstruction algorithms. Photon range and non-collinearity (as represented in Figure 3) are complications not present in clinical and pre-clinical SPECT systems. Instead, SPECT gamma cameras rely on collimators to determine the gamma ray trajectory. In clinical systems that require imaging of a large patient, collimators typically have parallel holes. In contrast, small animal imaging requires substantially higher spatial resolution for a much smaller object, and this is achieved by pinhole collimators. As

a consequence, the imaging field of view and sensitivity of the system becomes compromised as a sufficient amount of radioactivity must pass through the small pinholes in order for the detected events to be transformed into images. Multiple pinholes can be used to achieve a reasonable trade-off between spatial resolution, sensitivity and FOV. Pinhole collimators magnify the object in the projection and hence improve the resolution in the object space, relative to the intrinsic resolution of the detector (Figure 5). The notion that SPECT is unique for magnification imaging is not entirely true. Specialised detectors could magnify PET images and this higher resolution imaging method may be in principle applied to human imaging.¹⁸

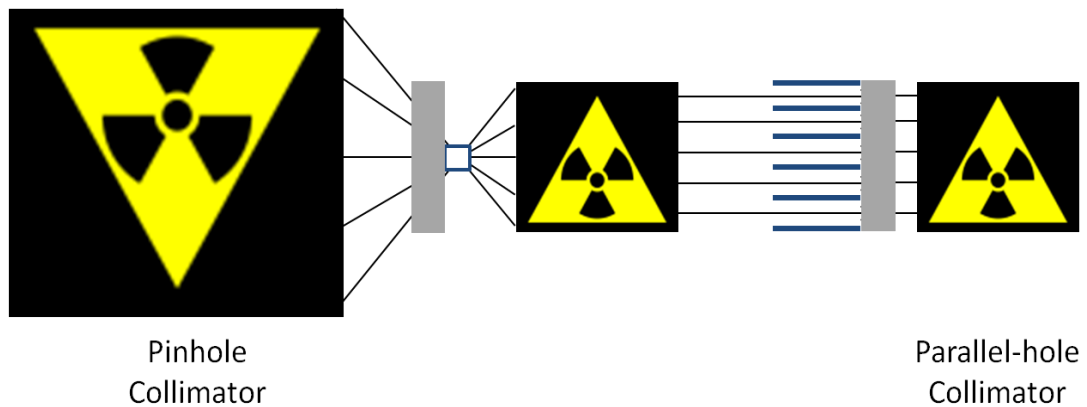


Figure 5. Comparison of multi-pinhole and parallel-hole collimators used in pre-clinical and clinical SPECT imaging. Pinhole collimators (left) generate magnified, inverted images.

Additional factors such as attenuation and scatter can degrade SPECT image quality and this is discussed in detail in chapter 2. The overall image quality in small animal imaging is affected to a lesser extent by these degrading factors as rodents for example mice, are much smaller (20 – 40 g) compared to humans (average 75 kg). This disparity is also one of the main reasons why small animal PET scanners offer greater resolution than their clinical counterparts: in PET scanners used for small animals, D in Equation 1 is generally smaller.

1.1.4 Autoradiography and Phosphorimaging

Whilst PET and SPECT show radioactivity distribution *in vivo*, autoradiography and phosphorimaging measure the distribution of radioactivity on tissue sections in two dimensions, *in vitro* or *ex vivo*. These imaging techniques can reach resolutions of less than 10 microns. Therefore, structures that are too small to be imaged *in vivo* can be assessed using these methods.

For autoradiography and phosphorimaging, the radioactive tissue or organ is cryo-sectioned with a thickness typically between 5 – 20 μM . These sectioned slices are mounted on glass slides and then exposed to either a photographic film (autoradiography) or a phosphorimaging screen.

Phosphorimaging screens are coated with photo-reactive phosphor crystals that are europium (Eu) activated barium fluorohalide compounds. Tissue sections containing radioactivity are apposed on the screen and the energy from the radioactive emissions is absorbed by the phosphor crystals. As a result, Eu^{2+} is oxidised to Eu^{3+} and the released electron is stored in the phosphor lattice.¹⁹ After the exposure period, the screen is scanned in a phosphor imager using a red laser. This releases the trapped electron, reducing Eu^{3+} back to Eu^{2+} and reemitting the stored energy as blue light. The intensity of the emitted light is proportional to the amount of radioactivity in the sample. The blue light is detected and processed by a photomultiplier tube and the data are stored as a digital image of the locations and intensities of the radioactivity in the sample.

The resulting image is then analysed using dedicated software programmes, and if a set of radioactive standards are included with the tissue samples, the amount of radioactivity within discrete regions of the image can be quantified. Further details of how this is performed are outlined in chapter 2. The screen can be reused by erasing the stored images with white light.

Phosphor screen resolution is determined by the size of the phosphor crystals, the thickness of the coating, and the concentration (packing density) of the crystals. Phosphor crystal size and layer thickness are both inversely related to resolution, whilst a greater concentration of crystals will increase resolution.

Phosphor screen crystals are substantially larger than the silver halide crystals in film autoradiography. As a result, phosphor screens display superior sensitivity and hence exposure times are reduced.¹⁹ This is very convenient for radionuclides emitting low energy gamma rays such as ¹²⁵I.

For phosphorimaging and autoradiography, dynamic range is the intensity range over which signals can be quantified. This is equal to the net signal from the highest activity that can be measured (at the level of saturation) divided by the lowest activity level that can be detected. This lowest activity level is governed by the noise level that can be measured. Another advantage of phosphor screens is the increased linear dynamic range of five orders of magnitude compared to films.²⁰ This makes it less likely that screens will be saturated (and thus the user has a greater latitude for the exposure time), and a larger range of intensities can be quantified in a single image.

One of the drawbacks of autoradiography and phosphorimaging is that the tissue of interest must be physically removed from the subject. For this reason, these techniques are exclusively used for research, in particular to validate the binding properties of novel tracers and to quantify the expression of biomolecules such as receptors within tissues of interest. Moreover, *in vivo* imaging with PET and SPECT provides the opportunity to perform longitudinal dynamic studies. Conversely, in *ex vivo* studies such as autoradiography and phosphorimaging, only a single time point per animal can be sampled during an investigation.

1.2 Radiotracers

1.2.1 Radionuclides

Radiotracers have two essential components: a radionuclide that emits ionising radiation as it decays, and a ligand specific for a biological target. A radionuclide is an atom with an unstable combination of protons and neutrons in the nucleus and thus has excess energy available, which can be imparted to a newly created radiation particle (alpha or beta particles), or gamma rays. The choice of radionuclide is governed by several factors²¹:

- Physical half-life (the time where the radioactivity decays by one-half of its initial value)
- The nature of the radiation emitted (gamma rays which require lead shielding, alpha or beta particles that can be shielded with paper and aluminium respectively)
- Ease of production and availability
- Suitability for labelling the ligand

With the exception of radio metals such as ^{68}Ga and ^{82}Rb which are obtained from a generator, radionuclides used for PET imaging are produced in cyclotrons. Nearly all positron emitters have to be produced on site due to their rapid decay. In contrast, SPECT radionuclides have longer half-lives (Table 1), thus can be produced at a distant commercial centre and delivered to the site of radiotracer synthesis. This can be more cost effective as cyclotrons are expensive (\$1 - \$2 million) and require highly skilled staff for operation and maintenance.

1.2.2 Isotopes and Radioisotopes of Iodine

Radionuclides can also be referred to as radioisotopes of an element. Isotopes of an element are atoms that have the same atomic number (identical number of protons) but different atomic masses (different number of neutrons). The nuclear imaging studies outlined herein feature radio-iodinated tracers. Iodine has numerous radioisotopes and the naturally occurring isotope, iodine-127, can be used for modelling radiolabelling reactions. With its short half-life (13 hours) and medium energy gamma emission (159 KeV), iodine-123 is the preferred choice for SPECT scintigraphy. With a convenient half-life of 4.2 days, iodine-124 labelled radiopharmaceuticals are increasingly becoming useful tools for PET imaging.²² In other instances, iodine-131 is routinely used for SPECT radiotherapy studies, in particular treatment of hyperthyroidism, due to its emission of short-range beta radiation.²³

Iodine-125, the choice of radionuclide in this thesis, has low energy gamma emission and long half-life (35 KeV and 60 days respectively). These properties make iodine-125 extremely useful for radioimmunoassays²⁴ and brachytherapy, which involves

the use of small radioactive pellets or seeds.²⁵ Furthermore, iodine-125 is extensively used in pre-clinical studies, especially for preliminary evaluations of lead tracer candidates.

	Isotope	Half-life	Maximum Positron Energy	Photon Energy
	¹²⁵ I	60 days	-	27 keV
	¹²³ I	13 hours	-	159 keV
SPECT	^{99m} Tc	6 hours	-	140 keV
	¹¹¹ In	2.8 days	-	23 keV
	¹³³ Xe	5.3 days	-	80 keV
	¹⁸ F	110 min	0.64 MeV	511 keV
PET	¹¹ C	20 min	0.96 MeV	511 keV
	¹³ N	10 min	1.19 MeV	511 keV
	¹⁵ O	2 min	1.72 MeV	511 keV

Table 1. The properties of common SPECT and PET radioisotopes.

1.2.3 Pharmacokinetics

Radiotracers must display favourable pharmacokinetics, which can be defined as the interaction between the drug and body, encompassing the processes of absorption, distribution, biotransformation (metabolism) and excretion over time.²⁶ The pharmacokinetics of a radiotracer is predominantly dependant on its chemical structure.

The ligand carrying the reporter radionuclide must possess a number of vital properties which include:

- Accessible sites for efficient and rapid radiolabelling
- High structural stability to withstand the radiolabelling conditions

- High metabolic stability after administration into the living organism

After intravenous injection of a radiotracer, it is distributed throughout the body via the systemic circulation. During transit, the radiotracer can undergo metabolism and be excreted from the circulation. This process is known as clearance and can be defined as the notional volume of blood from which a substance is completely removed per unit time²⁷:

$$\text{Clearance} = \frac{\text{Dose}}{\text{AUC}} \quad \text{Equation 2}$$

The area under curve (AUC) is the total area beneath a plot of plasma concentration against time after administration of the radiotracer. Radio – High Performance Liquid Chromatography (Radio-HPLC) can identify and measure the concentration of radiotracers in the plasma whilst a gamma counter can determine the tissue distribution over time, revealing the total amount of radioactivity in the tissues of interest. This provides important information about how rapidly radiotracers are distributed, metabolised or excreted. Further information about these two techniques is provided in chapter 2.

Biodistribution studies can quantify the amount of radioactivity in different organs of the body over time. The results provide an insight as to which tissues have the highest uptake of the radiotracer and how this distribution varies over time between healthy and diseased states. The stability of the parent radiotracer can also be evaluated from biodistribution experiments. For example, de-fluorination will give $^{18}\text{F}^-$ which accumulates in bone tissue, and specifically within hydroxyapatite: a naturally occurring mineral with the formula $\text{Ca}_{10}(\text{PO}_4)_6(\text{OH})_2$.²⁸ The OH^- ion can be replaced by fluoride to produce fluoroapatite. Therefore, high uptake of radioactivity in bone tissue following administration of an ^{18}F -labelled tracer is strongly indicative of de-fluorination *in vivo*. Similarly, high uptake of radioactivity in the thyroid is suggestive of de-iodination. This is because the sodium iodide symporter (NIS) mediates uptake of iodide into follicular cells of the thyroid gland, which is the first step in the synthesis of thyroid hormones. These hormones (thyroxine and triiodothyronine) play an important role in the development and functional

maintenance of the CNS. Apart from thyroid cells, NIS can also be found, although less expressed, in the salivary glands, kidneys and the gastric mucosa. Therefore, high levels of radioactivity in these tissues following administration of radioiodinated tracers imply that de-iodination is a major metabolic route.

Metabolic processes alter the core scaffold of radiotracers by transforming lipophilic substances into hydrophilic products that can be excreted. Metabolites of radiotracers *in vivo* can cause unwanted distribution of radioactivity and this reduces image quality. Although imaging modalities such as PET and SPECT reveal the distribution of radioactivity and changes in their concentration over time, they provide no information about the chemical composition of the radiotracer. Therefore, it is important to determine the stability of a radiotracer as it gives a measure of the proportion of radioactivity that corresponds to the parent tracer.

Ideally, radiotracers should give high target-to-background ratios: a high uptake of the radiotracer in the tissue of interest compared to its (non-specific) localisation elsewhere throughout the body. The ability of small molecule radiotracers to reach their target is dictated by physicochemical properties (for example molecular weight and lipophilicity) which for those targeting the brain should in most cases adhere to the rules established by Lipinski.²⁹

Small molecules or peptides are cleared from the circulation and localise to the target tissue more rapidly compared to large molecules such as proteins and antibodies.³⁰ This is because, although the structure of the vascular endothelial cell monolayer varies throughout the body, the effective pore size in normal intact endothelium is less than 5 nM, enabling small molecules to achieve rapid equilibrium with the extravascular extracellular space. Furthermore, renal clearance of larger molecules is impeded by the small pores (4.5 – 5 nM in diameter) of the glomerular capillary wall.

Lipophilicity is a measure of the polarity of a compound. The traditional measure of lipophilicity is Log *P*: the partition coefficient of a molecule between an aqueous and lipophilic phase, usually water and octanol.³¹

$$\text{Log } P = \text{Log} \frac{[\text{Organic Phase}]}{[\text{Aqueous Phase}]}$$

Equation 3

Therefore, lipophilic substances are non-polar and have a low solubility for water and thus can also be referred to as hydrophobic. Many compounds however contain ionisable groups and are likely to be charged at physiological pH. Log *P* only describes the coefficient of neutral (uncharged) molecules. Log *D* is the distribution coefficient of a compound in a mixture of two immiscible phases at equilibrium and can be determined in a similar manner to Log *P*, however, instead of using water, the aqueous phase is adjusted to a specific pH using a buffer.³²

Polar compounds are highly soluble in water and tend to be cleared rapidly via the kidneys whereas lipophilic compounds are commonly excreted via the liver. However, the elimination of lipophilic compounds can be slow due to reabsorption across the kidney tubules back into the bloodstream.²⁶ Lipophilic compounds can also bind to a higher degree to plasma proteins such as serum albumin and, as a result, are unavailable to bind to the intended target.^{33, 34} Essentially, this can influence the distribution of the compound and compromise its ability to cross biological membranes (Figure 6). In addition, changes in plasma protein concentrations, which occur in certain disease states and under various pathophysiological conditions such as age, can change the unbound concentrations of lipophilic compounds.

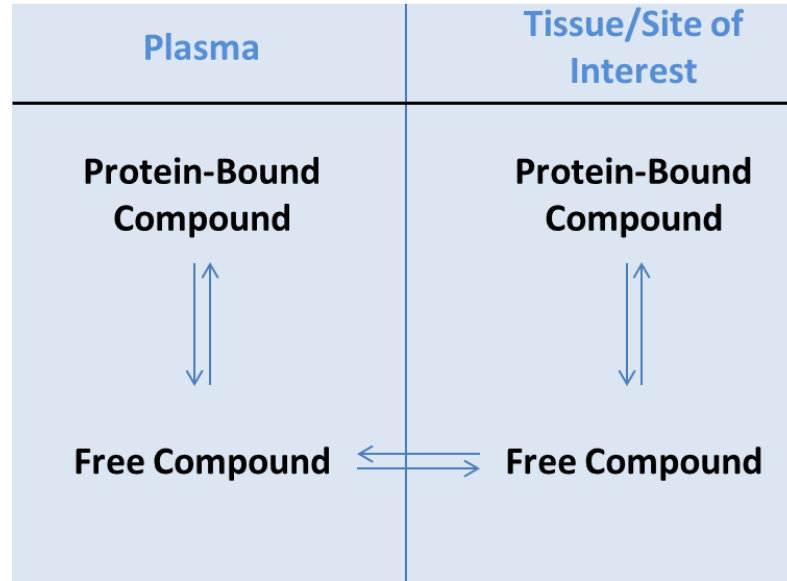


Figure 6. A two compartment model representing the influence of plasma protein binding on drug distribution.

The distribution of radiotracers should reflect the presence of the biological target in a concentration dependent manner, giving a high target-to-background ratio. For imaging of a receptor, the interaction of a radiotracer with its target depends on binding affinity. The binding of a particular drug (D) or radiotracer to the biological target or receptor (R) can be described by the following expression³⁵:



k_1 = rate constant for association between the drug and receptor

k_{-1} = rate constant for DR complex dissociation

Affinity describes the strength with which a ligand binds to a receptor and is equal to the k_1/k_{-1} ratio. A high affinity ligand has a greater tendency to bind to the receptor (a large k_1 value) relative to its dissociation from the receptor (a small k_{-1} value). K_d is the equilibrium dissociation constant and is the reciprocal of the affinity (k_{-1}/k_1). This value is widely used to describe the binding of drugs to a receptor. The K_d value

relates to the amount of ligand needed for a particular experiment and so the lower the value of K_d , the higher the affinity.

Radioligand binding assays reveal the affinity and specificity of a radiotracer to the receptor of interest. In saturation experiments, tissue sections, cultured cells or homogenates are incubated with an increasing concentration of a radiolabelled ligand or drug (Figure 7).³⁶ Analysis using curve fitting programmes measure the affinity of the labelled compound for a receptor (K_d and receptor density (B_{max})).

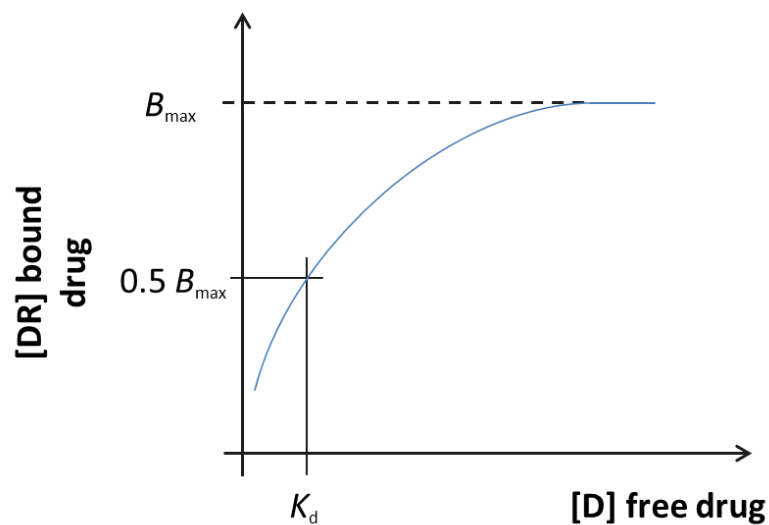


Figure 7. Graph of bound versus free drug showing relationship between K_d and B_{max} .

The graph represented in Figure 7 has the following equation:

$$Y = \frac{B_{max} \times [D]}{K_d + [D]} \quad \text{Equation 5}$$

When $[D]$ (drug or radiotracer concentration) is equal to K_d , the term $[D] / (K_d + [D])$ will equal 0.5 and therefore the Y value will be half the of B_{max} . Binding potential, (BP), is defined as:

$$BP = \frac{B_{max}}{K_d} \quad \text{Equation 6}$$

and is proportional to the total number of receptors in the region of interest.

However, there will be some degree of non-specific binding. The degree of non-specific binding can be determined using a saturating concentration of an unlabelled compound which competes for the target receptor binding site against a fixed concentration of the labelled compound. Under such conditions, virtually all the target receptors are occupied by the unlabelled compound and any radioactivity detected corresponds to radiotracer binding that cannot be displaced. The choice of compound is usually one that has a known affinity for the target of interest or the non-radiolabelled version of the radiotracer investigated. Specific binding can then be determined from total binding and non-specific binding by the relationship:

$$\text{Total Binding} = \text{Specific Binding} + \text{Non-Specific Binding} \quad \text{Equation 7}$$

For a competitive interaction, the concentration of a compound which inhibits the specific binding by 50% at equilibrium is known as the half maximal inhibitory concentration (IC_{50}). Similarly, the concentration or dose of a drug that gives half maximal response is known as the half maximal effective concentration (EC_{50}). The IC_{50} value can be converted to K_i using the Cheng-Prusoff equation³⁷:

$$K_i = \frac{IC_{50}}{1 + \left(\frac{[L]}{K_d}\right)} \quad \text{Equation 8}$$

[L] = the concentration of the free radioligand used in the assay

K_i : the concentration of competing ligand that would occupy 50% of the receptors if no radioligand was present. Whereas the IC_{50} value for a compound may vary between experiments depending on radioligand concentration, the K_i is an absolute value dependant only on the target and inhibitor concentrations. The K_i value for an

unlabelled drug should be the same as the K_d for the same drug in its radiolabelled form.

1.3 Radiotracer Development

For nuclear imaging to remain at the forefront of diagnostic imaging, new radiotracers need to be established. Nevertheless, the small number of novel radiotracers emerging in the clinic reflects the lengthy and costly process underpinning their development. For example, Schering and Amersham invested roughly \$150 million dollars during 1999 – 2004 for new imaging agents, but were not successful in delivering a product until mid-2007.³⁸ This high rate of failure is a cause of concern when attempting to develop new radiotracers in industry or academia.³⁹

The process for radiotracer development is summarised in Figure 8. The first phase identifies potential targets, (e.g. ion channels, receptors) that play a vital role in the generation or exacerbation of disease. At this stage, the clinical questions that need to be addressed are formed: what is the mechanistic role of this target in the pathophysiology of the disease, how can the actions of this target be suppressed, which chemical moieties will have the best fit at the target binding sites? Once these have been tackled and the aims are set, a library of compounds is assembled, or an existing library of compounds is used to test for target affinity. From this a lead molecule to be radiolabelled is identified and its molecular properties as well its specificity and selectivity for the target of interest are investigated through binding assays (section 1.2.3).

After *in vitro* evaluations, *in vivo* animal (pre-clinical) research is performed to ascertain the pharmacokinetics (section 1.2.2) of the radiotracer candidate: it is this stage of radiotracer development that forms the core research of this thesis. Multiple factors need to be reviewed for *in vivo* imaging of animals, and hence ensure reliable results are obtained. For example, gender, species and strain can have significant effects on the pharmacokinetics and metabolism of a radiotracer, as well as on the physiological parameters. This in part can be due to the varying levels of hormones, glucose and hepatic enzymes. Equally, fasting and dietary patterns may influence the

distribution and metabolism of the radiotracer. The injection volume and the physiological effects of the radiotracer itself also need to be considered when performing sequential imaging in the same animal. The general recommendation for the maximum volume on an intravenous injection is around 4% to 5% of the animal's blood volume. Accordingly, the volume injected into a mouse should be no more than 200 μL and 1000 μL for a rat.⁴⁰ Anaesthesia affects respiration and cardiac function, thus affecting radiotracer distribution and kinetics. Rigorous control of anaesthesia is therefore imperative in *in vivo* imaging experiments to ensure the results are not confounded and to obtain highly reproducible data.^{40, 41}

Clinical trials are conducted to determine how faithfully the pre-clinical findings translate into humans. To reach this stage, the pre-clinical data must prove the radiotracer is efficacious with a high benefit-to-risk ratio. Many clinical trials however have a high failure rate, particularly at the early stages (Phase 1). This is attributed to species variation between humans and rodents, in particular metabolism, radiotracer affinity to efflux pumps, the density and distribution of the target, and ability for the radiotracer to cross the blood-brain-barrier (BBB). Consequently, radiotracers that exhibit ideal properties in rodents may fail in humans. This is proven by epibatidine derivatives, developed as radiotracers for imaging of the nicotinic cholinergic receptors.⁴²



Figure 8. The process of radiotracer development.

In addition, evaluating the actions of potential drug candidates both at the pre-clinical and clinical stages can be a lengthy process. Molecular imaging with PET and SPECT can facilitate faster and more cost-effective decision-making to eliminate failures early in the drug evaluation process, whilst advancing promising candidates sooner.⁴³

1.4 Radiotracers for Neuroimaging

At each stage of the long and complex pipeline for radiotracer development, processes are finely tuned depending on the imaging target. In this section, the desirable characteristics that have been proposed for small molecule radiotracers to target the brain are discussed. In general, the criterion is fairly demanding, and therefore successful brain radiotracers have been rather sporadic.

Radiotracers can enter the brain by passive diffusion across the Blood Brain Barrier (BBB), which is a highly selective permeability barrier, maintaining the necessary environment for brain function.⁴⁴ The BBB is well equipped with efflux pumps such as P-glycoprotein (P-gp) and multi-drug resistant-associated proteins that function to repel many unwanted xenobiotic compounds. The properties that small molecule radiotracers must therefore exhibit to cross the BBB include:⁴⁵

- A molecular weight lower than 500 g/mol
- A polar surface area below 60-90 Å²
- The number of hydrogen bond donors lower than five or the sum of nitrogen and oxygen atoms less than 10
- A Log *P* between 1 and 3.5. (Exceptionally, some useful radiotracers with lower or higher lipophilicity readily enter the brain, shown by [¹¹C]MePPEP (cLog *P*: 5.7): a radiotracer for brain cannabinoid subtype 1 (CB₁) receptors.⁴⁶)
- Minimal affinity for efflux pumps and enzymes at the BBB

Ideally, metabolism for brain radiotracers should dominate outside of the brain yielding less lipophilic radio-metabolites with poor brain entry and no interaction with the target. Radio-metabolites that are formed in the brain can be problematic as they can give a false impression of the parent radiotracer distribution. This is because SPECT and PET have no means to discriminate between the chemical identities of detected radioactivity.

Additional parameters that will suit radiotracers for neuroimaging include:

- The absence of functional groups that will strongly ionise at physiological pH

- A high brain uptake of the desired radiotracer in rodent and non-human primate
- Disassociation or inhibition constants for the target in the nanomolar range

A convenient measure for radiotracer concentration in the brain is the standardised uptake value (SUV) which normalises radioactive concentration (e.g. Bq/mL) to injected radioactive dose and subject body weight (%ID/g).

When developing radiotracers for the brain, it is also important to ascertain differences in target density and structure between species. Having this determined at an early stage would assist in interpreting results and potentially reduce problems when translating the radiotracers to human studies. Furthermore, in order to maximise the image-ability of the radiotracer, the target should be highly localised and abundant in the organ of interest. This could explain why [¹¹C]MePPEP works well as a brain radiotracer despite its high lipophilicity: CB₁ receptors are one of the most abundant G-protein-coupled receptors in the brain, so give a high receptor-specific to non-specific signal.

1.5 Summary

The fundamental principles of nuclear imaging and radiotracers have been introduced. It has also been shown that radiotracer development is an intricately long process and that successful tracers for neuroimaging must conform to specific properties.

Chapter 2 Experimental Methods for Radiolabelling and Quantitative Analysis

The radiotracers used for SPECT and PET imaging should be synthesised with a high yield, purity and specific activity (SA). How this can be achieved and determined is discussed in the first part of this chapter. In addition, attention is given to the methods employed to incorporate radio-iodide onto chemical moieties.

Nuclear imaging only requires small quantities of the radiotracer (picomolar) for detection and thus offers exceptional sensitivity. To maximise this utility and extract accurate information from the data, the quantitative accuracy of the imaging modality needs to be determined. How best to attain this is detailed in the second part of this chapter.

2.1 Radiolabelling with Iodine

As part of the research outlined in this thesis, SPECT radiotracers have been developed and the principal radionuclide used is iodine-125 (^{125}I). Aliphatic carbon-iodine bonds are weak (222 kJ/mol) and so are prone to breaking, especially *in vivo* due to a plethora of enzymatic systems. As a result, when radioiodine is used to radiolabel a chemical construct, it is preferentially targeted to an sp^2 carbon atom in a vinylic or aromatic system since the resulting carbon-iodine bond is stronger (268 and 297 kJ/mol respectively).

Several strategies have been developed to radiolabel compounds with radioisotopes of iodine ($^*\text{I}$). The ideal method for any given radiochemical reaction is dependent on a variety of factors and is individually optimised to suit particular needs. Oxidative electrophilic radioiodination techniques are routinely used for labelling proteins and small organic molecules.

In electrophilic substitution reactions, a moiety with high electron density such as an aromatic ring, will attack electrophiles (atoms, molecules or ions which have an affinity for negative charge and will accept electrons). As a result, a new bond is formed accompanied by bond cleavage and loss of a positively charged group.

Electrophilic radioiodination reactions require an oxidising agent to generate the electrophilic species (HO^+I , $\text{H}_2\text{O}^+\text{I}$, ICl). Oxidising agents accept electrons and in turn become reduced whilst the reactant is oxidised. The most frequently used oxidising agents are peracetic acid and the *N*-chloro compounds such as chloramine-T, Iodogen and succinimides. *N*-chloro compounds are the most popular oxidants used⁴⁷, however their relatively strong oxidising properties can induce unwanted by-products. To minimise this, chloramine-T can be immobilised on spherical polystyrene particles while a thin layer of Iodogen can be applied to the walls of reaction vessels.

Of the *N*-chloro compounds, radioiodination using Iodogen (1,3,4,6-tetrachloro-3 α ,6 α -diphenylglycoluril, Figure 9) occurs in milder conditions than those required for the chloramine-T reaction.⁴⁸ This results in less oxidative damage, although in some cases, at the expense of reduced yields.

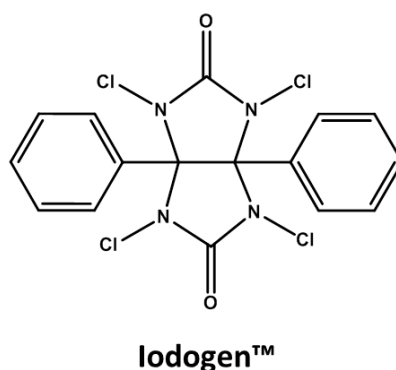


Figure 9. The chemical structure of Iodogen™.

Overall, radioiodination with Iodogen is extremely simple and reliable.⁴⁸ In brief, a solution of iodogen in an organic solvent such as dichloromethane is used to coat the inside of reaction vessels. Following evaporation of the solvent, the protein, peptide or compound to be labelled is added in a suitable buffer (e.g. PBS, pH 7.4) to the reaction vessel. The reaction commences following addition of [$^*\text{I}$]NaI and can be monitored by chromatographic techniques. Reactions are then stopped approximately 30 minutes later by simply removing the solution from the reaction

vessel (Figure 10). For practical ease, pre-coated iodogen tubes are commercially available.

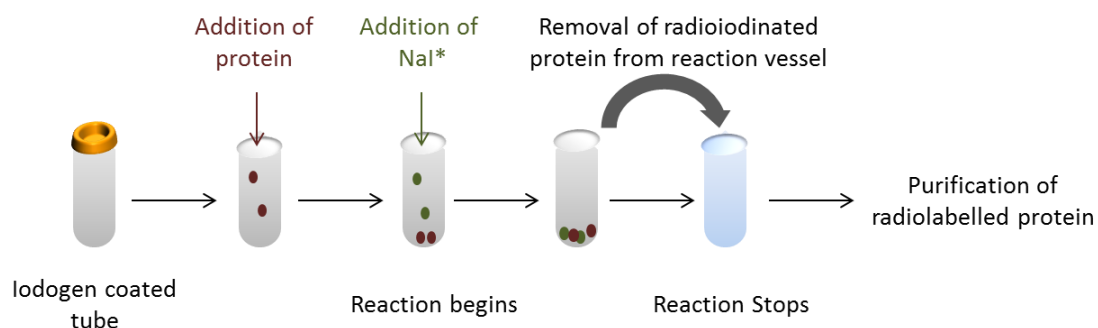
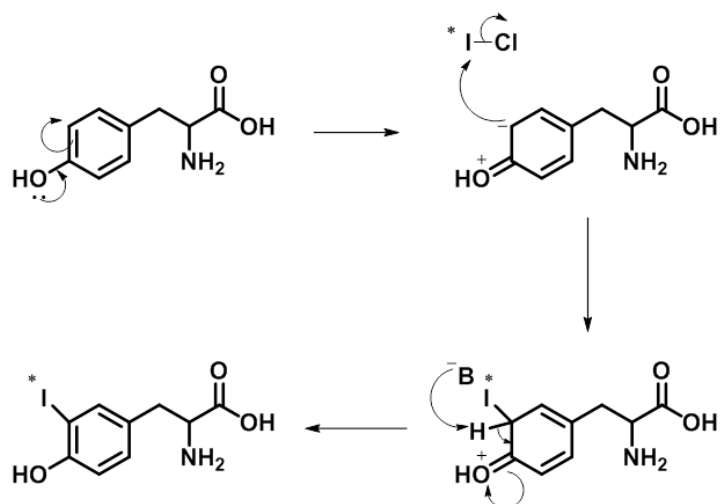


Figure 10. Radioiodination of proteins using pre-coated iodination tubes.

Proteins labelled with radioiodine using oxidative electrophilic radioiodination have long been used in nuclear medicine and biomedical research.⁴⁹ The reaction of Iodogen with iodide ion in solution (NaI) results in the oxidation of I^- to I^+ , ($I-Cl$) which then rapidly reacts with sites within the target molecules that can undergo electrophilic substitution reactions.

Aromatic rings within amino acids, principally tyrosine are the sites of iodination in many proteins.⁵⁰ The point of attachment is at the most electron-dense part of the ring. Therefore, with tyrosine, substitution of a hydrogen ion with the reactive iodonium ion occurs *ortho* to the phenolic hydroxyl group (Scheme 1). This is due to resonance stabilisation provided by the lone pair of electrons on the oxygen atom.



Scheme 1. (Radio)-iodination of tyrosine.

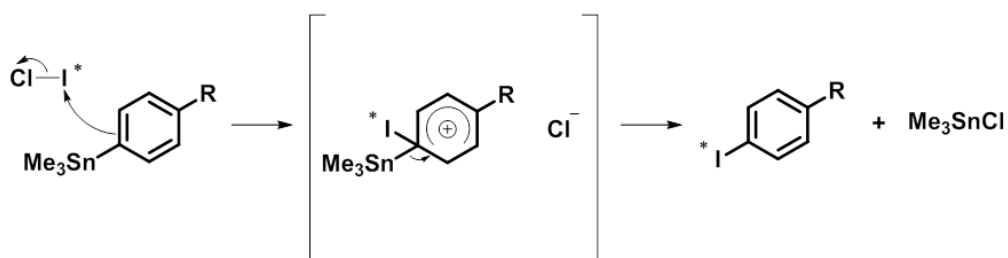
Essentially, the functional (-R) groups present on the aromatic ring that is to be radiolabelled is key in determining the radiolabelling methodology. Electron rich substituents will activate towards electrophilic substitution, which on the whole have shorter reaction times, require lower temperatures and entail more facile purification compared to nucleophilic substitution reactions.

2.1.1 Radioiodination of Small Organic Molecules

For the radioiodination of small organic molecules, the exchange reaction can either be isotopic (*I for I) or non-isotopic (*I for Br).⁵¹ In other cases, the exchange can be for a metal atom (M). One of the main advantages of this method is the opportunity to regioselectively radioiodinate activated and de-activated arenes under very mild conditions. This attractive method relies on the fact that the electropositive character of the metals used and the resulting polarisation of the C-M bond makes carbon-metal bonds much more activated for an electrophilic attack than carbon-hydrogen bonds. Therefore, substitution of M by *I is easier than substitution of H by *I.

The most commonly used exchange method for radioiodination involves organotin compounds, which readily affords site specific radioiodination, even at room temperature.⁵² Due to their inductive effects, alkyl groups attached to the tin increase electron density at the aromatic or vinylic carbon bound to the metal, thus facilitating attack of the '*I⁺' species (Scheme 2). Overall, there is a plethora of reactions

described in the literature where organotin precursors are used for radioiodination.⁵³⁻
⁵⁶ Also, the carbon-silicon bond shares similar properties to the carbon-tin bond thus organosilanes (e.g. trimethylsilane) can be used in exchange reactions to give iodinated compounds.



Scheme 2. Radioiodination of organotin compounds.

2.2 Radio - High Performance Liquid Chromatography

High Performance Liquid Chromatography (HPLC) is a powerful tool in analytical chemistry and is used to separate, identify and quantify chemical components in a mixture.⁵⁷ It is a highly improved version of column chromatography: instead of a solvent eluted through a column under gravity, it is forced through by high pressure and so experimental times are substantially reduced (Figure 11). Furthermore, the particles for loading the HPLC columns are considerably smaller in size, which provide a larger surface area to maximise interactions between the stationary and mobile phases. This facilitates the separation of chemical components which are structurally very similar.

Purification by means of HPLC is also robust as it provides automated radioactivity and UV detection of the chemical constituents. In most set ups, the UV and radioactive detectors are in tandem with each other, thus the data is collected a few seconds apart, with the time lag dependant on the flow rate of solvents eluting through the column and the volume of tubing between the two detectors. UV detection relies on the fact that organic compounds with chromophore groups absorb UV light set to a particular wavelength (usually 254 nm). A beam of UV light is directed at the stream of liquid eluting from the column and a UV detector is placed

at the opposite side to record how much of the light has been absorbed (Figure 11). The amount of light absorbed will depend on the concentration of a particular chemical moiety passing through the UV beam at a certain time. This relationship is described by the Lambert-Beer law where absorbance is directly proportional to the concentration of the absorbing compound if the path length of the measuring cell is held constant.

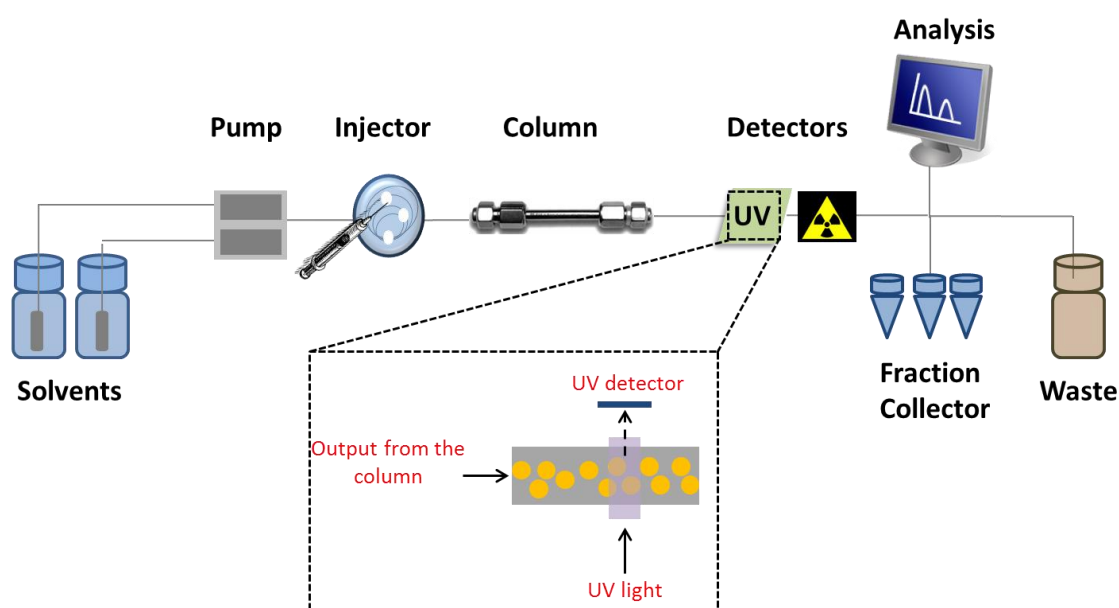


Figure 11. Schematic representation of HPLC.

There are two main types of HPLC:

- Normal HPLC: Essentially, the principles are the same as column chromatography and thin layer chromatography (TLC) where the column is packed with small silica particles. Therefore, polar compounds will adhere strongly to the polar silica compared to lipophilic compounds which will elute first.
- Reverse Phase HPLC: This is the more commonly used method where the stationary phase silica particles are modified with long hydrocarbon chains - typically between 8 to 18 carbons - rendering it non-polar. The analytes are separated according to their lipophilicity: the most lipophilic compounds have a stronger adsorption with the hydrophobic stationary phase and elute

relatively late, requiring a higher proportion of non-polar solvent (usually methanol or acetonitrile mixed with water) in the mobile phase. Modifiers such as organo-soluble salts and acids (e.g. tetrabutylammonium salts, trifluoroacetic acid) are often added to the mobile phase solvents in order to improve the chromatographic peak shape.⁵⁸

The time taken for a compound to elute through the column and reach the detector is known as the retention time which will depend on:

- The flow rate used (as this will affect the flow rate of the solvent)
- The nature of the stationary phase (including composition and particle size)
- The temperature of the column
- The physiochemical properties of the compound
- The composition of the eluent used

For radiotracer synthesis, it is paramount that the retention time of the pure, non-radiolabelled product is determined under the same HPLC conditions in order to elucidate the chemical identity and hence the desired fraction within the radiolabelled mixture.

HPLC results are presented in a chromatogram where the retention times are assigned on the x-axis and the intensity of UV or radioactivity detection is plotted on the y-axis. The area under a peak is proportional to the quantity of compounds which have passed the detectors at that time, and this is calculated automatically by a computer linked to the system. This makes it possible to calibrate the system to ascertain concentrations of the relevant compounds.

2.3 Specific Activity

Specific activity, defined as radioactivity per unit mass of the sample, can determine the chemical contamination of the sample with nonradioactive isotopes of the radionuclide. Therefore, low SA can result in unwanted pharmacological effects which can cause potential toxicity as well as affecting measurements.

To calculate SA of the radiolabelled product, the UV responses of the pure, non-radiolabelled (cold) product in a range of suitable concentrations are analysed by HPLC.⁵⁹ This concentration range is tailored around the analytical radiochemical yield obtained for that particular radiotracer. The resulting concentration-response curve is then applied to convert the UV response eluting with the radiolabelled product into moles. The amount of radioactivity corresponding to the product is determined by integration of the radio-detected peaks on the HPLC chromatogram and the injected activity, assuming there is no loss of radioactivity on the HPLC system. The specific activity can then be reported as the amount of radioactivity per mol (MBq/ μ mol).

2.4 Quantitative Accuracy for Imaging

In the studies performed as part of this PhD, radioactivity levels were measured using an ion chamber, SPECT/CT scanner, typhoon scanner and gamma counter, where results are presented in varying units (for example, Bq and CPM). Therefore, in the subsequent sections of this chapter, the methods employed to cross calibrate and acquire quantification factors for these equipment are outlined. This is particularly important for normalising the recorded counts in ROIs to the amount of radioactivity initially injected.

2.4.1 *In Vivo* SPECT

For nuclear imaging, PET allows more accurate quantification primarily due to its higher energy gamma emitters, coincident detection and superior correction for confounding factors such as attenuation. Nevertheless, developments in the hardware and reconstruction algorithms for SPECT systems over the years have increased its detection capability, thus making it an attractive option for *in vivo* imaging using longer-lived radionuclides.⁶⁰

However, several physical factors compromise the quantitative accuracy of SPECT and PET. These include:

- Attenuation: the loss of detected signals from the radionuclide because of their absorption in the body
- Spatial Resolution: the ability of the imaging system to discriminate between two adjacent objects. This can be expressed by the full width at half maximum (FWHM). FWHM is given by the difference between the two extreme values of the independent variable at which the dependant variable is equal to half its maximum value (Figure 12). If the points are separated by less than the FWHM distance of the system, then two separate points will be visualised as one
- Partial volume effects: the loss of apparent activity in small objects or regions due to the limited resolution of the imaging system
- Scatter: deviations from the expected trajectory (and hence part loss of energy) of a gamma ray upon interaction with matter

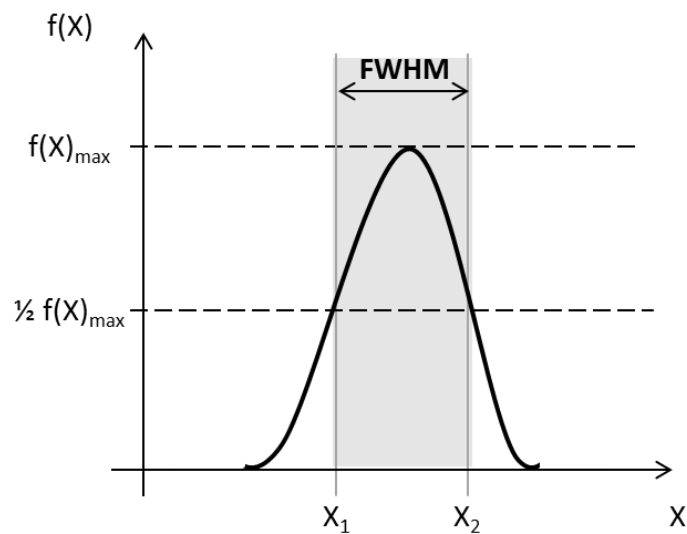


Figure 12. Graphical representation of the FWHM.

These effects can lead to a wrong interpretation of the results. For example, photons which deviate from the detectors may lead to a missed count. In other cases, the scattered photon could be detected in the wrong location, leading to an over- or underestimation of counts.⁶¹ It is therefore important to consider the magnitude of these effects when quantifying *in vivo* images. Also, since the uptake in organs of interest typically varies from <1% to 30%, there is a need to determine the validity

of measurements from SPECT imaging, especially when low radioactivity levels have been injected and there is minimal uptake in regions-of-interest (ROI). In the next section is discussed how the attenuation and calibration factors were attained.

In this body of work, SPECT/CT imaging was performed on a Nano-SPECT/CT small animal *in vivo* scanner. Calibrations on this system followed the protocols outlined in the manufacturers manual and have been conducted for each radionuclide-aperture combination used. The camera was calibrated for I-125 attenuation using a syringe filled with a known amount of radioactivity (measured in an ion chamber). To mimic the attenuation caused by the animal body, the syringe was placed inside a Plexiglas phantom filled with water (Figure 13). This water-filled phantom is likely to more closely resemble the attenuation caused by soft tissue rather than bones such as the skull. However it would be very difficult to find a phantom that suits both soft and hard tissues exactly. The phantom was subsequently scanned using the manufacturer's specifications.

The phantom images were reconstructed using InVivo Quant software, which converts dimensionless image count values to units of radioactivity in mega Becquerel (MBq) or kilo Becquerel (KBq). A calibration factor was obtained from the radioactivity levels measured in the ion chamber and the InVivo Quant software, which was stored and implemented in the reconstruction of subsequent images.



Figure 13. Quantification phantoms used for rat (a) and mouse apertures (b) on the SPECT/CT scanner.

2.4.2 Phosphorimaging

Phosphorimaging is a powerful tool for *ex vivo* analysis, to visualise the distribution of the radiotracer at higher resolutions, particularly on the sub-organ level, than that obtained *in vivo* with SPECT. For the studies outlined in this thesis, unmounted phosphor screens were used, which were scanned on a Typhoon 9410 Trio⁺ Phosphorimager.

Many precautions were undertaken so that the results would not be confounded by factors un-related to the study. For example, because phosphor screens are light sensitive and white light will erase them, the screens were stored at room temperature within a cassette which provided a dark and dry environment. It was also imperative that the screens had minimal exposure to white light when being transferred from the cassette to the scanner as direct exposure to bright light can erase up to 90% of the stored energy in less than 1 minute.

The screens were erased using a light box and cleaned with MIN-R Screen cleaner wipes before use. Also, to minimise the chances of blurred images, the screen was not adjusted once placed in contact with the radioactive samples.

To obtain sound quantitative data, the optimum exposure time was determined based on the radionuclide and the amount of radioactivity in the sample. Furthermore, the screens were scanned immediately after exposure as they lose intensity of the stored data with time (signal fading).²⁰

Phosphorimages have been quantified using radioactive standards comprising the radionuclide used in the study. These standards were co-exposed with the relevant brain sections to ensure they have the same exposure time and thus the same level of potential signal fading. The counts recorded from the standards were used to produce a calibration curve, correlating the amount of radioactivity measured in MBq by the ion chamber to the amount of counts recorded by the Typhoon scanner. This furnished the calibration factor for quantification and for normalising the results to the amount of radioactivity injected into the animals.

Radioactive standards for phosphorimaging quantification were prepared in buffer solutions (PBS). Depending on the levels of radiotracer uptake in the brain, the highest radioactivity concentration was measured in the ion chamber. Subsequent concentrations were obtained by serial dilutions (1:2). Aliquots of the standards were spotted onto quadrilateral filter paper mounted on microscope glass slides and allowed to dry. The volume spotted for each radioactive concentration was identical and the size of the quadrilaterals ensured uniform distribution of the radioactive solutions.

2.4.3 Biodistribution

Results for biodistribution studies are reported as % injected dose per gram of body weight (%ID/g). This was calculated by creating a calibration curve: appropriate concentrations of radioactivity in identical volumes were prepared by serial dilutions and measured in a Wizard² 2470 Automatic Gamma Counter, which was also used to measure radioactivity content in the tissues of interest. This calibration curve correlated the measured radioactivity in MBq from the ion chamber, (which was

used to determine the dose of radioactivity injected into animals), to that in counts per minute (CPM) recorded by the gamma counter and thus provided a conversion factor for quantification.

The Wizard² 2470 Gamma Counter consists of 10 detectors made of thallium activated, NaI crystals. For each new study, normalisation was conducted using solutions of the relevant radionuclide to correct for differences in efficiency between the detectors (Figure 14). Normalisation involves measuring the same radioactive solution in each of the wells and varies the amplification of the pulses from each detector, which then pass through a common energy window. This ensures that there is uniformity in the detection window across the gamma counter wells.

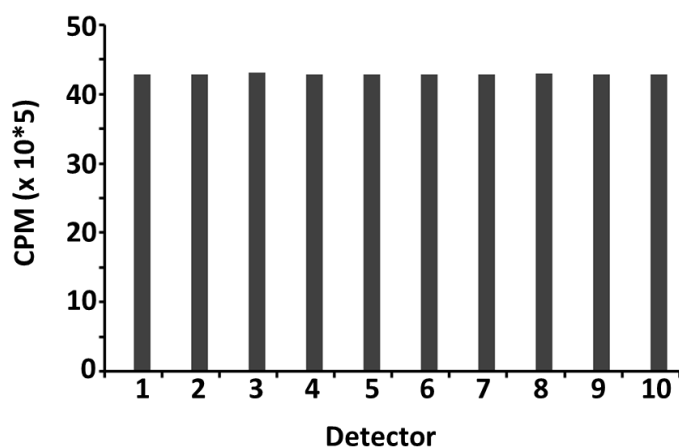


Figure 14. Results of the gamma counter after normalisation. Normalisation ensures there is a uniform detection window between the detectors.

2.5 Summary

In this chapter the basic concepts of radiolabelling and how to accurately quantify SPECT data have been introduced. The methods for calibrating and determining conversion factors between the equipment used have also been outlined.

Chapter 3 Evaluation of Voltage Gated Sodium Channel Blockers for Imaging with SPECT and PET

3.1 Aim and Hypothesis

In the studies outlined in this chapter, the core aim was to develop radiotracers and evaluate their potential to image the expression of Voltage Gated Sodium Channels (VGSCs). It was assumed that radioiodinated analogues of the BNZA and WIN17317-3 compound class would bind to neuronal VGSCs.

3.2 Sodium Channels

Abnormal expression and function of VGSCs has been identified in a number of neurological conditions including multiple sclerosis and epilepsy. Radiotracers for imaging VGSCs therefore hold significant potential as tools to study neuronal pathways as well as for diagnostic imaging and treatment monitoring. Despite this potential, the field of VGSC imaging remains largely unexplored.

3.2.1 Structure and Function

Sodium channels are integral membrane proteins, which conduct sodium ions (Na^+) through a cell's plasma membrane, either in response to binding of a ligand, (ligand gated sodium channels) or changes in the electrical membrane potential (voltage-gated sodium channels). This conduction triggers action potentials that propagate along neurons and to other electrically excitable cells.⁶² As a result, this allows communication and co-ordination of processes ranging from locomotion to cognition, particularly when speed is of the essence.⁶³

Pioneering studies have revealed three conformational states for VGSCs: at resting membrane potentials, sodium channels are closed and thus non-conductive.⁶⁴ Depolarisations open and activate the channels, permitting Na^+ ions to flow through. Following this, the channels enter the inactive state before returning to the non-conductive, resting state (Figure 15). During prolonged depolarisations, slow

inactivation occurs. This inactivation is about four times slower compared to fast inactivation, and involves rearrangements of the channel pore.⁶⁵ In some neurons, inactivation of the sodium current is incomplete, resulting in a slow inactivating current, often referred to as a slow, persistent Na⁺ current (I_{NaP}).

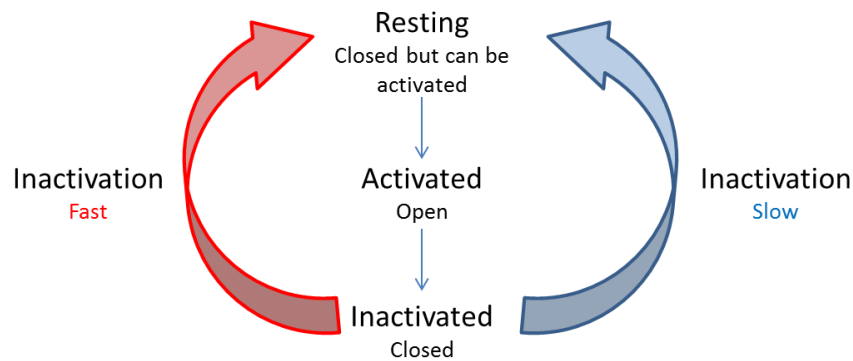


Figure 15. Conformational states of VGSCs.

VGSCs are composed of a principal α subunit, which can be associated with one or more auxiliary β subunits. Ten genes encoding the α subunit have been identified, nine of which have been characterised by their distinct pharmacological and electrophysiological properties.⁶² The remaining isoform seems to be gated by sodium concentration rather than voltage change. The nomenclature for VGSC isoforms uses a numerical system to define subfamilies and subtypes based on similarities between the amino acid sequences: Na refers to the chemical symbol of the principal permeating ion with the principal physiological regulator (voltage) indicated as a subscript (Na_v).⁶⁶ The number following indicates the gene subfamily (currently only Na_v1), which is succeeded by a number identifying the specific channel isoform (e.g., $\text{Na}_v1.1$). This last number has been assigned according to the approximate order in which each gene was identified.

The ion conducting pore of the channel is found within the α subunit, which folds into four domains, each containing six transmembrane helices (S1-S6, Figure 16). Extra- and intracellular loops connect these six helices, with the N and C terminals both located intracellularly.⁶⁷ The S4 helix has positively charged amino acid residues which serve as gating charges, moving across the membrane to initiate

channel opening in response to a depolarisation of the membrane. The pore module is formed by the S5 and S6 helices where the S6 helix contains binding sites for various-therapeutically important pore blocking drugs. The β subunits modulate the function of the α subunits and help their integration into the plasma membrane.⁶⁷

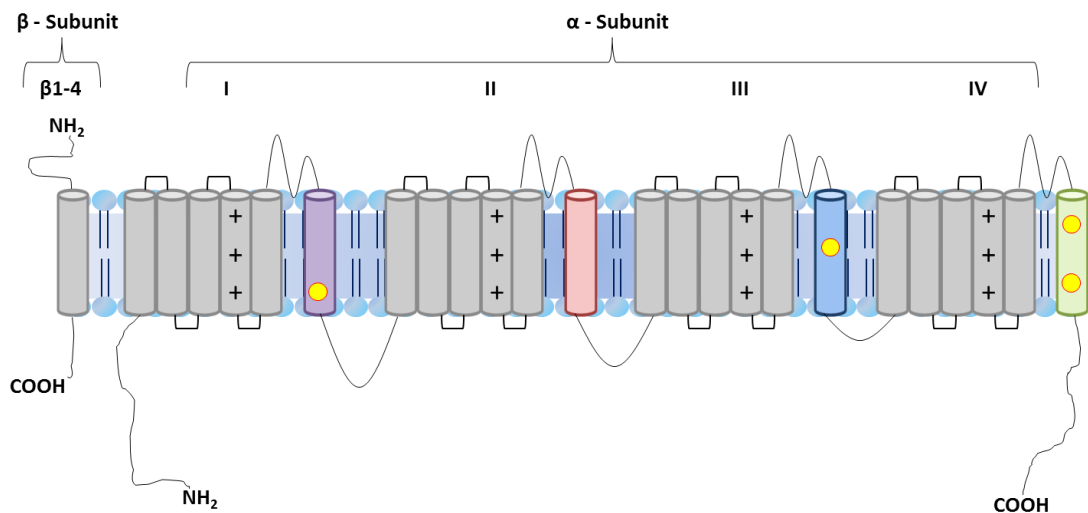


Figure 16. Structural representation of VGSCs. The pore forming α subunit comprises four domains (labelled I – IV), each with six transmembrane helices. The circles on helices I6, III6 and IV6 represent the binding sites for therapeutic blocking drugs.⁶³

Recently, studies elucidating the crystal structure of the *Arcobacter butzleri* VGSC Na_vAb have revealed the molecular basis of voltage sensing, ion conductance and voltage dependant gating.⁶⁸ Hydrophilic interactions between arginine charges within the voltage sensor (S4) appeared to catalyse gating charge movements during activation. Investigations have also indicated that the voltage sensor domains, along with the S4-S5 linkers, dilated the central pore by pivoting together around a hinge at the base of the pore module. Furthermore, the selectivity filter for the channels was found to be short, about 4.6 Å wide, and water filled with four acidic side chains surrounding the narrowest part of the ion conduction pathway.⁶⁸

The classification of VGSCs is based on their sensitivity to tetrodotoxin (TTX), which is a potent neurotoxin produced by marine organisms such as the tetraodon pufferfish.⁶⁹ Nanomolar concentrations of TTX blocked $Na_v1.1-1.4$, $Na_v1.6$ and $Na_v1.7$ whilst significantly higher (micro molar) concentrations were needed to block $Na_v1.5$, $Na_v1.8$ and $Na_v1.9$.⁶⁹ The isoforms in TTX-sensitive and TTX-

resistant groups are nevertheless closely related based on their amino acid sequences. The VGSC subtypes are differentially distributed throughout the body, as shown in Table 2.

Isoform	Location
Na _v 1.1, Na _v 1.2, Na _v 1.3, Na _v 1.6	Central Nervous System
Na _v 1.4, Na _v 1.5	Cardiac and Skeletal Muscles
Na _v 1.7, Na _v 1.8, Na _v 1.9	Peripheral Primary Sensory Afferents

Table 2. VGSC subtypes located throughout the body. Na_v1.2 appears to predominate in the immature brain, with Na_v1.6 becoming more prevalent during maturation.⁷⁰

The research outlined in this chapter focuses on neuronal VGSCs, in which their dysfunction or over expression along axons and neurons has been implicated in a number of neurological diseases, in particular multiple sclerosis and epilepsy. The next section of this chapter will present some of the evidence linking VGSCs to these brain disorders.

3.2.2 VGSCs in Disease

3.2.2.1 Multiple Sclerosis

Multiple Sclerosis (MS) is an inflammatory disease of the Central Nervous System (CNS) with a wide range of symptoms including problems with muscle control, vision and balance. There is currently no cure for MS and although a number of treatments are available, none can halt the progression of primary progressive MS.⁷¹ Therefore, more effective treatments are required and to achieve this, early biomarkers need to be established.

Two processes have been implicated in the pathogenesis of MS. The first is axonal damage, where the axon becomes severed or destroyed and so electrical impulses are impeded along the nerve or across the synapse.⁷² The second process is

demyelination, which describes the loss of the protective myelin sheath that insulates nerve fibres and allows the efficient transmission of impulses along them. These two processes affect the ability of neurones to communicate with each other, resulting in loss of neurological function and the debilitating effects observed in MS patients.

Numerous *ex-vivo* studies have identified changes in VGSC expression under MS conditions. Immunocytochemistry with subtype specific antibodies revealed a 52% reduction in Nav1.6 and a 63% increase in Nav1.2 expression along the optic nerve in animal models of MS compared to controls.⁷³ A similar pattern was observed in the retinal ganglion cells, suggesting that Nav1.2 can support conduction in demyelinated axons.⁷³

As mentioned, axonal degeneration is one of the pathological features of MS. A marker for axonal injury is β -amyloid precursor protein (β -APP). Using fluorescently labelled antibodies, it has been shown that $74 \pm 4\%$ of β -APP positive axons co-express Nav1.6 and the sodium calcium exchanger (NCX), compared to $4 \pm 1\%$ in β -APP negative axons.⁶⁵ The high expression of Nav1.6 is thought to produce a persistent sodium current, triggering a reversal of NCX. As a result, NCX imports Ca^{2+} whilst exporting Na^+ and the subsequent accumulation of intraaxonal calcium ions triggers injurious secondary cascades and axonal injury.⁶⁵

Interestingly, lamotrigine, a sodium channel blocking agent, was found to be effective in preventing axonal degeneration in an animal model of MS whilst various sodium channel blocking agents have ameliorated spinal cord inflammation.⁷⁴ These include TTX, lidocaine, phenytoin and carbamazepine which exhibit protective effects at concentrations that do not compromise the conduction of action potentials. The protective role of sodium channel blockers is based on the assumption that sodium channels contribute to activation of microglia and macrophages.⁷⁵

3.2.2.2 Epilepsy

Epilepsy is a neurological disorder characterised by recurrent seizures (further details about this disease are given in chapter 5). Alterations in the density and distribution of VGSCs have been observed in animal models of acute or chronic epilepsy.

Genetic studies on the E1 (epileptic) mouse strain found an over expression of $\text{Na}_v1.2$ mRNA levels (by 30 - 40% compared to controls), suggesting that altered VGSC expression may be one of the intimate processes underlying epileptogenesis.⁷⁶

The origin of epileptic seizures is thought to involve hyperexcitability caused by excessive depolarisations. This increase in depolarisations is thought to result from high frequency action potentials generated by VGSCs.^{77, 78} Blockade of VGSCs is the most common mechanism of action among currently available antiepileptic drugs (AEDs), including phenytoin, carbamazepine and lamotrinine.⁷⁹ As mentioned, VGSCs cycle through three states (resting to open, open to inactivated, inactivated to resting, Figure 15). During seizures, the aberrant firing of action potentials results in a high proportion of sodium channels in the inactivated states.⁸⁰ VGSCs are unable to respond to further depolarisations until they have returned from the inactivated to the resting state. AEDs bind preferentially to the inactivated state and thus slow the fast inactivation pathway of VGSCs. In doing so, these drugs can suppress the rapid and excessive firing of neurons that can start a seizure.

3.3 VGSC Blockers

Compounds can bind selectively to distinct conformational states of VGSCs. Drugs can impair the conduction of Na^+ either by binding to the extracellular pore opening (TTX, Saxitoxin) or by blocking the channels from the intracellular side (local anaesthetics, antiarrhythmic agents) triggering conformational changes.

Toxins have been useful for unravelling the structural and molecular determinants of VGSCs by modifying gating actions.⁸¹ At least six toxin-binding sites (sites 1-6) have been identified with site 1 toxins inhibiting and 2-6 site toxins enhancing sodium current.⁸² The usefulness of toxins as clinically relevant drugs is limited by their high molecular weights and lack of subtype specificity.⁸³ Furthermore toxins, which have affinity for resting state VGSCs, cannot be removed by changing the membrane voltage or the gating of the channel. However, promising success has been demonstrated with ProTx-II, a peptide derived from tarantula venom which is two orders of magnitude more selective for $\text{Na}_v1.7$ and inhibited action potential

propagation in nociceptors⁸⁴, whilst μ O-conotoxin has been shown to selectively block $\text{Na}_v1.8$ currents in chronic pain animal models.⁸⁵

Inhibition of VGSCs from the intracellular side requires binding at sites located at the surface of the S6 helices which will occlude the pore opening.⁸⁶ It has been hypothesised that these binding sites can be accessed by two distinct mechanisms: a hydrophilic pathway requiring binding of the drug from the intracellular side during channel opening and a hydrophobic pathway.⁸⁷ Indeed, the recent crystal structure of the *Arcobacter butzleri* VGSC NavAb confirmed the existence of hydrophobic fenestrations within the protein lipid interface.⁶⁸ This suggests a molecular mechanism featuring a closed state for VGSC inhibition. Hydrophilic compounds will be incompatible for the hydrophobic route, thus requiring channel opening. In this case, cumulative block of VGSCs occurs with high-frequency opening, with drug dissociation from the binding site slower than its association rate (i.e. $K_1 > 1$). In contrast, neutral or hydrophobic compounds can access the intracellular binding site through the hydrophobic pathway when VGSCs are in the closed state, as well as the hydrophilic pathway during channel opening.

Many neurological conditions involve neurons firing action potentials with high frequency and thus cells display a tonically depolarised membrane potential. Consequently, compounds exhibiting a frequency dependant inhibition of neuronal VGSCs are desirable as they will tend to only target VGSCs in the affected areas. Drugs which have a slow dissociation from VGSCs when the membrane potential is returned to the resting value upon repolarisation are most effective at affecting high frequency firing, as demonstrated by phenytoin and carbamazepine.⁸³

Although many VGSC blockers have been developed (Figure 17), there are currently still no established tracers for imaging of excitatory ion channels *in vivo*. Nevertheless, a number of tracers have been evaluated for imaging of *N*-methyl-*D*-aspartate receptors (NMDARs), which is explored in chapter 6. For VGSC tracers, it is likely that both ion channel expression and function can influence the binding pattern, at least for state dependant ligands. In addition, the subtype selectivity of a tracer will determine its potential applications. Therefore, in order to diagnose and/or treat CNS-related diseases, potential new drugs have to be significantly more active at neuronal VGSCs ($\text{Na}_v1.1$ - $\text{Na}_v1.3$) compared to those at other regions such as in

cardiovascular tissue ($\text{Nav}1.4$, $\text{Nav}1.5$), whilst demonstrating minimal effect on normal action potentials.⁸⁸ However, the high degree of homology between VGSC isoforms makes development of subtype selective ligands challenging. The similarity in the amino acid sequence between the brain sodium channel genes, *SCN1A*, *SCN2A*, and *SCN3A* is greater than 90% and these three genes closely resemble additional brain genes (*SCN8A*), as well as sodium channel genes in the peripheral tissue and sensory neurones.⁸⁸ The binding of VGSC tracers *in vivo* is therefore likely to reflect VGSC expression in the periphery as well as in the brain, with state dependant ligands showing increased uptake in tissues with high electrical activity.

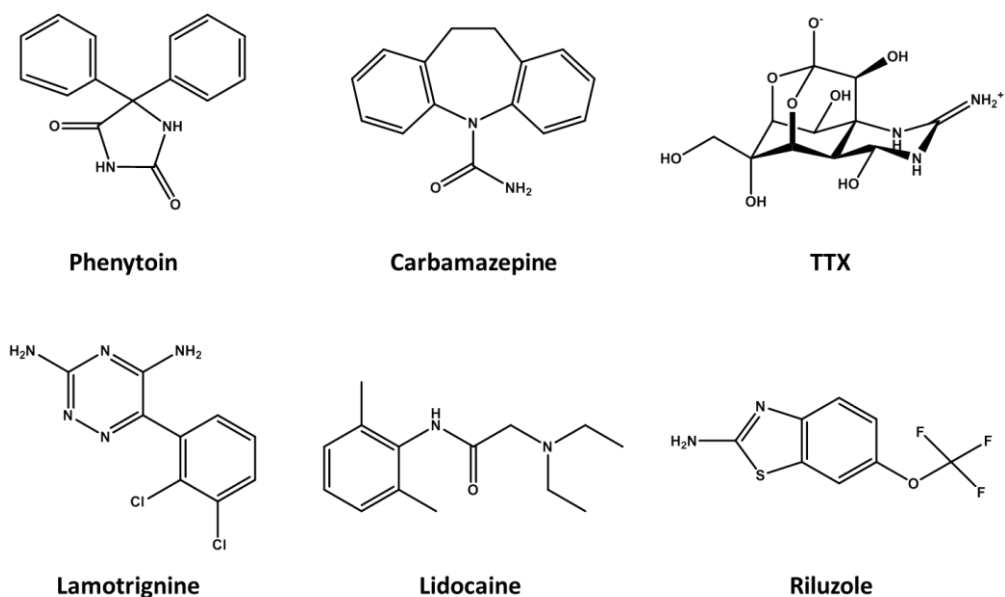


Figure 17. Structures of VGSC blockers.

As part of this research, two radiotracers have been developed and their ability to target neuronal VGSCs has been evaluated by biodistribution, metabolite analysis, and *in vivo* SPECT/CT imaging in healthy mice. In the subsequent section, the results from the two studies are reported, beginning in each case with a short introduction, reasoning why that particular compound class was selected for tracer development and evaluation. The experimental methods for the synthesis and evaluation of the two tracers are reported in chapter 8.

3.4 Benzazepinone Derived VGSC Blocker for SPECT Imaging

3.4.1 BNZA

It has been reported that the 1-benzazepin-2-one derivative [³H]BNZA (Figure 18, **1**) is a highly potent and state dependant VGSC blocker, displaying high affinity to rat brain synaptosomal membranes ($K_d = 1.53 \pm 0.46$ nM) as well as to transfected human hNav_v1.5 ($K_d = 0.97$ nM) and hNav_v1.7 ($K_d = 1.6$ nM) VGSC isoforms.⁸⁹ Furthermore, sodium channel modulators inhibited binding of [³H]BNZA to rat brain membranes in a concentration dependant manner and displayed K_i values (veratridine: $K_i = 6.8 \pm 2.4$ μM, phenytoin: $K_i = 8.0 \pm 1$ μM) similar to those found in competition experiments with other well characterised sodium channel ligands such as [³H]batrachotoxin ($K_i = 7.0$ μM).⁹⁰ Batrachotoxin (BTX) is an extremely toxic alkaloid that binds with high affinity to VGSCs in nerve and muscle membranes and due to its potency and specificity, is commonly used to study the function of sodium channels.^{91, 92}

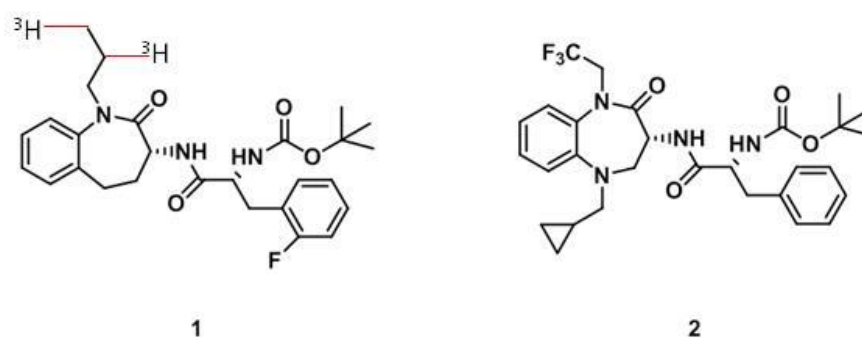


Figure 18. Structure of BNZA (**1**) and one of its analogues (**2**).

Analogues of BNZA have demonstrated good metabolic stability, and have been shown to be highly efficacious in the maximal electroshock (MES) model of epilepsy in mice.⁸⁰ When orally dosed at 3 mg/kg, analogue **2** (Figure 18) prevented shock induced tonic-clonic seizures in 90% of subjects (n = 10) at 30 min post dosing. These results are comparable to those obtained with clinical standards such as carbamazepine (MES ED₅₀ = 3.4 mg/kg) and lamotrigine (MES ED₅₀ = 2.2.

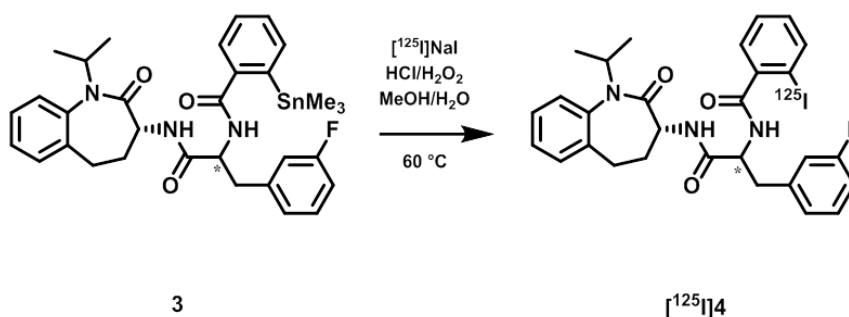
mg/kg), and imply that derivatives of this compound class can cross the blood-brain barrier (BBB).

Collectively, these data suggest that 1-benzazepin-2-ones meet many of the key criteria for developing neuronal radiotracers, and that suitably radiolabelled derivatives of BNZA have the potential for imaging of VGSCs.

3.4.2 Results

3.4.2.1 Radioiodinated BNZA Analogue

The precursor (**3**) for the radioiodinated BNZA analogue (**4**) was prepared by Dr C Perèz-Medina in an excellent overall yield (46%).⁹³ In one of the synthetic steps to obtain **3**, a racemic substrate (*N*-Boc-DL-3-fluorophenylalanine) was used, and therefore the precursor (**3**) and the radiolabelled product ($[^{125}\text{I}]\mathbf{4}$) were obtained as a mixture of diastereoisomers. Semi-preparative HPLC was used to separate the diastereoisomers of the radiolabelled product ($[^{125}\text{I}]\mathbf{4}$), whilst enriched fractions of the non-radiolabelled product (**4**) were obtained by column chromatography. The two diastereoisomers of **4** were termed *high-4* (*h-4*) and *low-4* (*l-4*) according to their relative affinities towards neuronal VGSCs. The absolute configuration around the α -carbon (denoted by *) was not determined for this study.



Scheme 3. Radiolabelling of the trimethyltin tin precursor to obtain a radioiodinated derivative of BNZA.

A mixture of the two diastereomers of [^{125}I]**4** was obtained with a radiochemical yield of $24 \pm 4\%$ ($n = 11$) and specific activity $37.0 \pm 10.4 \text{ GBq } \mu\text{mol}^{-1}$ ($n = 8$) upon treatment of the trimethyltin precursor (**3**) with [^{125}I]NaI in the presence of 0.1 M HCl and 1.4% H_2O_2 for 30 min at 60 °C. Retention times of [^{125}I]*h*-**4** and [^{125}I]*l*-**4** were 21 and 22 min respectively (Figure 19 a) with excellent radiochemical (>99 %) and diastereomeric (>99 %) purities (Figure 19 b-d). Using the traditional n-octanol shake flask method, The Log *D*_{7.4} of [^{125}I]*h*-**4** was measured to be 3.93 ± 0.01 ($n=4$) by Dr C Perèz-Medina.

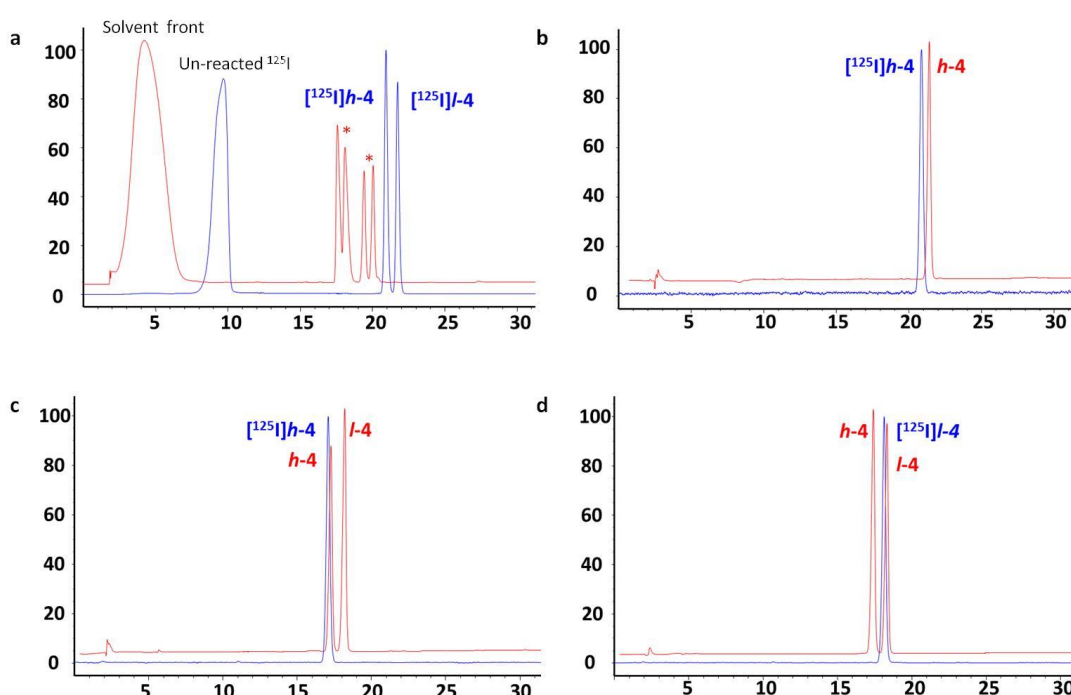


Figure 19. HPLC chromatograms for the synthesis of [^{125}I]**4**. The chromatograms show radioactivity (blue trace) and UV absorption at 254 nm (red trace). A = The crude reaction mixture from the radiolabelling of **3** (*unidentified impurities), b = co-injection of *h*-**4** with [^{125}I]*h*-**4**, c = co-injection of a mixture of *h*-**4** and *l*-**4** with [^{125}I]*h*-**4**, d = co-injection of a mixture of *h*-**4** and *l*-**4** with [^{125}I]*l*-**4**. For diagrammatic purposes, the radioactivity signal is offset from the UV-signal in b-d.

3.4.2.2 In Vitro Evaluation

A diastereomeric mixture of **4** was sent for evaluation against the cloned human $\text{Na}_v1.2$ (h $\text{Na}_v1.2$, *SCN2A* gene) and $\text{Na}_v1.7$ (h $\text{Na}_v1.7$, *SCN9A* gene) isoforms

expressed in Chinese Hamster Ovary Cells (CHO) by means of automated patch clamp (ChanTest Corp., U.S.A.).⁹⁴ The IC₅₀ values for compound **4** were 4.1 ± 1.5 μM and 0.25 ± 0.07 μM , for Na_v1.2 and Na_v1.7 respectively. While the amino acid sequence of mammalian VGSCs has been largely preserved across species, distinct pharmacological profiles have been reported for human and rodent isoforms.⁹⁵ Therefore, a receptor [³H]BTX binding assay (by Ricerca Taiwan Ltd, Taiwan) was carried out using rat brain homogenates.⁹⁰ Compound *h*-**4** displaced [³H]BTX with an IC₅₀ of 0.15 μM whereas *l*-**4** had three times lower affinity (IC₅₀ = 0.48 μM). From this result, the terms high (*h*) and low (*l*) were assigned to the relevant diastereoisomer.

3.4.2.3 Biodistribution

The distribution of radioactivity was measured *ex-vivo* 5, 15, 30 and 60 min after i.v. injection of [¹²⁵I]*h*-**4**, and in a separate set of animals, 5 and 30 min after i.v. injection of [¹²⁵I]*l*-**4** ($n \geq 3$, Table 3). Initially a high uptake in the liver ($36.0 \pm 2.10\%$ ID/g) and kidneys ($24.0 \pm 1.0\%$ ID/g) was observed for [¹²⁵I]*h*-**4** with later time points dominated by high uptake in the intestines. The brain uptake was moderate for [¹²⁵I]*h*-**4** (0.92% ID/g at 5 min post injection) and gradually decreased over time. Blood clearance was slow, with $7.0 \pm 1.10\%$ ID/g at 5 min post injection and $3.0 \pm 0.45\%$ ID/g at 60 min, resulting in poor brain-to-blood ratios at all time points.

The tissue distribution of [¹²⁵I]*l*-**4** was similar to that of [¹²⁵I]*h*-**4**, with high uptake in the liver and kidneys 5 min post injection, and high uptake in the intestines at 30 min. The brain uptake was lower than that of [¹²⁵I]*h*-**4** (0.68 vs. 0.92% ID/g at 5 min).

	$[^{125}\text{I}]h\text{-4}$				$[^{125}\text{I}]l\text{-4}$	
	5 min	15 min	30 min	60 min	5 min	30 min
Blood	7.17 ± 1.10	4.66 ± 0.23	5.60 ± 0.21	3.25 ± 0.45	6.89 ± 0.81	4.05 ± 0.55
Heart	7.84 ± 1.20	4.27 ± 0.70	6.01 ± 0.81	2.96 ± 0.38	8.78 ± 1.84	4.27 ± 0.70
Liver	36.10 ± 2.1	27.50 ± 2.8	43.40 ± 3.4	18.80 ± 1.3	40.60 ± 3.5	31.70 ± 3.9
Kidneys	24.40 ± 1.0	12.80 ± 0.9	17.80 ± 1.7	7.34 ± 0.77	32.70 ± 2.9	20.30 ± 3.2
Brain	0.92 ± 0.08	0.49 ± 0.11	0.59 ± 0.07	0.26 ± 0.03	0.68 ± 0.10	0.34 ± 0.05
Lungs	7.98 ± 0.85	6.89 ± 0.93	6.28 ± 0.46	4.51 ± 0.68	9.10 ± 1.52	4.86 ± 0.69
Muscle	3.47 ± 0.18	2.53 ± 0.58	4.30 ± 1.3	1.71 ± 0.26	4.05 ± 0.56	2.41 ± 0.36
Spleen	10.10 ± 1.7	5.78 ± 0.61	6.94 ± 0.58	2.71 ± 0.23	10.10 ± 1.7	6.33 ± 0.83
Bone	2.11 ± 0.56	1.27 ± 0.36	1.76 ± 0.81	1.97 ± 0.76	5.09 ± 3.48	3.41 ± 1.33
Small Int.	9.89 ± 1.03	10.60 ± 1.8	39.50 ± 2.5	25.60 ± 2.7	9.63 ± 1.02	33.80 ± 8.2
Stom. / L. Int.	4.42 ± 0.77	4.60 ± 1.0	10.20 ± 1.3	12.6 ± 2.4	6.39 ± 1.68	7.38 ± 1.7

Table 3. Biodistribution of $[^{125}\text{I}]h\text{-4}$ and $[^{125}\text{I}]l\text{-4}$. Values are expressed as %ID/g ± SD (n ≥ 3).

3.4.2.4 Metabolite Analysis

Radio-HPLC was used to analyse the composition of radioactive species in plasma and brain tissue over a period of one hour after injection of $[^{125}\text{I}]h\text{-4}$. In both plasma and brain, $[^{125}\text{I}]h\text{-4}$ was found to have excellent stability, and was the predominant radioactive species at all time points. The fraction of the intact tracer $[^{125}\text{I}]h\text{-4}$ was 93% at 5 min post-injection, 70% at 30 min, and 58% at 60 min (n = 2) in plasma. 15 min after tracer administration, three metabolites, all more polar than the parent compound, were identified. In the brain, the intact tracer $[^{125}\text{I}]h\text{-9}$ was the only radioactive species found at the earlier times points (5, 10 and 15 min), with some minor metabolites (20%, n = 2) occurring 60 min after administration.

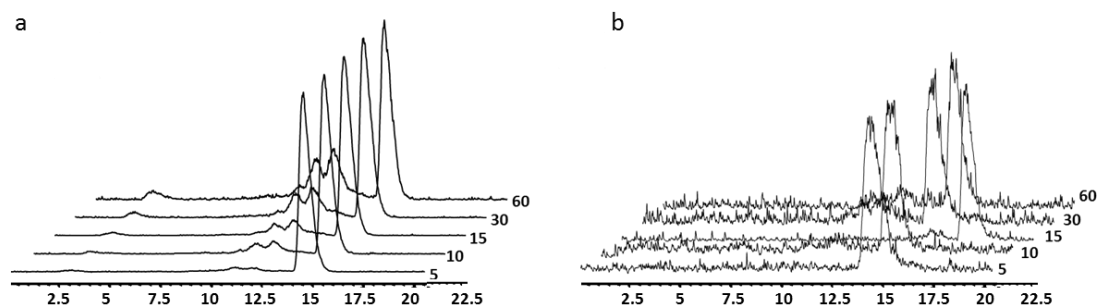


Figure 20. HPLC radioactivity profiles of plasma (a) and brain (b) samples after $[^{125}\text{I}]h\text{-4}$ injection. Plasma and brain samples were injected for HPLC analysis 5, 10, 15, 30 and 60 min post administration of $[^{125}\text{I}]h\text{-4}$. The chromatographic peaks have been offset from each other in order to distinguish the results at each time point.

3.4.2.5 SPECT/CT Imaging

Whole body SPECT/CT scans were recorded for both diastereoisomers of $[^{125}\text{I}]4$. Initially, a high uptake of radioactivity was observed in the liver (first scan, 15-25 min post-injection) and therefore, the SPECT images (Figure 21) were in overall good agreement with the biodistribution data. At the later time points (second scan, 35-55 min post-injection) the images were dominated by high levels of activity in the intestines. Interestingly, in three out of a total of seven mice imaged, a high uptake was observed in the interscapular region (Figure 21e). The uptake in this region appeared to be age related, as it was observed in adult mice (8-10 weeks old, $[^{125}\text{I}]h\text{-4}$ ($n = 2$) and $[^{125}\text{I}]l\text{-4}$ ($n = 1$)), but not in a group of younger animals (4-6 weeks, $[^{125}\text{I}]h\text{-4}$ ($n = 2$) and $[^{125}\text{I}]l\text{-4}$ ($n = 2$)). Unfortunately, the activity levels were too low in order for SPECT imaging to show the regional distribution of $[^{125}\text{I}]4$ in the brain.

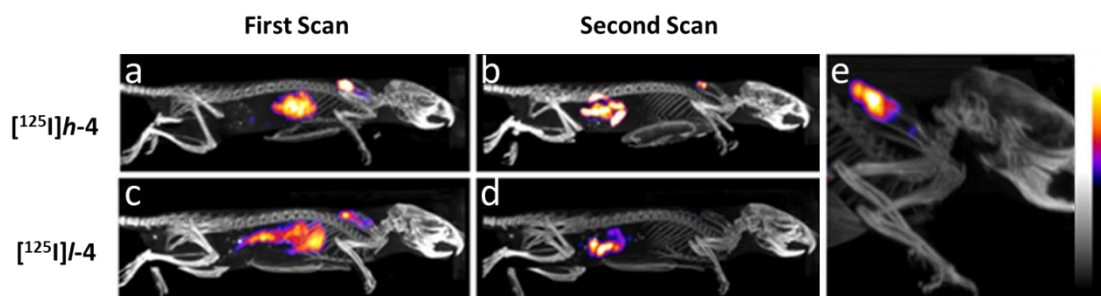


Figure 21. SPECT/CT images showing the distribution of [^{125}I]**4**. The images show the distribution of [^{125}I]*h*-**4** (a and b) and [^{125}I]*l*-**4** (c and d) at an early time point (5-25 min post tracer administration, a and c) and at a late time point (35-55 min post tracer administration, b and d). e = SPECT/CT image showing the uptake of [^{125}I]*h*-**4** in the interscapular region, 55-65 min post injection.

3.4.3 Discussion

In this collaborative study, the novel radioiodinated 1-benzazepin-2-one [^{125}I]**4** has been synthesised and evaluated to assess the suitability of this compound class for imaging of VGSCs. Inspired by binding studies with [^3H]BNZA using rat brain synaptosomal membranes, it was anticipated that radiolabelled 1-benzazepin-2-ones could be developed with sufficient affinity and binding potential for *in vivo* imaging of VGSCs. One of the goals for this study was to assess the organ distribution and metabolic stability of [^{125}I]**4** over a time frame suitable for imaging with PET and SPECT.

In vitro assessment of the non-radioactive, diastereoisomer mixture of the target compound (**4**) was concurrently carried out with the control -Boc derivative (**5**, Figure 22) against the human $\text{Na}_v1.2$ (*hNa_v1.2*, *SCN2A* gene) and $\text{Na}_v1.7$ (*hNa_v1.7*, *SCN9A* gene) isoform expressed in CHO cells. Compound **4** was found to block *hNa_v1.2* and *hNa_v1.7* with IC_{50} of $4.1 \pm 1.5 \mu\text{M}$ and $0.25 \pm 0.07 \mu\text{M}$ respectively whilst the IC_{50} values of **5** were $0.52 \pm 0.2 \mu\text{M}$ (*hNa_v1.2*) and $0.13 \pm 0.02 \mu\text{M}$ (*hNa_v1.7*). This suggests that the 2-iodobenzamide moiety is well tolerated in the binding site. The relative affinities of the two diastereoisomers of **4** were assessed by a [^3H]BTX displacement study. The diastereomer with the shorter retention on HPLC displaced [^3H]BTX with an IC_{50} of $0.15 \mu\text{M}$, comparable to that of **5** ($0.10 \mu\text{M}$) whereas the slower eluting diastereomer had three times lower affinity ($\text{IC}_{50} = 0.48 \mu\text{M}$). Whilst overall, these IC_{50} values for **4** were well above the low nanomolar

affinity range typically required for *in vivo* imaging, the data cannot be directly related to binding affinities as the relationship with blocking potency and [³H]BTX displacement is rather complex.

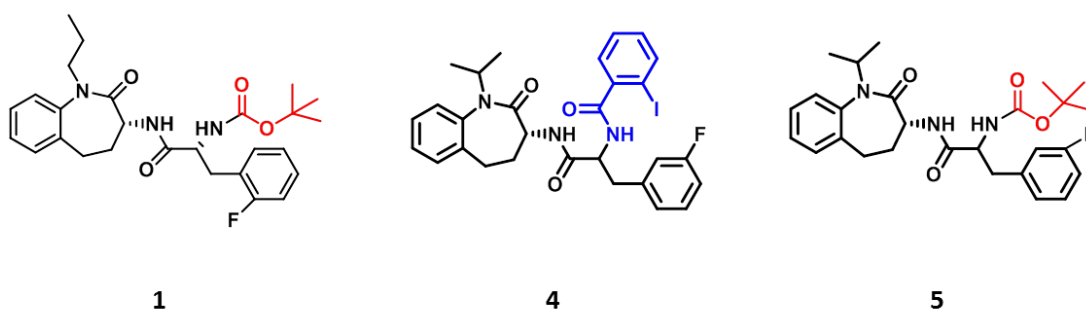


Figure 22. BNZA (**1**) and its derivatives (**4** and **5**) evaluated *in vitro*. The –Boc group and 2-iodobenzamide moiety have been highlighted in red and blue respectively.

It was important to determine the $\log D_{7.4}$ of [¹²⁵I]h-**4** as lipophilicity affects brain uptake, metabolism and protein binding.⁹³ The high lipophilicity of [¹²⁵I]h-**4** ($\log D_{7.4} = 3.93 \pm 0.01$, calculated $\log P = 5.20$) is a limitation with this study as it is likely to have impaired brain uptake. Studies have shown that for better brain penetration, $\log D$ values of potential drugs should be in the range of 1-3.⁹⁶ For compounds over this range, there is increased probability of binding to hydrophobic proteins *in vivo* other than the target which can impair clearance and reduce the ratio of specific to non-specific binding.

Furthermore, for small molecules to readily cross the BBB, their molecular weight should be in the range of 100-500.⁹⁷ Therefore another limitation of this study was the high molecular weight of **4** (612.45). Whilst having a long half-life (60 days) and thus facilitating *ex vivo* evaluations, the use of radioiodine for small molecule tracers can be problematic as it results in high lipophilicity and a significant increase in molecular weight. Therefore, substituting iodine with a radionuclide of lower molecular weight and size (for example ¹⁸F) may improve the pharmacokinetic properties and in particular, increase brain uptake. The attempts to achieve this are reported in section 3.4.3.1.

Results of the metabolite analysis showed that [¹²⁵I]h-**4** exhibited excellent stability in both plasma and brain, as it was the predominant species at all-time points.

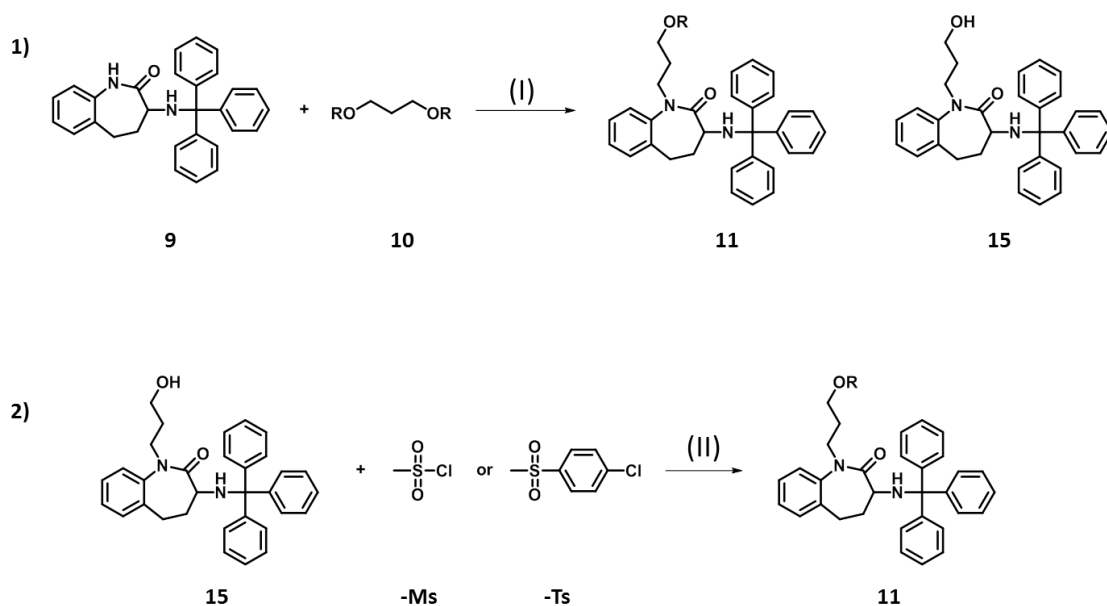
Deiodination appeared to be low, corroborating results from SPECT imaging and biodistribution, since no thyroid uptake was observed. Figure 20b illustrates how the parent compound had a longer retention time than normal for the 15 minute time point, potentially caused by a drift in the HPLC column, most likely due to a minor variation in the sample or eluent preparation.

The distribution of [^{125}I]h-**4** and [^{125}I]l-**4** was similar, with brain uptake initially moderate and gradually decreasing over time. The lack of retention in the brain implies that no specific binding to neuronal VGSCs was achieved. At later time points, the majority of the activity was found in the intestines, consistent with hepatic clearance.

Surprisingly, whilst the SPECT images overall confirmed the biodistribution results, a high uptake was observed in the interscapular region in the older animals (8-10 weeks). The clearance of [^{125}I]l-**4** from the interscapular region appeared to be faster (Figure 21, c to d), whilst for [^{125}I]h-**4** the signal persisted up until 6 hours post tracer administration (image not shown). Within this region, brown adipose tissue (BAT) is known to build up yet BAT has no known expression of VGSCs.⁹⁸ Accordingly, the high uptake of [^{125}I]**4** in the interscapular region may therefore be due to a physiological effect, or potentially, cross activity with an unknown protein. Nevertheless, the highly localized uptake of [^{125}I]**4** in the interscapular region demonstrates the potential of 1-benzazepin-2-ones for *in vivo* imaging, provided that sufficient VGSC binding affinity can be achieved. To achieve this, the next section details attempts to modify structure **4** in order to lower its lipophilicity.

3.4.3.1 [^{18}F]-Derivative of BNZA

As part of this PhD, attempts were made to synthesise a fluorinated (PET) analogue ([^{18}F]**14**) more structurally related to the parent (BNZA) compound, whilst exhibiting a lower molecular weight (482.59) and lipophilicity (calculated log *P* of **14** = 4.48) than [^{125}I]**4**. The proposed synthetic route involved radiolabelling the precursor (**11**) with ^{18}F to obtain an intermediate ([^{18}F]**12**) (Scheme 4).



Scheme 5. Attempts to obtain the precursor (**11**) for ^{18}F radiolabelling. (I): NaH (1.1 equiv.), propane-1,3-diyl bis(4-methylbenzenesulfonate) or propane-1,3-diyl dimethanesulfonate, DMF, 24 hours, 0 °C \rightarrow RT. (II): Methane or tosyl sulfonyl chloride, TEA, DCM, 90 Min.

Compound **9** was synthesised by methods that have been reported in the literature.⁹³ In one attempt, overnight reaction of **9** with either propane-1,3-diyl bis(4-methylbenzenesulfonate) or propane-1,3-diyl dimethanesulfonate in the presence of sodium hydride in anhydrous dimethyl formamide (DMF), followed by aqueous extraction and column chromatography purification did not lead to the desired product, (**11**). Proton NMR and liquid chromatography – mass spectrometry (LC-MS) revealed the hydrolysed product had been formed (**15**) for both the mesyl (Ms) and tosyl (Ts) groups. In the second attempt, **15** was reacted with either meth or tosyl sulfonyl chloride (MsCl or TsCl) for 90 minutes in the presence of anhydrous DCM and TEA. Analysis of the crude mixture by proton NMR revealed that **15** had not reacted and thus the desired product (**11**) was not formed.

Essentially, the precursor required to obtain [^{18}F]**12** was not obtained. A possible explanation for this is that **9** was incorporated onto both ends of the propane chain (**10**) and thus a dimer was produced (Figure 23). This is probable taking into consideration that although 2 equivalents of either propane-1,3-diyl bis(4-methylbenzenesulfonate) or propane-1,3-diyl dimethanesulfonate was added, this was done by drop wise addition, resulting in an initial excess of **9**.

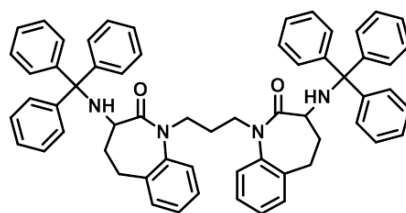


Figure 23. A possible product formed in the attempts to obtain a precursor for ^{18}F radiolabelling.

3.5 Evaluation of an Iminodihydroquinoline Tracer for Imaging of VGSCs

3.5.1 WIN17317-3

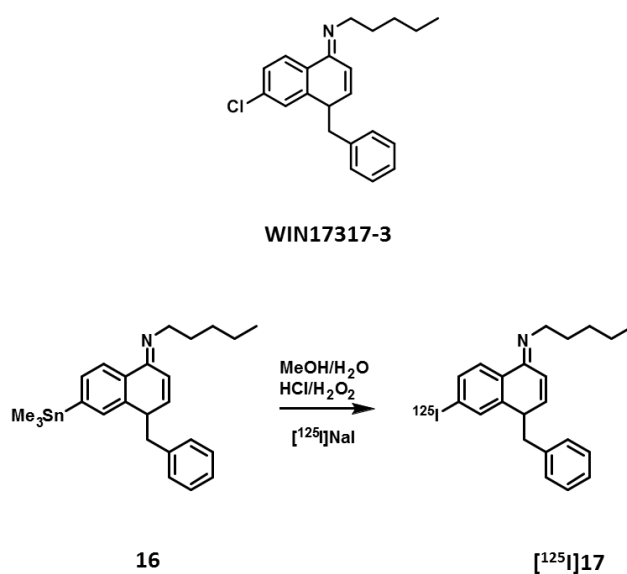
Initially, WIN17317-3 (Scheme 6) was reported to be a selective voltage gated potassium channel blocker.^{99, 100} In subsequent studies however, the binding of [^3H]WIN17317-3 to rat brain synaptosomal membranes ($K_d = 2.2 \pm 0.3$ nM) was found to be insensitive in the presence of a number of potassium channel modulators. Interestingly, several sodium channel ligands did block binding.¹⁰¹ Encouragingly, exposure of the brain preparations to [^3H]WIN17317-3 resulted in a concentration dependant association, whilst unlabelled WIN17317-3 displaced binding of its radiolabelled congener ($K_i = 1.30$ nM).

Furthermore, autoradiography of rat brain sections incubated with [^3H]WIN17317-3 revealed high specific binding to sites (cerebral cortex, substantia nigra and hippocampus) that correspond with the known distribution of VGSCs in the CNS.¹⁰¹ Electrophysiological studies using CHO cells transfected with $\text{Nav}1.2$ showed that WIN17317-3 dose dependently inhibited agonist stimulated sodium currents. As a result, WIN17317-3 represents a high-affinity ligand for VGSCs. The ability to depict VGSC distribution *in vitro* makes WIN17317-3 appealing as a lead tracer for development.

3.5.2 Results

3.5.2.1 Radioiodinated WIN17317-3 Analogue

The tin precursor (**16**) for radiolabelling with ^{125}I and the non-radioactive reference compound (**17**) were prepared by Dr C Perèz-Medina in excellent yields (37% and 25% respectively).¹⁰²



Scheme 6. ^{125}I Radiolabelling of WIN17317-3.

The radiotracer (^{125}I]**17**) was obtained by Dr C Perèz-Medina by iodostannylation of **16** with ^{125}I]NaI in the presence of dilute hydrogen peroxide for 30 min at room temperature ($58 \pm 9\%$ radiochemical yield with $>99\%$ radiochemical purity and a specific activity of $53.2 \pm 7.1 \text{ GBq } \mu\text{mol}^{-1}$, retention time on HPLC = 12.5 minutes), (Scheme 6).

Using the traditional *n*-octanol shake flask method, the $\text{Log } D_{7.4}$ of **17** was measured to be 2.98 ± 0.08 ($n = 3$) by Dr C Perèz-Medina and is within the optimal range for brain penetration.

3.5.2.2 *In Vitro* Evaluation

The iodinated reference compound (**17**) was sent for evaluation in an automated patch clamp assay using CHO cells transfected with the human (hNav1.2, *SCN2A* gene) Nav1.2 isoform. The blocking potency of **17** was $IC_{50} 1.5 \pm 0.5 \mu M$ and that of WIN17317-3 (which was included as a positive control) was $IC_{50} 2.2 \pm 1.2 \mu M$. Displacement studies with [³H]BTX using rat brain homogenates suggests that the binding affinity of **17** ($IC_{50} 21.1 \text{ nM}$) was comparable with WIN17317-3 ($IC_{50} 25.6 \text{ nM}$).¹⁰¹

3.5.2.3 Biodistribution

The distribution of radioactivity was measured *ex vivo* after *i.v.* injection of [¹²⁵I]**17** at predetermined time points (5, 15, 30 and 60 min $n \geq 3$) in female mice. At the early time points, a high uptake was observed in the kidneys and liver, which over time decreased in parallel to an increase uptake in the intestines, consistent with hepatobiliary excretion. Brain uptake was initially low ($0.48 \pm 0.04\%$ 5 min post [¹²⁵I]**17** administration) and showed no sign of retention. Clearance from the blood, heart and spleen was rapid.

	¹²⁵ I]13			
	5 min	15 min	30 min	60 min
Blood	7.17 ± 1.10	1.23 ± 0.23	0.66 ± 0.10	1.36 ± 1.55
Heart	5.70 ± 1.20	3.31 ± 0.65	2.12 ± 0.50	1.09 ± 1.91
Liver	49.43 ± 4.69	23.65 ± 5.08	10.21 ± 1.07	7.08 ± 1.3
Kidneys	61.13 ± 9.50	27.72 ± 3.30	14.25 ± 2.81	8.89 ± 1.30
Brain	0.48 ± 0.04	0.30 ± 0.06	0.14 ± 0.02	0.08 ± 0.004
Lungs	13.08 ± 3.90	6.34 ± 1.60	5.12 ± 1.10	6.00 ± 2.12
Muscle	1.83 ± 0.31	1.64 ± 0.86	1.01 ± 0.15	0.72 ± 0.16
Spleen	6.44 ± 0.65	2.63 ± 0.32	1.13 ± 0.16	0.95 ± 0.28
Bone	2.16 ± 0.36	1.00 ± 0.34	0.77 ± 0.32	0.46 ± 0.27
Small Int.	18.95 ± 5.93	34.26 ± 11.78	39.32 ± 15.27	41.10 ± 19.03
Stom. / L. Int.	6.34 ± 5.06	2.30 ± 0.80	4.23 ± 3.53	31.60 ± 19.19

Table 4. Tissue distribution of [¹²⁵I]17 expressed as %ID/g ± SD (n ≥ 3).

3.5.2.4 Metabolite Analysis

To assess the metabolic stability of [¹²⁵I]17, the composition of radioactive species in plasma and brain tissues were analysed by radio-HPLC over a period of one hour after injection. In plasma, the fraction of the intact tracer [¹²⁵I]17 was 22.8% at 5 min, 12.5% at 15 min, and 5.2% at 30 min (n = 2). At 60 min, minimal traces of [¹²⁵I]17 were detected (Figure 24). In the brain, polar metabolites were predominant at all time points, and additional metabolites of intermediate polarity along with the parent compound [¹²⁵I]17 were also observed. The low radioactivity levels recorded in the brain made quantification of the metabolite concentrations difficult.

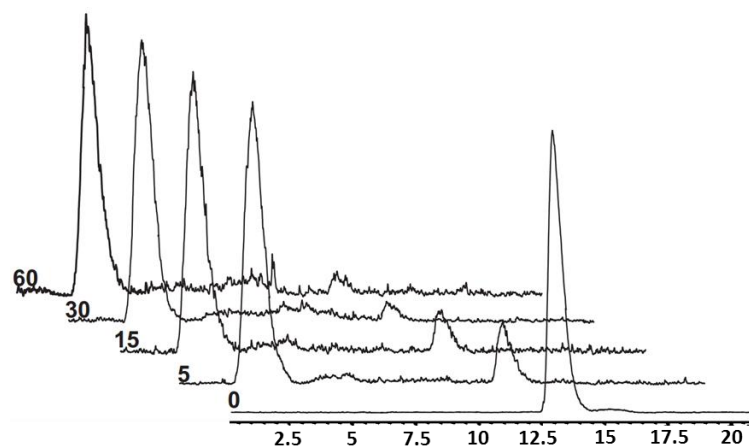


Figure 24. HPLC radioactivity profiles of plasma samples after [^{125}I]17 administration. Plasma samples were injected for HPLC analysis 5, 15, 30 and 60 min post administration of [^{125}I]17.

3.5.2.5 SPECT/CT Imaging

Whole body SPECT/CT scans were recorded following injection of [^{125}I]17 in female mice (4-10 weeks old). Similar to the biodistribution results, high radioactivity levels were observed in the liver (0-15 min post injection). At the later time points, (15-35 min post injection, Figure 25) high levels of radioactivity were observed in the intestines. Unfortunately, uptake in the brain was too low for SPECT imaging to show the regional distribution of [^{125}I]17. Low levels of radioactivity were observed in the thyroid, stomach and bladder, thus excluding de-iodination as a major metabolic route.

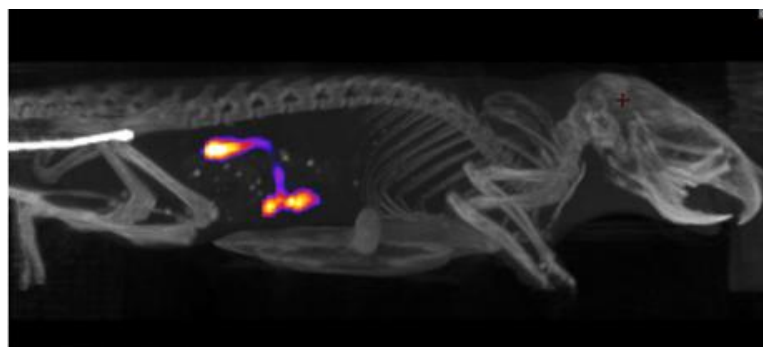


Figure 25. SPECT/CT image showing the distribution of [^{125}I]17, 15-30 min after injection. At this later time point, radioactive uptake is dominated within the intestines.

3.5.3 Discussion

The tritiated derivative of WIN17317-3 displayed high affinity to VGSCs in rat brain tissue ($K_d = 2.2 \pm 0.3$ nM) as well as successfully imaging neuronal VGSC expression in *in vitro* autoradiography.¹⁰¹ Due to these promising findings, WIN17317-3 was selected as a lead candidate for tracer development. Encouragingly, the results from the patch clamp and [³H]BTX displacement studies of WIN17317-3 and the non-radioiodinated analogue **17**, suggests that iodine is well tolerated in the binding site and that **17** largely retains the biological properties of the parent compound.

Nevertheless, (*in vivo* and *ex vivo*) biological evaluation of [¹²⁵I]**17** failed to demonstrate any binding that could be attributed to neuronal VGSCs. High accumulation of radioactivity was observed in the intestines 15 min post tracer administration. Consequently, this is highly suggestive of rapid excretion of the parent tracer and its metabolites. To rule out the possibility that the distribution pattern was the result of specific binding to VGSCs expressed in the intestines,¹⁰³ the composition of radioactivity in this tissue sample was also analysed by radio-HPLC. It was found that [¹²⁵I]**17** constituted only a minor component, with various other metabolites observed.

The metabolic stability of [¹²⁵I]**17** was very poor both in the plasma and brain. Deiodination as a major metabolic route can be excluded due to minimal uptake of radioactivity observed in the bladder, stomach and thyroid. As a result, the low metabolic stability of [¹²⁵I]**17** is likely related to the core iminodihydroquinoline scaffold, and hence compromises other derivatives of this compound class for further tracer development. This rapid metabolism provides a plausible explanation for the lack of uptake observed in the brain. However, the low activity level in the brain at 5 min post [¹²⁵I]**17** injection points to additional contributing factors, such as high protein binding or active extrusion by drug efflux pumps. It is noteworthy that the parent compound is ionized at physiological pH, which may also impair its passage through the BBB.¹⁰⁴

3.6 Conclusion

Two lead structures have been radiolabelled and evaluated as potential imaging agents for neuronal VGSCs. The two diastereoisomers of [^{125}I]4 and the ^{125}I -labelled derivative of WIN17317-3 exhibited minimal brain uptake *in vivo*.

Taking into consideration the highly localised uptake of [^{125}I]4 in the interscapular region of mice, as well as its excellent metabolic stability, attempts were made to synthesise a fluorinated derivative. It was anticipated that such a tracer, with a lower lipophilicity and molecular weight, would have improved brain uptake compared to [^{125}I]4. However, efforts to modify the BNZA structure and obtain a precursor for ^{18}F labelling were unsuccessful.

[^{125}I]17 suffered not only from poor brain uptake, but was also found to have a low metabolic stability. Essentially, these findings are important as they provide evidence to rule out this compound class for future tracer development.

Chapter 4 Multimodal Imaging of Neuroinflammation

4.1 Aims and Hypothesis

The study devised to explore the feasibility of imaging neuroinflammation with SPECT, MRI and Phosphorimaging is detailed in this chapter. The aim was to provide a more robust method for imaging Vascular Cell Adhesion Molecule-1 (VCAM-1) expression.

By radiolabelling VCAM-1 targeting antibodies conjugated to Micron Sized Particles of Iron Oxide (MPIOs), it was assumed that VCAM-1 expression could be monitored in the same animal following administration of the inflammatory cytokine TNF- α , by both SPECT/CT and MRI.

4.2 Neuroinflammation

Inflammation, defined as local reaction to injury, is the body's self-protection mechanism, with the aim to remove harmful stimuli such as damaged cells, irritants or pathogens. Leukocyte recruitment to regions of inflamed tissue is vital for the removal of these inflammatory stimuli.¹⁰⁵ When this removal is not efficient, the beneficial inflammatory response can become chronic. Therefore, the inflammation response must be well-orchestrated.

Exposure to an antigenic stimulus triggers an immune response, which involves the release of inflammatory mediators from activated T-cells and monocytes¹⁰⁵, as well as microglia in the brain.¹⁰⁶ Furthermore, supportive and regulatory glial cells such as astrocytes and oligodendrocytes in the brain and spinal cord; Schwann cells in the peripheral nerves; satellite glial cells in the dorsal root ganglia; as well as endothelial cells, can secrete immunoregulatory factors capable of mediating neuroinflammation.¹⁰⁷ Although these factors can induce beneficial effects that help to limit disease, for instance by killing infectious microorganisms, uncontrolled inflammation may amplify underlying disease states. For example, in MS, a breakdown of tolerance to self-antigens occurs by an unknown mechanism, leading immune cells to degrade the protective myelin sheath that surrounds axons.¹⁰⁷

Cerebral inflammation also occurs in various other neurological conditions, such as stroke, traumatic brain injury, brain tumours and Alzheimer's disease.

One of the critical pro-inflammatory mediators released is the cytokine Tumour Necrosis Factor – alpha (TNF- α). TNF- α stimulates endothelial cells within the inflamed microenvironment and induces the expression of cell adhesion molecules such as VCAM-1 and other endothelial adhesion molecules. VCAM-1 binds to $\alpha_4\beta_1$ integrin, which is constitutively expressed on lymphocytes, monocytes and eosinophils. Furthermore, VCAM-1 is a member of the immunoglobulin supergene family that mediates the rolling and extravasation of leukocytes across the vascular endothelium.¹⁰⁸ This is an important inflammatory event and has been implicated in the progression of epilepsy (epileptogenesis)¹⁰⁹ and may underpin development of brain tumours as VCAM-1 can be hijacked by tumour cells to aid adhesion to the vascular endothelium.¹¹⁰

VCAM-1's pattern of regulation is unique and under baseline conditions there is a low expression. In rabbits, mice and humans, VCAM-1 is rapidly induced by proatherosclerotic conditions, including in early lesions.¹¹¹ Equally, using cultured human endothelial cells, it has been shown that VCAM-1 first appears 4-6 hours after cytokine treatment.¹¹² Its maximum expression occurs 12-18 hours, then gradually declines over several days. Also, significant up-regulation of VCAM-1 is noted at a TNF- α dose of 5 $\mu\text{g}/\text{kg}$ with optimal expression occurring at 10 to 25 $\mu\text{g}/\text{kg}$.¹¹³

A biomarker can be defined as “a characteristic that is objectively measured and evaluated as an indicator of normal biological processes, pathogenic processes, or pharmacological responses to a therapeutic intervention”.¹¹⁴ As inflammation is characterised by a cascade of signalling pathways and cellular interactions acting in concert, the degree, severity and localisation cannot be ascertained using a single biomarker. Nevertheless, VCAM-1 expression is an attractive marker for inflammation as its low constitutive expression renders it an ideal target for molecular imaging. Furthermore, VCAM-1 are localised on the surface of endothelial cells within blood vessels, and can therefore be used to monitor pathology or therapies in the brain without the need for contrast agents (CA) to cross the BBB.

Recently, the development of Micron sized Particles of Iron Oxide (MPIOs) coated with VCAM-1 targeting antibodies as CA for imaging VCAM-1 expression with MRI has been a major technological advance, as it enables neuroinflammation to be detected and localised with exquisite sensitivity and specificity.¹¹⁵⁻¹²⁰ This has expanded the MRI landscape to enable imaging of molecular events *in vivo*, a domain traditionally restricted to optical techniques and imaging with SPECT and PET. Iron oxide particles can provide image contrast due to unpaired electrons (4 for Fe²⁺ and 5 for Fe³⁺) in the outer shell of the iron atoms giving it superparamagnetic properties that can distort magnetic fields. MPIOs provide marked contrast attributed to the sizable payload of iron oxide which results in regions of hypointensities up to 50 times the physical diameter of the microparticle.¹¹⁵

4.3 Study Outline

In order to identify the potential of SPECT for imaging of neuroinflammation and to explore the value of complimentary multimodal imaging, VCAM-1 targeting MPIOs were radiolabelled with iodine-125. To characterise this imaging agent for *in vivo* neuroimaging, its biodistribution and blood clearance properties have been investigated. This radiolabelled CA was then evaluated in a rat model of cerebral inflammation based on intra-striatal injection of TNF- α . To ensure that inflammation was induced by TNF- α and not the injection procedure itself, saline was injected in place of TNF- α for the control groups. Equally, to control for non-specific binding, isotype matched, generic antibodies (IgG) were conjugated to MPIOs, radiolabelled and evaluated in TNF- α treated rats. Experimental details for this study can be found in chapter 8.

MPIOs were purchased commercially as Dynabeads[®] MyOne[™] tosyl-activated particles consisting of polystyrene beads coated with a polyurethane layer. Briefly, the hydroxyl groups found on this coating are activated by reaction with p-toluensulphonyl chloride. The resulting sulphonyl ester can react with proteins or ligands containing sulfhydryl or amino groups (Scheme 7). In this study, the monoclonal antibodies conjugated to MPIOs were radiolabelled with ¹²⁵I.



Scheme 7.

Unless stated otherwise, [^{125}I]VCAM-MPIO or [^{125}I]IgG-MPIO was administered 7 hours after rats were treated with TNF- α whilst [^{125}I]VCAM-MPIO was injected in rats that received saline in place of TNF- α . The CA (5 mg of iron per kg of animal weight, which approximately equates to 19.2 mg of tosyl activated Dynabeads, 4×10^8 particles¹¹⁵, 30-150 MBq) in heparinised phosphate-buffered saline (1 mL, pH 7.4), was delivered via a cannula inserted into the right external jugular vein.

In this collaborative study, the quantification represented in Figure 30 was obtained by Dr B Duffy who also performed the intra-cerebral injections, as well as processing the MRI images for co-registering with SPECT.

4.4 Results

4.4.1 Conjugation Radiochemistry

As the iron content in MPIOs is responsible for the signal hypointensities on MRI images, the percentage of iron was normalised to the weight of animal (in kg) when determining the amount of MPIOs to use for each animal. After conjugation, the final product was anti-VCAM-1 antibodies bound to MPIO and henceforth will be referred to as VCAM-MPIO. The radiolabelled CA was obtained directly from antibody coated MPIOs by incubation with [^{125}I]NaI in pre-coated iodogen tubes. ^{125}I was introduced onto tyrosine residues present on the antibodies and isolated by magnetic immobilisation to give [^{125}I]VCAM-MPIO in $85 \pm 5\%$ ($n = 11$) radiochemical yield.

4.4.2 Blood Clearance and Biodistribution

In healthy rats, [125 I]VCAM-MPIO displayed rapid kinetics and was effectively cleared from the blood pool 2 min post-injection (Figure 26a). Within 10 min, the CA accumulated in the lungs (4.8 ± 1.3 %ID/g), spleen (3.4 ± 1.4 %ID/g) and liver (1.5 ± 0.5 %ID/g), with negligible uptake in the brain (0.016 ± 0.005 %ID/g) (Figure 26b). The low radioactivity levels in the bladder and thyroid, as seen by whole body SPECT/CT (Figure 26c), suggest that [125 I]VCAM-MPIO remains largely intact after administration *in vivo*.

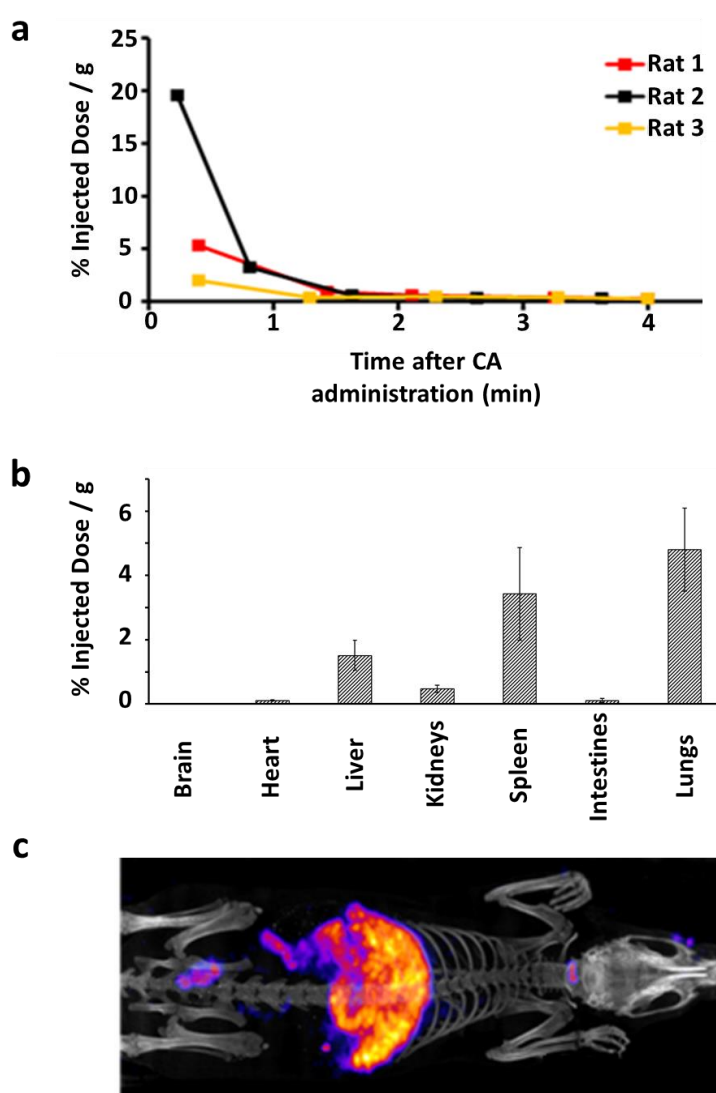


Figure 26. (a) Blood clearance and (b) *ex-vivo* biodistribution of [125 I]VCAM-MPIO in healthy rats. For biodistribution studies, the animals were euthanized 10 min post tracer administration and the results displayed are averaged ($n=3$) \pm SEM. (c) *In vivo*, biodistribution of [125 I]VCAM-MPIO, (whole body SPECT/CT maximum intensity projection), 20 min post CA administration (5 mg Fe/kg, 0.2 MBq/g per gram).

4.4.3 Dose Optimisation

In order to facilitate sequential imaging with SPECT/CT and MRI in individual animals, dose optimisation studies were performed in rats that were injected with TNF- α in the right striatum to induce inflammation. Although in preliminary studies 2 mg of Fe/kg of [¹²⁵I]VCAM-MPIO (0.043 MBq/g) was sufficient for imaging with SPECT/CT, this concentration appeared to be too low to give discernible hypointensities with MRI (Figure 27a). Therefore, higher doses of MPIO were used to determine the optimum concentration for MRI. The MRI contrast effect seemed dependant on the amount of [¹²⁵I]VCAM-MPIO administered, and was only apparent at higher doses of iron oxide (Figure 27b and c). At 5 mg Fe/kg, there was a pronounced difference between TNF- α treated animals, animals sham treated with saline, and TNF- α treated animals that received non-specific CA (IgG-MPIO). A few hypointensities were noted in the brains from the two control groups, most likely due to dephasing from the vasculature (Figure 27d and e). At the optimised concentration of iron oxide (5 mg Fe/kg), imaging with SPECT/CT showed localised binding of the CA in the brains of TNF- α treated animals, consistent with neuroinflammation, when using radioactivity levels at both a low and high range (0.20-0.25 and 0.70-0.90 MBq per gram of body weight, Figure 27f and g). In the TNF- α group, 0.23 MBq/g resulted in a clear difference between the signal from the brain and the extracranial regions (Figure 27f). No CA binding could be detected in the brains of animals from the control groups with SPECT (Figure 27h and i). Instead, at both the low (0.25 MBq/g) and high (0.71 MBq/g) levels of radioactivity, signals from the extracranial region dominated.

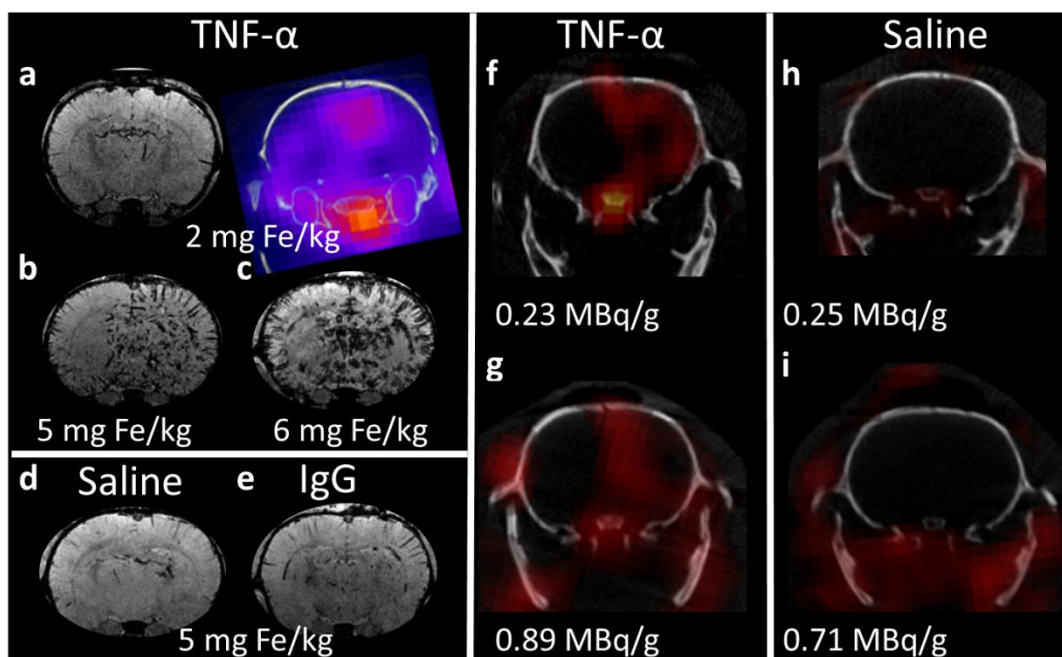


Figure 27. Dose optimisation studies of [^{125}I]VCAM-MPIO for *in vivo* imaging. (a) Coronal MRI and SPECT/CT images and (b-c) coronal MRI images demonstrating binding of [^{125}I]VCAM-MPIO (0.043 MBq/g) at different doses of iron oxide (2, 5 and 6 mg Fe/kg), administered 7 hours after intra-cerebral TNF- α injection. The optimum dose of iron oxide (5 mg Fe/kg) was assessed in two control groups by MRI; (d) Rat sham treated with saline; (e) TNF- α treated rat administered IgG-MPIO. SPECT/CT imaging was performed 20 min after administration of [^{125}I]VCAM-MPIO (5 mg Fe/kg, 0.23-0.9 MBq/g) in animals treated with (f and g) TNF- α or (h and i) saline. SPECT/CT imaging was conducted on animals which received (f and h) a low radioactive dose and on animals administered with (g and i) a high radioactive dose of the CA.

4.4.4 Qualitative Comparison of MRI, SPECT/CT and Phosphorimaging

To facilitate qualitative comparison between the data, MRI images were co-registered with CT enabling SPECT images to be overlaid on the MRI (Figure 28a-d). In TNF- α treated rats ($n=4$), the hypointensities present on MRI were in good agreement with the SPECT signals in the brain, and also correlated well with phosphorimaging of cryosections from the site of TNF- α injection (Figure 28e and f). Interestingly, in the saline treated control group, phosphorimaging showed localised uptake of the CA at the injection site, suggesting that the sham treatment also induced local inflammation (Figure 28g). The low and homogenous radioactivity levels observed with phosphorimaging in brains from animals that received [^{125}I]IgG-MPIO confirms that non-specific binding of the CA is negligible (Figure 28h).

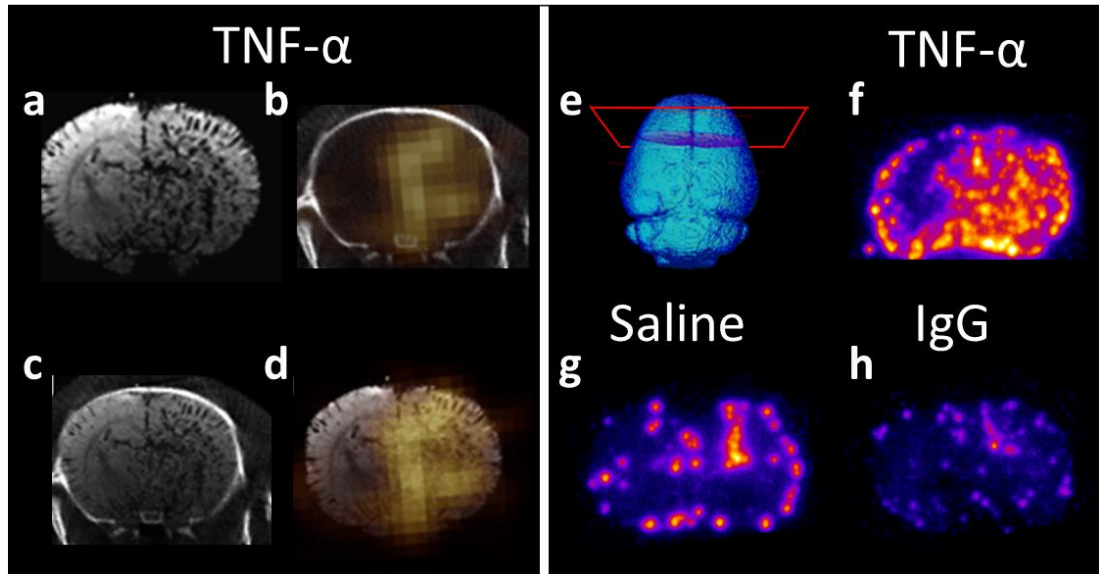


Figure 28. Multimodal imaging of VCAM-1 expression in a TNF- α treated rat using [^{125}I]VCAM-MPIO (5 mg Fe/kg, 0.25-0.90 MBq/g). (a): Coronal MRI image, (b): Coronal SPECT/CT image, (c): Co-registration of MRI and CT images, (d): SPECT overlaid on MRI image; (e) Representation of the coronal sections from the plane of injection; (f) Phosphorimages of brain sections with [^{125}I]VCAM-MPIO in TNF- α treated rat, (g) a saline sham treated rat, and with (h) [^{125}I]IgG-MPIO (5 mg Fe/kg, 0.2 MBq/g) in the TNF- α model.

4.4.5 Quantitative Comparison of MRI and SPECT

For MRI, local thresholding performed well for the segmentation of hypointense regions (Figure 29).

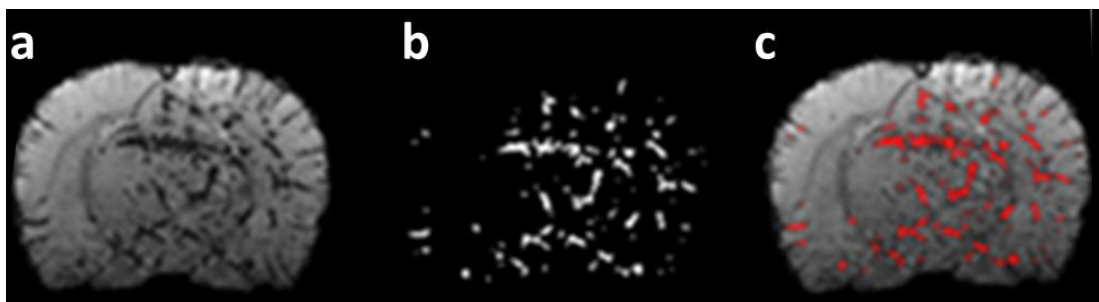


Figure 29. Illustration of the procedure for MRI quantification. (a) Brain extraction; (b) hypointense regions segmented using local thresholding; (c) segmented regions overlaid in red upon the original MRI image.

Injection of TNF- α into the right striatum induced widespread inflammation, which included the left hemisphere (Figure 30a and b). For this reason, the total signal from [125 I]VCAM-MPIO in the whole brain, as well as in the two hemispheres was determined for quantitative comparison between the data obtained with MRI and SPECT/CT. By comparing the signal in the two brain hemispheres, bias from manually defining ROIs is avoided. Furthermore, direct comparisons between the two hemispheres enables differences in the data obtained with MRI and SPECT to be highlighted.

Quantification of both MRI and SPECT signals revealed higher CA binding in TNF- α treated animals compared to the two control groups, globally as well as in each of the brain hemispheres (Figure 30c-e). Therefore, there is overall good agreement between the two modalities. Nevertheless, MRI analysis indicated more pronounced difference in CA uptake between the left and right hemispheres in the TNF- α group: the difference in the group means when comparing CA uptake in the right hemisphere reached a significance of $p = 1 \times 10^{-6}$ with MRI, but only $p = 0.045$ with SPECT (Figure 30e). Quantification of signals observed on the cryo-sections from phosphorimaging was unfortunately not feasible, because the radioactivity levels that were used for imaging with *in vivo* SPECT/CT were too high.

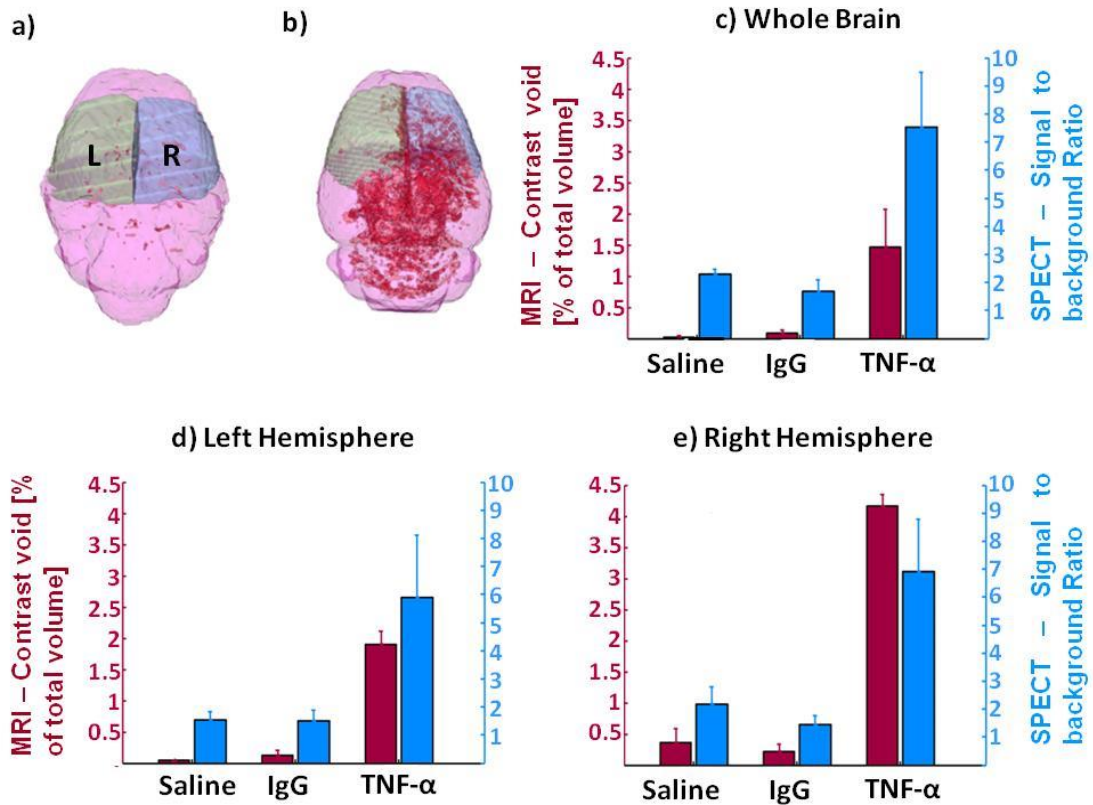


Figure 30. 3-D representation and quantification of CA binding. 3D representation of CA binding (VCAM-MPIO, 5 mg Fe/kg) based on *in vivo* MRI images for the (a) saline control group and (b) the TNF- α treated group. This was produced by Dr B Duffy. Segmented hypointense regions are shown in red, whilst the green and blue areas indicate the left and right brain regions (respectively) used for quantification. MRI quantification has been achieved by determining the percentage of hypointense signals within the ROI volume (either left, right or whole brain). C-e: Quantification of CA binding as assessed by *in vivo* MRI (red) and *in vivo* SPECT (blue). Quantification was carried out over the (c) whole brain as well as the (d) left and (e) right cerebral hemispheres. Following intracerebral saline (n=3) or TNF- α injections (n=4), animals were administered [125 I]-VCAM-MPIO or [125 I]-IgG-MPIO (n=3) (5 mg Fe/kg, 0.23-0.9 MBq/g).

In the TNF- α group, dynamic imaging with SPECT using 5 min frames from 20 to 45 min post-injection revealed that [125 I]VCAM-MPIO binds strongly to the brain (Figure 31).

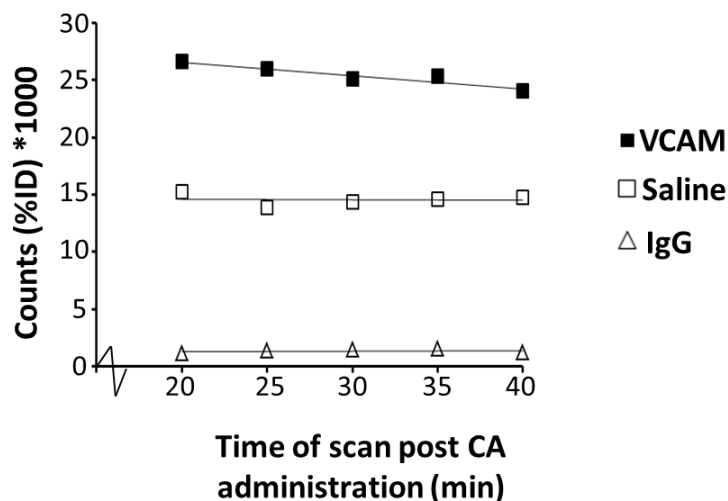


Figure 31. Dynamic SPECT (5 min frames) from 20-45 min following administration of the CA (5 mg Fe/kg, 0.20 MBq/g). For each group, the quantification from a representative animal is shown. Quantification was performed across the whole brain.

4.4.6 Distribution of [¹²⁵I]VCAM-MPIO within the Brain Vasculature

To determine the distribution of [¹²⁵I]VCAM-MPIO within the brain vasculature, one TNF- α treated rat was administered a reduced dose of [¹²⁵I]VCAM-MPIO (3 Fe/kg, 30 KBq/g). Phosphorimaging of brain cryosections (obtained 1 hour after CA administration) revealed a highly heterogeneous distribution, with the CA predominately confined to large blood vessels (Figure 32a). This was consistent with the pattern of hypointensities observed with MRI (Figure 32b) on slices both anterior and posterior to the bregma (Figure 32c). Whether the CA localised on vessels on the arterial or venous side of the circulation was not determined in this study. However, several large vessels indicative of major arteries were identified. These include the anterior striate arteries (astr), anterior choroidal arteries (ach), transverse hippocampal arteries (trhi), the supracollicular network (scol),¹²¹ as well as the choroidal artery. The prominent vessels which lie on the dorsal surface of both hemispheres also contained high levels of the CA.

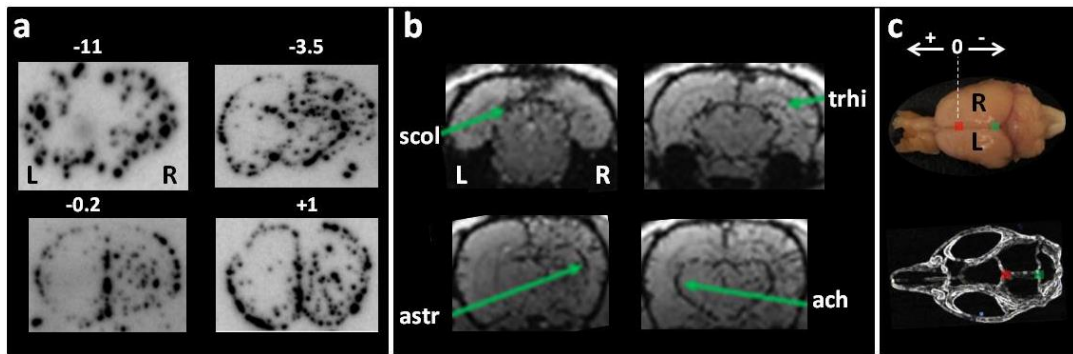


Figure 32. CA distribution within the brain vasculature. (a) Phosphorimages of coronal brain sections (20 μ m) from a TNF- α treated animal administered [125 I]VCAM-MPIO (3 mg Fe/kg, 30 KBq/g). The sections anterior (+) and posterior (-) relative to the bregma have been indicated in mm and the animal was culled 40 min after CA administration. (b) Coronal MRI images from a separate study of a TNF- α treated rat administered [125 I]VCAM-MPIO (5 mg Fe/kg, 0.20 MBq/g) showing uptake in large blood vessels. *In vivo* MRI was conducted approximately 40 min after CA administration. (c) The approximate locations of the bregma (red) and lambda (green) shown on a rat brain, and on the skull which were used as indicators to ensure that intra-cerebral injections (of TNF- α or saline for controls) on each animal was at the same co-ordinates, which was always located at the right brain hemisphere.

4.5 Discussion

The assessment of radiolabelled, VCAM-1 targeting micro-sized particles of iron oxide, in a model of neuroinflammation has revealed for the first time, its potential as a multi – modal imaging agent; conspicuity of the CA was not only evident by MRI, but was also seen with SPECT/CT and phosphorimaging. *In vivo* quantification of both the MRI and SPECT signals in the affected right brain hemisphere revealed that binding of [125 I]VCAM-MPIO was almost four times higher in the disease model, (TNF- α treated animals), compared to the two controls.

From the synthesis perspective, the presence of superparamagnetic iron oxide enabled rapid and efficient purification of the radiolabelled CA. The simplicity and highly practical nature of this method means that it can easily be adopted for radiolabelling and purifying MPIO/antibody constructs with shorter lived, higher energy, gamma emitting radionuclides such as 123 I.

MPIOs were selected primarily due to their exquisite sensitivity by the contrast “blooming effect”; a phenomenon where the effects of MPIO on local magnetic field

homogeneity and detectable contrast extend 50 times the physical diameter of the microparticle.^{122, 123} p-Toluenesulfonyl (tosyl) activated MyOne™ Dynabeads® were used due to their large binding capacities (0.04-0.06 mmol/g) and the ease by which they can be conjugated to primary amine or sulfhydryl groups on antibodies, producing high yields. This strategy has been reported in several *in vivo* VCAM-1 targeting studies¹¹⁵⁻¹²⁰, suggesting that their physiochemical properties are suitable for *in vivo* imaging.

The manufacturers' specifications state that per mg of MyOne™ Dynabeads®, 14-19 µg of whole antibodies can be conjugated, which in the best case scenario, equates to approximately 173 pmol per mg of particle (or 104,180 antibodies per particle). For the synthesis of VCAM-MPIO, 40 µg of antibody were used in the conjugation reaction per mg of iron/MPIO (Fe-MPIO), and the final radiochemical yield of [¹²⁵I]VCAM-MPIO was excellent (85 ± 5% n = 11). An excess of antibody was used for the conjugation in order to account for factors that may impede binding between the amine or sulfhydryl groups on the antibody with the tosyl activated groups on the particles, such as steric hindrance or hydrolysis of the tosyl functional group.

Kinetic studies revealed that [¹²⁵I]VCAM-MPIO binds strongly within the brain vasculature and clears rapidly (within minutes) from the blood pool, which is in good agreement with previously published results.^{124, 125} Due to this rapid clearance, *in vivo* imaging was performed soon after CA administration in order to maximise the signal-to-background ratio. It is noteworthy that efforts to develop particle-derived radiotracers have focused considerably on nanoparticles.^{126, 127} However, nanoparticles typically exhibit blood clearance rates on the order of hours or days.¹²⁸ Accordingly, these results suggest that micron-sized particles could improve image contrast compared to vascular-targeted nanoparticles. Moreover, by validating the rapid clearance of micron-sized imaging agents, there is now further scope for their use with a wider range of radionuclides, including short-lived positron emitters, such as ⁶⁸Ga and ¹⁸F for imaging with PET.

To obtain blood for the kinetic study, a cannula was implanted into the right external jugular vein of the rats.¹²⁹ This permitted sufficient volumes of blood to be withdrawn and then to be replaced with an equivalent volume of saline. Replacing

the sample volume ensured that repeated withdrawals were possible without compromising blood volume.

Biodistribution studies in healthy rats showed high uptake of [125 I]VCAM-MPIO in organs known to clear iron oxide particles.¹³⁰ The high accumulation in the lungs displays pulmonary first pass effect, whilst high liver and spleen uptake displays clearance of the iron oxide particles by the reticuloendothelial system. The high lung uptake observed in *ex vivo* biodistribution was not observed in the *in vivo* image (Figure 26). This discrepancy is likely due to differences in how radioactivity is measured with the two techniques: in *ex vivo* biodistribution, radioactivity is correlated to the weight of the tissue samples (%ID/g), whereas *in vivo* SPECT imaging reflects activity per volume. As the lungs contain a high proportion of air, they may contain high activity levels relative to their weight, yet fairly low activity levels relative to their volume. Fundamentally, the *in vivo* and *ex vivo* biodistribution revealed that uptake in the thyroid and bladder was minimal, suggesting that the rate of deiodination from the particle was low and hence good stability of the CA.

SPECT/CT imaging was conducted approximately 20 minutes after CA administration, followed by MRI (which commenced roughly 1 hour after CA administration). To allow sequential imaging with SPECT/CT and MRI in individual animals, dose optimisation studies were performed in rats that were pre-treated with TNF- α . Marked hypointensities in TNF- α treated rats were only observed at high concentrations, with 5 mg Fe/kg appearing to be the optimal dose. It is worth noting that incorporating iodine-125 on the antibody may reduce the binding affinity of the iron oxide particles to the target antigen. Determining the effects (if any) of radiolabelling on the affinity of VCAM-MPIO will provide a better indication of how sensitive the technique is. Quantifying the observed MRI signals at different MPIO doses and keeping the amount of radioactivity consistent will help to achieve this.

At the optimised concentration of MPIOs for MRI (5 mg Fe/kg), imaging with SPECT/CT showed localised uptake of CA in the brain, consistent with neuroinflammation. Promisingly, this was apparent when using radioactivity levels as low as 0.25 MBq per gram of animal weight. Dynamic imaging with SPECT using 5 min frames from 20 to 45 min post-injection revealed that [125 I]VCAM-

MPIO binds strongly to the brain vasculature, with no change in the global radioactivity levels observed over this period of time (Figure 31).

In TNF- α treated rats ($n = 4$), considerably more CA was detected compared to the control groups; the hypointensities present on MRI were in good agreement with the SPECT signals in the brain, and also correlated well with phosphorimaging of cryosections from the site of TNF- α injection. In particular, MRI and phosphorimaging showed that in the TNF- α group, the CA tended to localise to larger vessels in favour of smaller ones. Further work will be needed to determine how faithfully this reflects the distribution of the VCAM-1 receptor in the brain's pathological state or whether this phenomenon might to some extent be due to blood flow.

Any discrepancies in the results, especially in terms of quantification between SPECT and MRI were in part due to the use of iodine-125. Attenuation and scatter of the low energy gamma rays (35.5 KeV) makes iodine-125 poorly suited for *in vivo* imaging. Attenuation is likely to have affected the results from the TNF- α group, where inflammation is most pronounced within deeper brain tissues. Despite this limitation, imaging of [125 I]VCAM-MPIO with SPECT/CT enabled inflammation to be detected and localised at least in the outer regions of the rat brain, using moderate amounts of radioactivity and short imaging sequences (5 min frames). The use of iodine-123, which emits higher energy gamma rays (159 KeV), will provide improved image quality and also allow imaging of deep brain tissue; however it is worth noting that the half-life of 13 h makes it less practical than iodine-125, and it is also more costly to use.

4.6 Conclusion

Using a highly efficient, practical method to label antibody-MPIO constructs, a versatile imaging probe has been synthesised and characterised in a neuro-inflammatory model based on intra-cerebral administration of TNF- α . The conspicuity of the CA was not only evident by MRI, but was also seen with SPECT/CT and phosphorimaging, which showed increased binding of [125 I]VCAM-MPIO in the brains of TNF- α treated rats. This, to our knowledge, is the first study to

employ SPECT for imaging of VCAM-1 expression. The optimisation studies highlighted that as expected, the absolute sensitivity of SPECT is superior to that of MRI. Nonetheless, with optimal dose of CA, the MRI appeared to provide better and more defined contrast than SPECT. This demonstrates the value of cross-validation, and the importance of multi-modal, complimentary imaging.

Chapter 5 Multimodal Imaging of Seizure-Induced Inflammation

5.1 Aim and Hypothesis

In the follow up study described herein, the goal is to assess if [¹²⁵I]VCAM-MPIO can detect cerebral inflammation that occurs after status epilepticus (SE) and thus characterise the imaging agent in a pre-clinical model which more closely resembles human disease, compared to the cerebral inflammatory model used in chapter 4.

In spite of intensive efforts, there is currently no biological marker predictive for seizure outcome. This Holy Grail for *in vivo* imaging research would make it possible to identify patients at high risk for developing epilepsy after a predisposing insult such as head injury or stroke. The subsequent sections discuss attempts to identify neurobiological processes or receptors that could be useful predicative markers for seizure outcome. It was hypothesised that the radiolabelled CA developed in chapter 4 could enable MRI and SPECT imaging of VCAM-1 expression in the same animal, and thus provide further information about the neurological changes which occur after SE.

5.2 Epilepsy

Epilepsy is a group of neurological disorders characterised by recurrent seizures or an enduring predisposition to generate seizures. A seizure is an abnormal electrical discharge in the brain that causes alteration in consciousness, sensation and/or behaviour. Epileptic seizures can be classified as partial (60% of cases) or generalised (40% of all epilepsies), in which the former refers to epileptic activity originating focally in the brain whereas the latter relates to seizure activity involving both cerebral hemispheres from the outset.¹³¹

Temporal lobe epilepsy (TLE) is the most common form of partial epilepsy associated with atrophy of mesial temporal structures.¹³² The most common structural abnormality in TLE is observed in the hippocampus, which involves neuronal loss and gliosis (hippocampal sclerosis).

Despite the wide range of available anti-epileptic drugs (AEDs), about one third of individuals with epilepsy still experience seizures, and do not respond to medication.¹³³ There is thus a pressing need for more effective therapies to exist, especially since current AEDs are mainly symptomatic: they inhibit seizures but do not tackle the underlying pathology or progression of the disease.^{134, 135} Elucidating the mechanisms involved in the generation of epilepsy should aid the development of novel, therapeutic drugs that modify the epileptic process.

The term epileptogenesis is used to describe the complex changes in the brain that following a precipitating insult or injury, convert a normal brain into a brain debilitated by recurrent seizures.¹³⁶ For example, TLE often ensues after an identifiable cerebral insult such as febrile seizures, prolonged seizures (status epilepticus, section 5.2.1), hypoxia-ischemia or head injury. Febrile seizures are associated with fever in the absence of other precipitating events, such as central nervous system infection or electrolyte imbalance.¹³⁷

The epileptogenesis process can be broken down into three main stages: 1) the initial precipitating event; 2) the latent period; and 3) the chronic period with spontaneous seizures.¹³⁶ The latent period offers a window of opportunity for testing interventions in patients at high risk for epilepsy. Nonetheless, there is no definite marker to identify such patients and consequently this study explores if VCAM-1 could be a suitable option. The motivation for selecting VCAM-1 stems from experimental and clinical evidence proposing that inflammatory processes in the brain may constitute a vital mechanism in the pathophysiology of seizures and epilepsy.¹³⁸ In particular and as mentioned in chapter 4, VCAM-1 mediates the rolling and extravasation of leukocytes across the vascular endothelium¹⁰⁸: an important inflammatory event that has been implicated in epileptogenesis.¹⁰⁹

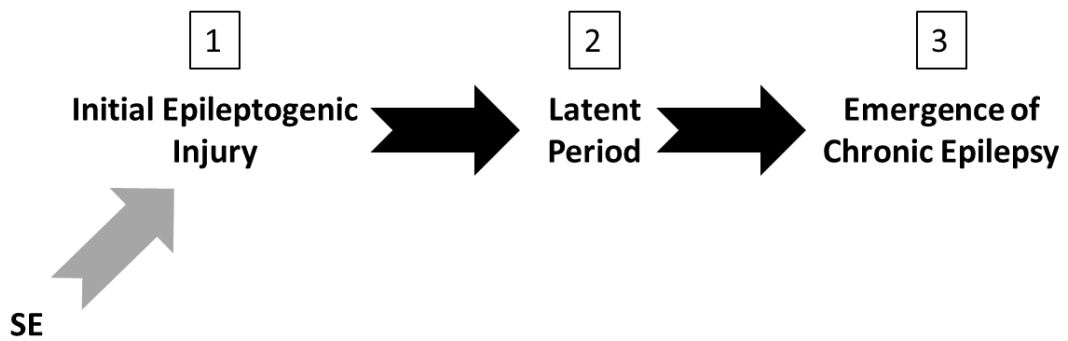


Figure 33. The stages of epileptogenesis following SE. SE-induced neuronal injury activates diverse signalling events, such as inflammation, oxidation, apoptosis, neurogenesis and synaptic plasticity, which eventually leads to structural and functional changes (stage 1).¹³⁶ These changes are progressive, causing rearrangement of synaptic circuitry, neurogenesis and hyperexcitability over weeks, months or years (stage 2). These changes eventually manifest as spontaneous recurrent seizures (epilepsy) in susceptible individuals (stage 3).

5.2.1 Status Epilepticus

Status Epilepticus (SE) can be defined as a continuous seizure lasting more than 30 min; however during the past 10 years there has been considerable rethinking about the precise duration that a seizure must last for it to be designated as SE.¹³⁹ Therefore, the definition of SE in the World Health Organisation’s *Dictionary of epilepsy* is “a condition characterised by an epileptic seizure that is sufficiently prolonged or repeated at sufficiently brief intervals so as to produce an unvarying and enduring epileptic condition.”¹⁴⁰ There are numerous forms of SE, resulting in various types of seizures.¹⁴¹ Uninterrupted convulsive status epilepticus (CSE) is thought to cause brain injury or even lead to chronic epilepsy. For example, in one study it was found that the risk of unprovoked seizures in patients was 3.3 fold higher after CSE than after a single brief seizure.¹⁴² Nevertheless, it is noteworthy that CSE does not necessarily cause epilepsy as a prolonged seizure may be indicative of substantial brain injury already present at the time of the initial seizure.

5.2.2 Animal Models

Investigating early epileptogenic processes in the clinical setting is challenging as currently, epilepsy is diagnosed after the onset of recurrent seizures, which represents the culmination of epileptogenesis.¹⁴³ Animal models provide the opportunity to rigorously evaluate the epileptogenic process and thus can be valuable for increasing our understanding and identifying early biomarkers of this disease.

Innumerable models of epilepsy and epileptic seizures have been described in the literature.¹⁴⁴ Experimental models have been developed that mimic the continuous seizure state or SE. Such models are used to study: the transition of a single episode of SE into chronic epilepsy; the mechanism of neuronal injury; synaptic reorganisation (sprouting); hippocampal sclerosis; and the development of new anti-convulsant drugs.¹³⁶ In addition, SE is the most widely used approach for inducing chronic epilepsy, with the SE episode considered a trigger to initiate epileptogenesis that will culminate into TLE.

Animal models used for chronic epilepsy can fall under two main types: genetic and acquired, both of which allow investigations at all stages of the disease. Of the two, the focus of this chapter and chapter 6 is on acquired epilepsy models. Models of acquired epilepsy can be established either by chemical or electrical induction. As part of this research, acquired epilepsy models have been established via the administration of pilocarpine, and the experimental details of this have been outlined in chapter 8. It is important to note that because human SE is a complex neurological disorder that encompasses many causes and seizure phenotypes, it is highly likely that no single animal model is capable of mimicking the full spectrum of clinical SE features. Overall, models of acquired epilepsy to some extent reproduce the pathophysiological alterations that are identified in patients with this disease.

Pilocarpine can induce SE by activating the M1 muscarinic receptor subtype and is currently one of the most widely used models of chronic epilepsy.¹⁴⁵ Some important features of the pilocarpine model are:

- More rapid induction of self-sustaining SE compared to intraperitoneal (i.p.) administration of kainic acid: another convulsant drug commonly used to reproduce chronic epilepsy in rodents¹⁴⁶

- Substantial injury to the piriform and entorhinal cortices, amygdala, CA1 and CA3 sub regions of the hippocampus, hypothalamus and sub regions of the thalamus following self-sustaining SE
- The presence of a latent (seizure free) period of several weeks, followed by the appearance of spontaneous recurrent seizures (SRS)

As observed in the human condition¹⁴⁷, there appears to be a strong positive correlation between mortality and age in the pilocarpine model of SE.¹⁴⁸ In fact, in both species, the immature brain seems to be more susceptible to seizures whilst displaying a high degree of resistance to neuronal injury.¹⁴⁶

Variations of the pilocarpine model have been established, namely the lithium-pilocarpine model of SE.¹⁴⁹ Pre-treatment with lithium chloride 24 hours before the initiation of SE allows a conspicuous reduction of the pilocarpine dose (approximately ten-fold). Essentially, the neuronal damage observed in the lithium-pilocarpine model post SE have been similar to that reported in the high-dose pilocarpine models.¹⁵⁰ Moreover, the rate of success in developing SE after lithium pre-treatment has been reported to be 100%; a considerable improvement when compared to the high-dose pilocarpine model (60%).¹⁵¹ In general, there is a lower mortality rate with lithium-pilocarpine treated rats¹⁵² and this can be further reduced by the administration of diazepam to terminate seizures 60-120 min after the induction of SE.¹⁵³

Seizure severity in rodents can be assessed using behavioural scoring. This circumvents the implantation for more labour intensive electroencephalography (EEG) electrodes. The Racine scale is the accepted scoring method for limbic seizures and is composed of five stages:¹⁵⁴

1. Mouth and facial automatisms
2. Head nodding or wet dog shakes
3. Unilateral/bilateral forelimb clonus
4. Forelimb clonus with rearing
5. Rearing and falling

Partial seizures are at times considered to be stages 1 and 2, whilst the latter stages (3-5) are associated with generalised seizures.¹⁵¹ Often, the onset of self-sustaining SE is defined as stage 3 on the Racine scale.^{155, 156}

5.3 Neuroimaging the Epileptogenic Process

Neuroimaging has enabled researchers to identify *in vivo* changes during epileptogenesis as well as monitor treatment responses through serial acquisitions in the same patient.¹⁴³ Numerous approaches to identify early biomarkers involved in epilepsy and to study related pathology have emerged for pre-clinical and clinical investigations. For example, impairment of the BBB, a hallmark of epileptogenesis¹⁵⁷, can be visualised by systemic injection of imaging agents that under physiological conditions do not cross the intact BBB (e.g. gadolinium based contrast agents for MRI).¹⁵⁸ Furthermore, structural MRI has been valuable for revealing volumetric and morphological changes in the hippocampus and other limbic structures in SE models,^{159, 160} whilst functional MRI (fMRI) has been useful for evaluating the abnormalities in neural activity and circuitry introduced in epilepsy.¹⁶¹

Nuclear imaging, in particular PET, is proving to be a promising technique in epilepsy research.¹⁶² Fluorodeoxyglucose (2-deoxy-2[¹⁸F]fluoro-D-glucose, [¹⁸F]FDG), which maps glucose uptake and metabolism has been at the forefront of radiotracers used for PET. FDG is taken up by cells in a similar manner to glucose but it is not metabolised further after phosphorylation by hexokinase. As a result, FDG gets trapped in cells and thus provides an indication of glucose utilisation in the cell/region of interest. During seizures, it has been reported that [¹⁸F]FDG uptake is increased in several brain regions, most notably in the ventral and dorsal hippocampus (by 2.3 and 1.6 fold respectively), as well as the entorhinal cortex.¹⁶³ Such findings have been routinely reported¹⁶⁴ and demonstrate the usefulness of PET for detecting elevated neuronal activity during seizures. Hypometabolism in the epileptogenic zone during the interictal state (the intervals between convulsions or seizures) is a well-described phenomenon in humans with temporal lobe epilepsy.¹⁶⁵ One recent study has suggested that whole brain [¹⁸F]FDG uptake was dramatically

reduced as early as 24 h after kainic acid treatment, before and independently from hippocampal volume loss and the onset of spontaneous recurrent seizures (SRS).¹⁶² However at this infant stage, there is insufficient data to conclude whether [¹⁸F]FDG hypometabolism is a biomarker for the development of SRS.

One of the most commonly used target for imaging in epilepsy patients is the 18 kDa translocator protein (TSPO), formerly known as peripheral benzodiazepine receptor (PBR). Under physiological conditions, TSPO expression in the brain is relatively low and is found predominantly in ependymal cells lining the ventricles, in cells of the olfactory bulb and the choroid plexus as well as in resting glial cells, including microglia and astrocytes.¹⁶⁶ As a result of cerebral inflammation triggered by brain injury, TSPO expression markedly increases in activated glial cells, especially microglia, and in blood-borne macrophages/monocytes infiltrating the lesions.¹⁶⁷ A variety of radiolabelled ligands have been developed and evaluated to monitor changes in TSPO expression in animal models of epilepsy and in humans (Figure 34).^{166, 168, 169}

Of particular interest is the radiotracer ¹¹C-flumazenil, which has been extensively used to evaluate central benzodiazepine receptors in human epilepsy studies. Complex mechanisms of epileptogenesis are characterised by metabolic and neurotransmitter/receptor disturbances, with functional impairment of neurotransmission likely to play a vital role. γ -Aminobutyric acid (GABA) is the principal inhibitory transmitter in the brain and plays an important role in the genesis of partial seizures. Many studies have shown that ¹¹C-flumazenil (a specific antagonist for central benzodiazepine receptors (cBZR))-PET can detect abnormalities (mostly decreased binding) in the epileptogenic zone of patients with both temporal lobe epilepsy and extratemporal epilepsy.¹⁵¹

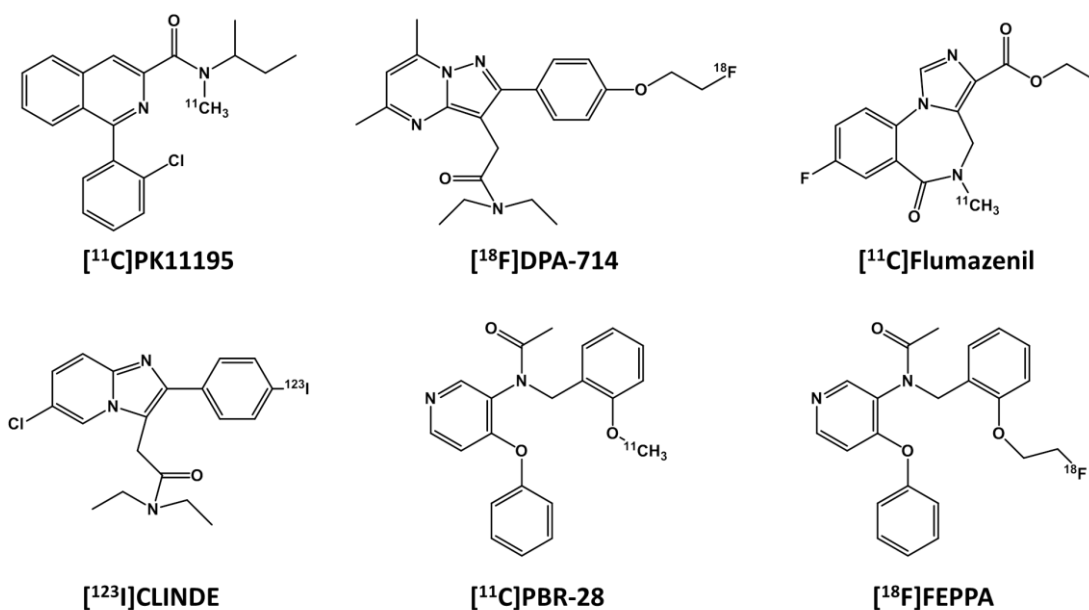


Figure 34. Structures of radiotracers used for imaging TSPO expression in epilepsy patients.¹⁶⁶

5.4 Study Outline

The purpose of this study was to determine if the radiolabelled CA, first discussed in chapter 4, could detect increased VCAM-1 expression in the lithium pilocarpine model of SE, by SPECT and MRI. The lithium pilocarpine model of SE was induced in male Sprague-Dawley rats. The radiolabelled CA (5 mg Fe/kg, 0.08 – 0.20 MBq/g) was administered via a cannula implanted in the external right jugular vein, 20 hours after the termination of seizures. SPECT/CT imaging commenced 20 min after administration of the CA, followed by imaging with MRI 45 min later. At the end of the acquisition, the animals were sacrificed and the brains were cryosectioned coronally (40 μm). The distribution of the CA was determined with phosphorimaging after the brain sections were exposed on the phosphor screens for 48 hours. The two control groups used were rats that received saline in place of pilocarpine (SALINE_{VCAM}) and rats that received [¹²⁵I]IgG-MPIO in place of [¹²⁵I]VCAM-MPIO (SE_{IgG}).

5.5 Results

The lithium-pilocarpine model of SE was used to further evaluate the properties of [125 I]VCAM-MPIO as a CA. All pilocarpine treated animals progressed to SE and displayed akinesia and facial automatisms. Tonic-clonic seizures and SE were induced 40-50 minutes after pilocarpine administration. The seizures were terminated 90 min after SE onset by administration of diazepam. None of the animals in the SALINE_{VCAM} group exhibited any signs of behavioural seizures.

With SPECT/CT, highly localised uptake of the CA was apparent in the cerebellum, brain stem and olfactory bulb for animals in the SE_{VCAM} group (n = 3, Figure 35a-c). With MRI, hypointensities were mainly observed near the hippocampus and ventricles, but also in the hypothalamic regions (Figure 35d). Both SPECT/CT and MRI displayed high uptake of the CA in the cortex. Phosphorimaging of coronal brain cryosections confirmed high uptake of [125 I]VCAM-MPIO in the cortex, hippocampus and hypothalamus (Figure 35e and f).

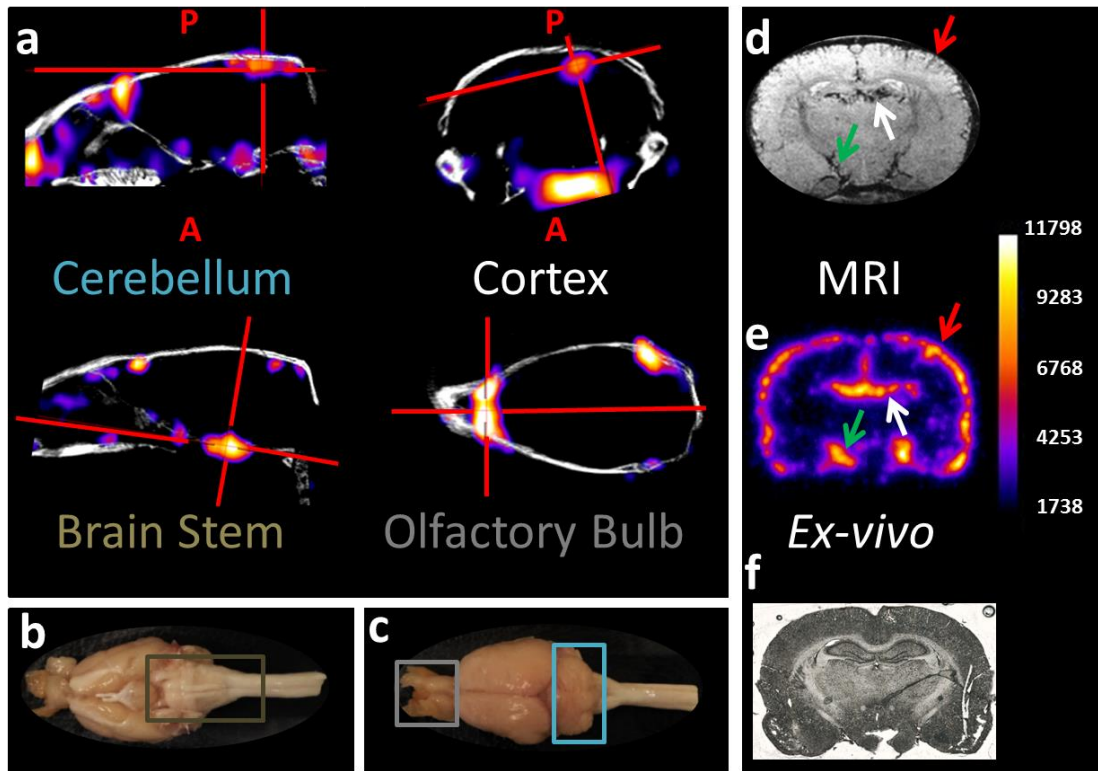


Figure 35. Evaluation of [^{125}I]VCAM-MPIO in the lithium -pilocarpine model of SE. (a) Representative SPECT/CT images from a rat administered [^{125}I]VCAM-MPIO (5 mg Fe/kg, 0.20 MB/g) approximately 20 hours after SE onset. Avid signals can be seen in the cerebellum, cortex, brain stem and olfactory bulb as viewed in the sagittal (cerebellum and brain stem), coronal (cortex) and transversal (olfactory bulb) slices. The, (b) brain stem, (c) cerebellum and olfactory bulb are highlighted on a perfused rat brain. Uptake of the CA was also observed with (d) MRI and (e) phosphorimaging near the hippocampus (white arrows), as well as at the cortex (red arrows) and hypothalamus (green arrows). (f) Optical image of the brain section shown in (e); P = Posterior A = anterior from the injection site.

No uptake of the CA was observed in brains from sham treated animals (SALINE_{VCAM}, n =3), and in control animals that received [^{125}I]IgG-MPIO (SE_{IgG}, n = 3) as observed with *in vivo* SPECT and MRI (Figure 36).

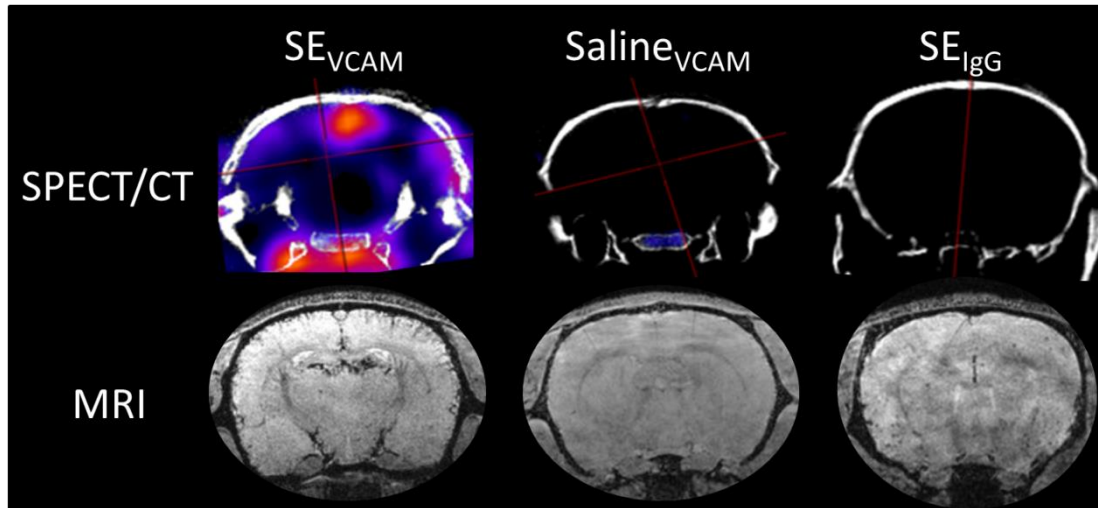


Figure 36. Bimodal *in vivo* imaging of seizure induced inflammation. The distribution of the CA (5 mg Fe/kg, 0.08 – 0.20 MBq/g) was assessed by SPECT/CT (top row) and MRI (bottom row) in the SE_{VCAM} group and the two control groups (SALINE_{VCAM}, SE_{IgG}).

Since the radioactivity content was too low to determine the distribution of the CA *in vivo*, the relevant brain sections were analysed by phosphorimaging (Figure 37). As seen in the TNF- α treated animals (chapter 4), [¹²⁵I]VCAM-MPIO distributed predominantly to larger blood vessels in the SE_{VCAM} group. In the slices proximal to the lambda, uptake of the CA was dominant at the choroid plexus and within the vasculature, in particular the middle cerebral artery. Minimal signals were observed in the brain slices from the two control groups.

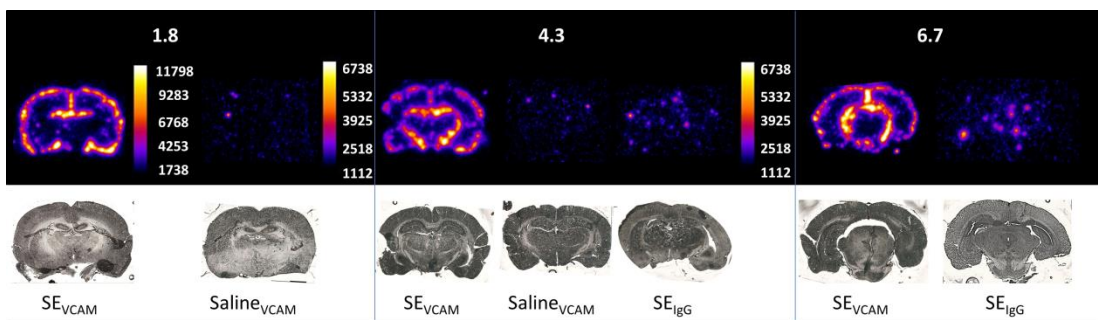


Figure 37. The distribution of the CA assessed by phosphorimaging. Phosphorimages of coronal brain sections (40 μ m) from the SE_{VCAM} group ([¹²⁵I]VCAM-MPIO: 5 mg Fe/kg, 0.25 MBq/g), Saline_{VCAM} ([¹²⁵I]VCAM-MPIO: 5 mg Fe/kg, 0.08 MBq/g) and SE_{IgG} ([¹²⁵I]IgG-MPIO: 5 mg Fe/kg, 0.08 MBq/g). The thresholding of the phosphorimages have been adjusted to account for the amount of radioactivity administered. The distance of the brain sections shown from the bregma are approximately indicated in mm.

Dynamic imaging with SPECT using 5 min frames from 20 to 45 min post-injection of the CA revealed that the levels of radioactivity remained constant (Figure 38). Considerably higher counts were recorded in the SE_{VCAM} group compared to controls.

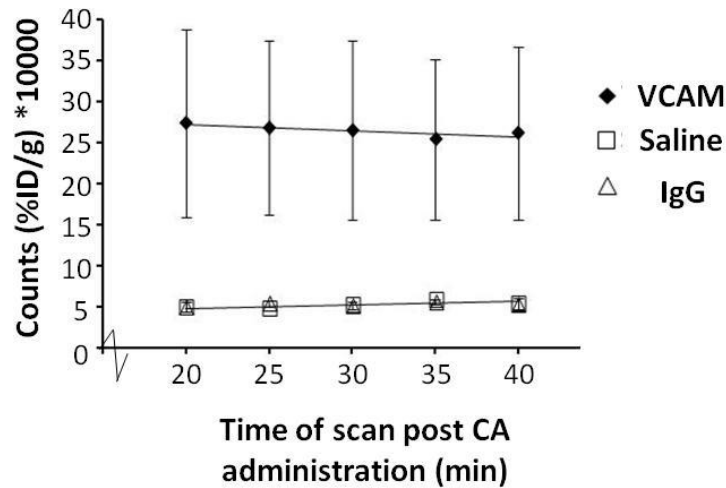


Figure 38. Quantification of the dynamic SPECT images captured from 20 to 45 min following administration of the CA (5 mg Fe/kg, 0.08 – 0.25 MBq/g) in seizure induced rats. Averages from the SE_{VCAM} (n = 3, ± SD), SALINE_{vcam} (n = 3, ± SD), and SE_{IgG} (n = 3, ± SD) groups are presented.

5.6 Discussion

This study has characterised [¹²⁵I]VCAM-MPIO in a model that has relevance to human disease: the lithium-pilocarpine model of SE. A strong inflammatory component¹³⁸ and several anti-inflammatory therapies have been identified and evaluated in this model.^{170, 171} In particular the distribution of the non-radiolabelled contrast agent, VCAM-MPIO, has previously been assessed in the lithium-pilocarpine model, with significant hypointensities observed in the choroid plexus, hippocampus, cerebral cortex and to a lesser extent, the thalamus, 20 hours after SE.¹¹⁷ These findings have been corroborated in the current study, which has additionally demonstrated for the first time that complimentary SPECT imaging of seizure induced inflammation is feasible.

Avid SPECT signals in the SE_{VCAM} group were localised to the cerebellum, cortex, brain stem and olfactory bulb which can be linked to the behavioural changes observed in rats administered pilocarpine. These included olfactory automatisms, eye blinking and salivation. In contrast, *in vivo* SPECT imaging suggests there was minimal uptake of the CA in the brains of the two control groups (SE_{IgG} and SALINE_{VCAM}). In part, this could be due to the low radioactivity content administered (0.08 MBq/g). Such a low dose was administered as in the TNF- α study, (chapter 4), *in vivo* SPECT and MRI failed to demonstrate any considerable uptake of the CA (0.20 – 0.90 MBq/g) in the control groups. As a result of this, as well as to save costs and minimise exposure to ionising radiation, this study focused on evaluating the distribution of the CA in the control groups by *ex vivo* phosphorimaging. Therefore, the doses of radiolabelled CA administered (5 mg Fe/kg, 0.08 MBq/g) reflect this and the phosphorimages have been thresholded accordingly.

Qualitative evaluation of the phosphorimages show that, similar to the TNF- α group, the CA was predominantly distributed to larger blood vessels in the SE_{VCAM} group, with uptake foremost at the choroid plexus and middle cerebral artery. Whilst phosphorimaging showed localised uptake of the CA at the TNF- α injection site, and thus suggested that local inflammation was induced in the sham treatment (Figure 28g), minimal signals were observed in the SALINE_{VCAM} group across the whole brain. Moreover, as demonstrated in the TNF- α model, the lack of signals detected in the SE_{IgG} group suggests there was little non-specific binding.

Quantitative assessment of the SPECT images obtained 20 – 45 min post CA administration revealed that the radioactivity content in the brain did not change over this period of time. Considerably higher counts were recorded in the SE_{VCAM} group compared to the controls, indicating substantial uptake of [¹²⁵I]VCAM-MPIO and hence increased VCAM-1 expression in SE induced rats.

In vivo imaging was approximately conducted 20 hours after the termination of seizures. Therefore, this study has investigated neuronal changes in the acute phase of the model. The results presented warrant further investigations at the chronic phase in order to increase our understanding of the epileptogenesis process. Additionally, it will be vital to determine how much of the CA distribution is blood

flow dominated, especially considering the fact that marked hypermetabolism¹⁷² and changes in cerebral blood flow¹⁷³ have been reported during and after SE.

5.7 Conclusion

This study has demonstrated that complimentary SPECT imaging of seizure induced inflammation is feasible and showcases the potential of multimodal validation. Nevertheless, due to a lack of *ex-vivo* immunohistochemical analysis and the number of animals in each group (n = 3), it was difficult to ascertain how closely the SPECT images agree with those of the MRI and how faithfully the signals represent VCAM-1 expression or alterations in blood flow. Promisingly, based on qualitative evaluation, both MRI and SPECT highlighted an increase of CA uptake within the cortex in the disease model compared to the controls.

The fact that a single CA can be used to study the epileptogenesis process by MRI, SPECT and phosphorimaging presents exciting opportunities to gain a deeper understanding of the role of inflammation in epilepsy. To the best of our knowledge, this is the first study to ascertain a biomarker for epileptogenesis using multiple imaging modalities within the same animal. Combining the high resolution offered by MRI with the high sensitivity of SPECT or PET imaging, could enable earlier diagnosis and identification of biomarkers for epileptogenesis, which is currently lacking. The results presented in this proof-of-principle study indicate that radiolabelled VCAM-MPIO to target VCAM-1 expression could be a viable option to achieve this.

Chapter 6 Synthesis and Evaluation of [¹²⁵I]CNS-1261 for Targeting Activated NMDA Receptors

6.1 Aim and Hypothesis

The study outlined in this chapter investigates the interplay between neuroinflammation, hyperexcitability and dysfunction of fast neurotransmission, each which have been investigated in the studies discussed in the previous chapters. The motivation is to assess if the functional activity of NMDA receptors becomes altered post SE.

Since radioiodinated CNS-1261 has displayed favourable kinetic properties in clinical studies, it was assumed this tracer would be a good candidate to determine if activated NMDA receptor expression becomes altered in adult male rats, 7 days after SE. This would allow us to further understand the mechanisms involved in epilepsy.

6.2 NMDA Receptors

Excitotoxicity refers to cell death resulting from the toxic actions of excitatory amino acids.¹⁷⁴ The amino acid glutamate is the principal excitatory neurotransmitter and its two main receptors are ionotropic or metabotropic. The ionotropic receptor can be further subdivided into three subtypes: NMDA (N-methyl-D-aspartate), AMPA (α -amino-3-hydroxy-5-methyl-4-isoxazolepropionate), and kainate. The NMDA receptors (NMDARs) are tetrameric ion channels with multiple ligand recognition sites, both inside and outside the channel (Figure 39). For activation, NMDARs require the binding of both glutamate to the NR2 subunit and a co-agonist such as glycine to the NR1 subunit. Simultaneous binding of glutamate and glycine results in channel opening thus permitting the influx of calcium and to a lesser extent, sodium ions into neurons.¹⁷⁵ A voltage dependant Mg^{2+} block is present on NMDARs which closes the channels when a certain membrane potential is exceeded (as shown in red on Figure 39).

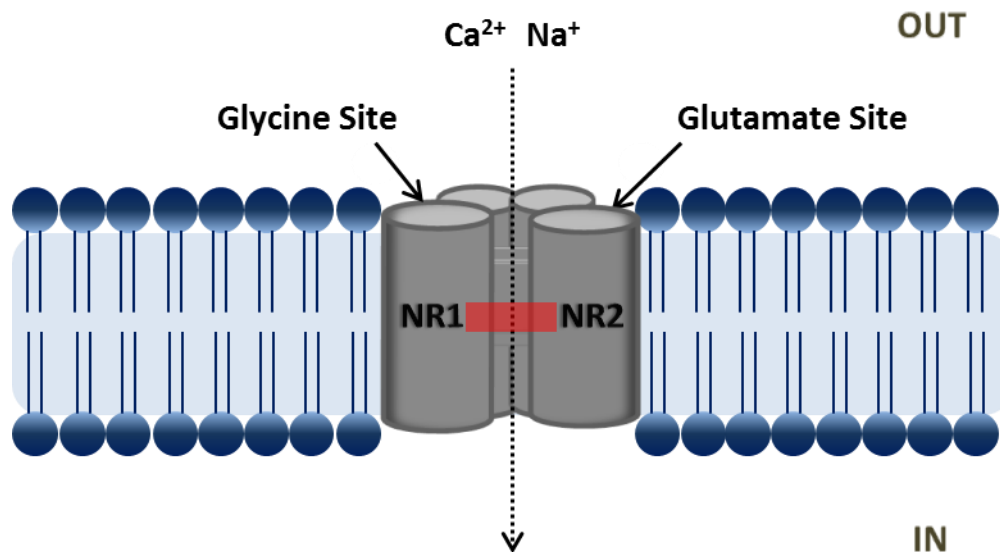


Figure 39. Representation of NMDA receptors. MK-801, Ketamine and Memantine act as non-competitive antagonists whose binding sites are within the ion channel pore, whilst the binding sites for glutamate and glycine are found on the extracellular portions of the NR2 and NR1 subunits.

Normal extracellular glutamate concentration is about 0.6 $\mu\text{mol/L}$. Substantial neuronal excitotoxic injury occurs with glutamate concentrations of 2 to 5 $\mu\text{mol/L}$.¹⁷⁵ At such high concentrations, NMDARs can become over stimulated resulting in neuronal calcium overload. Accumulation of intracellular calcium ions leads to activation of enzymes, including phospholipases that degrade proteins, membranes and nucleic acids.¹⁷⁴ Pharmacological blockade of NMDARs by compounds that interact at a site within the open ion channel may therefore have therapeutic effects. Examples of such agents include MK-801 (dizocilpine),¹⁷⁶ and memantine,¹⁷⁷ which has shown to have neuroprotective effects in preclinical studies.¹⁷⁸

The NMDA receptor complex has been suggested as a therapeutic target in epilepsy.¹⁷⁹ A variety of techniques such as subunit gene expression, immunoblotting and binding affinities, have found alterations in NMDA receptor expression in patients with epilepsy. Studies have found elevated mRNA levels for the NR2 subunits in patients with hippocampal sclerosis, which is one of the most frequently encountered pathologies in temporal lobe epilepsy.¹⁸⁰ Antagonists acting at NMDARs have also had potent anticonvulsant actions.¹⁸¹ In animal models of chronic epilepsy, it has been shown that 28 days after the last evoked seizure,

kindling, (focal electrical stimulation of the brain), induced a 2.8 fold increase in the number of binding sites for the competitive NMDAR agonist ^3H -CPP. This increase was confined to the CA3 region within the hippocampus.¹⁸²

Furthermore, increases in glutamate levels have been observed in rodent models of epilepsy. *In vivo* microdialysis on rats induced with seizures using the maximal electroshock (MES) protocol,¹⁸³ has shown that in the ventral hippocampus, there was a significant increase ($29 \pm 2\%$) in extracellular glutamate and this had peaked 50 min post seizures ($54 \pm 6\%$).¹⁸⁴ Repeated seizures significantly increased glutamate release compared with a single MES, ($84 \pm 8\%$ compared to $29 \pm 2\%$). Concentrations of glutamate, aspartate and glycine have also been shown to be increased in epileptogenic cerebral cortex.¹⁸⁵

Reports have shown that ictogenesis may be exacerbated by inflammatory cytokines such as interleukin-1 beta (IL-1 β) and TNF- α , possibly by increasing activated NMDA receptor states: using primary cultures of rat hippocampal neurons, IL-1 β (0.01-0.1 ng/ml) enhanced NMDA-induced Ca^{2+} concentration by up to 45% in a dose dependant manner.¹⁸⁶ Additional inflammatory mediators, such as cytokines (IL-1 β , IL-6, TNF- α) and prostaglandin E2 whose specific functions remain unresolved, are thought to play an active role in seizure generation and exacerbation.¹³⁸ The mechanism of action is thought to involve increases in ion channel conductance, enhanced glutamate release and impairment of potassium and glutamate buffering. In particular, IL-1 β has been shown to inhibit GABA receptor function in cultured hippocampal neurones¹⁸⁷ whilst enhancing calcium influx and NMDA receptor mediated transmission,¹⁸⁶ culminating in hyperexcitation.

In this study, the expression of activated NMDARs was investigated in the lithium pilocarpine model of SE. By investigating the functional activity of these receptors in this model, the aim was to establish a potential new biomarker for epileptogenesis. In order to target and hence monitor the expression of activated NMDARs, the diarylguanidine derivative, CNS-1261 was radiolabelled and administered into rats 1 week post SE induced seizures. The distribution of radioactivity, which is likely to reflect the expression pattern of activated NMDARs, in the relevant brain regions were analysed by phosphorimaging. In the next section, evidence is presented to

justify why this compound was selected for tracer development in order to target activated NMDARs.

6.3 [¹²⁵I]CNS-1261

The lack of suitable SPECT and PET ligands has limited direct evaluation of NMDARs *in vivo*. To target and image neuroreceptors, appropriate radiotracers must exhibit high specificity and affinity, and have apt lipophilicity. Studies have indicated that *N*-(1-Naphthyl)-*N'*-(3-[¹²⁵I]-iodophenyl)-*N'*-methylguanidine ([¹²⁵I]CNS-1261, [¹²⁵I]**19**), meets this criterion and has thus been proposed as a SPECT tracer for imaging activated NMDARs.¹⁸⁸⁻¹⁹⁰

In radioligand binding assays, CNS126-1 exhibited high selectivity for NMDARs.¹⁸⁸ At a concentration of 10 nM, CNS-1261 was selective for NMDARs and no significant binding was observed to receptors in any of the 41 other assays investigated. At a higher concentration (1 μM), CNS126-1 showed complete occupancy of the [³H]MK-801 binding site, whilst displaying marginal binding at the Na⁺ channel (38%), α-1 adrenoceptor (33%) and GABA transporter (21%).

Furthermore, in ischemic rat brains, [¹²⁵I]CNS-1261 uptake was markedly increased in the neocortex and striatum, with a twofold higher uptake in the ipsilateral caudate compared to the equivalent area of the contralateral hemisphere.¹⁸⁹ These results are in good agreement with the increased uptake observed of [¹²⁵I]MK-801 in periischemic areas. Equally, autoradiography experiments showed that, in normal rat brain, the uptake of [¹²⁵I]CNS-1261 in NMDA receptor-rich regions relative to the cerebellum was superior than that of [¹²⁵I]MK-801.¹⁸⁸

In preclinical studies, CNS-1261 was found to have a high affinity to the intrachannel site on NMDARs with a K_i value of 4.21 ± 0.4 nM against [³H]MK-801.¹⁸⁸ Furthermore, the high affinity and selectivity of [¹²⁵I]CNS-1261 to the MK-801/ketamine site on activated NMDARs has also been demonstrated in clinical studies.¹⁹⁰

In vivo metabolic studies using rat plasma and brain samples have shown that the plasma half-life of [¹²⁵I]CNS-1261 is 2.17 ± 0.44 min and deiodination occurred

rapidly.¹⁸⁸ However, extracts of brain homogenates showed that at 120 min post injection, >95% of radioactivity in the brain was due to intact [¹²⁵I]CNS126-1.

The high selectivity and affinity of [¹²⁵I]CNS126-1 to activated NMDARs, and its high metabolic brain stability, suggests that the distribution and density of radiolabelled CNS-1261 should theoretically reflect dynamic changes in NMDAR expression.

Above all, *in vivo* evaluations of [¹²³I]CNS-1261 in humans have proven to be successful and its pharmacokinetic properties render it to be a suitable tracer for *in vivo* imaging in the brain.¹⁹⁰

6.4 Study Outline

To determine if activated NMDA receptors play a role in seizure generation, changes in their expression have been monitored in animals induced with SE using the lithium pilocarpine model. CNS-1261 was radiolabelled with iodine-125 to reveal whether this radiotracer could highlight any changes in receptor expression.

6.4.1 Animal Model

The lithium pilocarpine model of SE (n = 5) was induced in Male Sprague Dawley rats (170-200g). The animals in the control group received saline in place of pilocarpine (n = 5).

One week after the termination of seizures, [¹²⁵I]CNS-1261 (25-30 MBq in saline (10% ethanol)) was administered by V. Taylor. The animals were anaesthetised two hours post tracer injection with 4% isoflurane mixed with medical air. After culling the animals by cervical dislocation, the brains were removed and fixed overnight in paraformaldehyde (4%), cryoprotected overnight in sucrose solution (45%) and sectioned coronally at 16 µM.

6.4.2 Phosphorimaging

Brain slices were mounted on polylysine coated glass slides. These were placed on a phosphor screen along with a set of [¹²⁵I]NaI standards (0.5 - 0.0001 MBq). One week after exposure, the screen was scanned, (25 µm resolution, acquisition time = 2 h 30 min).

6.4.3 Phosphorimaging Quantification

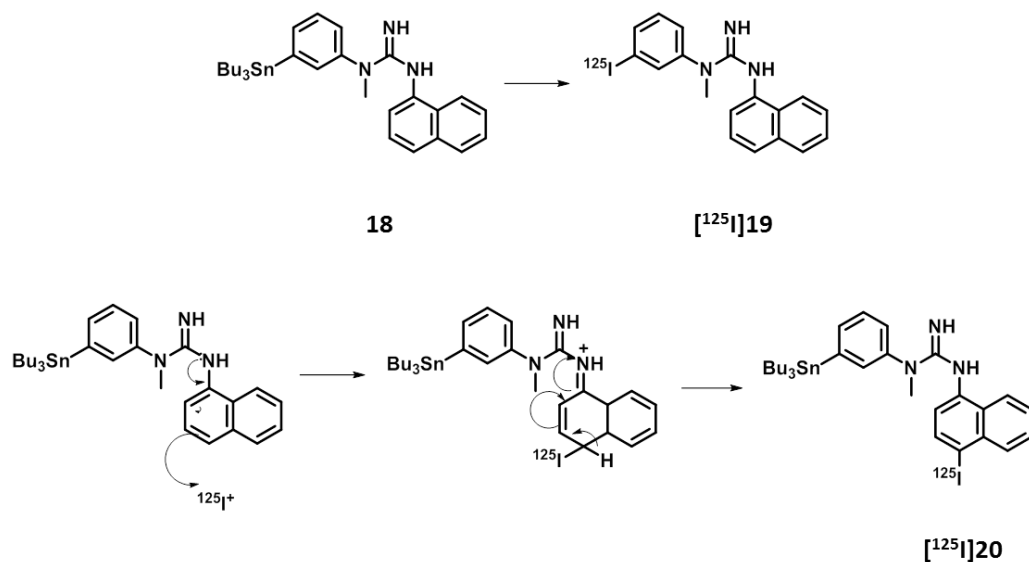
Image Quant TL 7.0 software was used to quantify the signals observed in the brain slices. Using the HE stained slices to identify anatomical regions, ROIs were set on the hippocampus, thalamus, hypothalamus, amygdala and piriform cortex (Figure 40). Counts per pixel within these ROIs were normalised to the amount of radioactivity administered into each animal. The amount of radioactivity in each region is expressed as a ratio to the amount of radioactivity recorded in the cerebellum. Group means were compared using an unpaired t-test. Statistical significance was assigned at $P < 0.05$.



Figure 40. Representation of ROIs selected for quantification of phosphorimaging signals. Red = hippocampus; Green = thalamus; Brown = hypothalamus; Yellow; amygdala; Blue = piriform cortex.

6.5 Results

6.5.1 Radiolabelling



Scheme 8. Radiolabelling of the tributyl tin precursor (**18**) to obtain [¹²⁵I]CNS-1261 ([¹²⁵I]**19**) and a possible side product ([¹²⁵I]**20**) which may have been formed.

The results from the radiolabelling experiments are summarised in Table 5 and the representative HPLC chromatograms are displayed in Figure 41. The retention time of **18** was 25 min and for [¹²⁵I]**19** was 15 min. The highest analytical (62%) and isolated (42%) radiochemical yields for [¹²⁵I]CNS-1261 was with method 2, 30 min reaction time, (SA = 21.0 GBq/μg). This was the method therefore used to obtain [¹²⁵I]CNS-1261 for the *ex vivo* evaluations. At higher HCl concentrations (0.4 M, method 1) there was a 40% reduction in yields when reaction times were increased, whilst at the lower concentration (0.1 M), the yield was 72%, (method 2, 10 to 30 min reaction time). Longer reaction times (method 2, 60 min) did not improve the yields. Overall, the combination of acetic acid and peracetic acid gave lower yields compared to HCl and H₂O₂. The exception was method 4, which for the 30 min reaction time, gave a 28% higher yield compared to method 1. Diluting the glacial acetic acid to 5% led to an 8 fold increase in the yield at 30 min reaction time (methods 3 and 4).

Method	Acid	Oxidant	Reaction Time (min)	Analytical RCY (%)	Fig. 41 Chromatogram
1	HCl 0.4 M	Hydrogen Peroxide	10	47	a
			30	28	b
2	HCl 0.1 M	Hydrogen Peroxide	10	36	c
			30	62	e, f
			60	57	d
3	Acetic Acid >95%	Peracetic Acid	10	4	g
			30	5	h
4	Acetic Acid 5%	Peracetic Acid	30	39	i

Table 5. Analytical radiochemical yields (RCY) for the radiolabelling of CNS-1261. All reactions were carried out at room temperature.

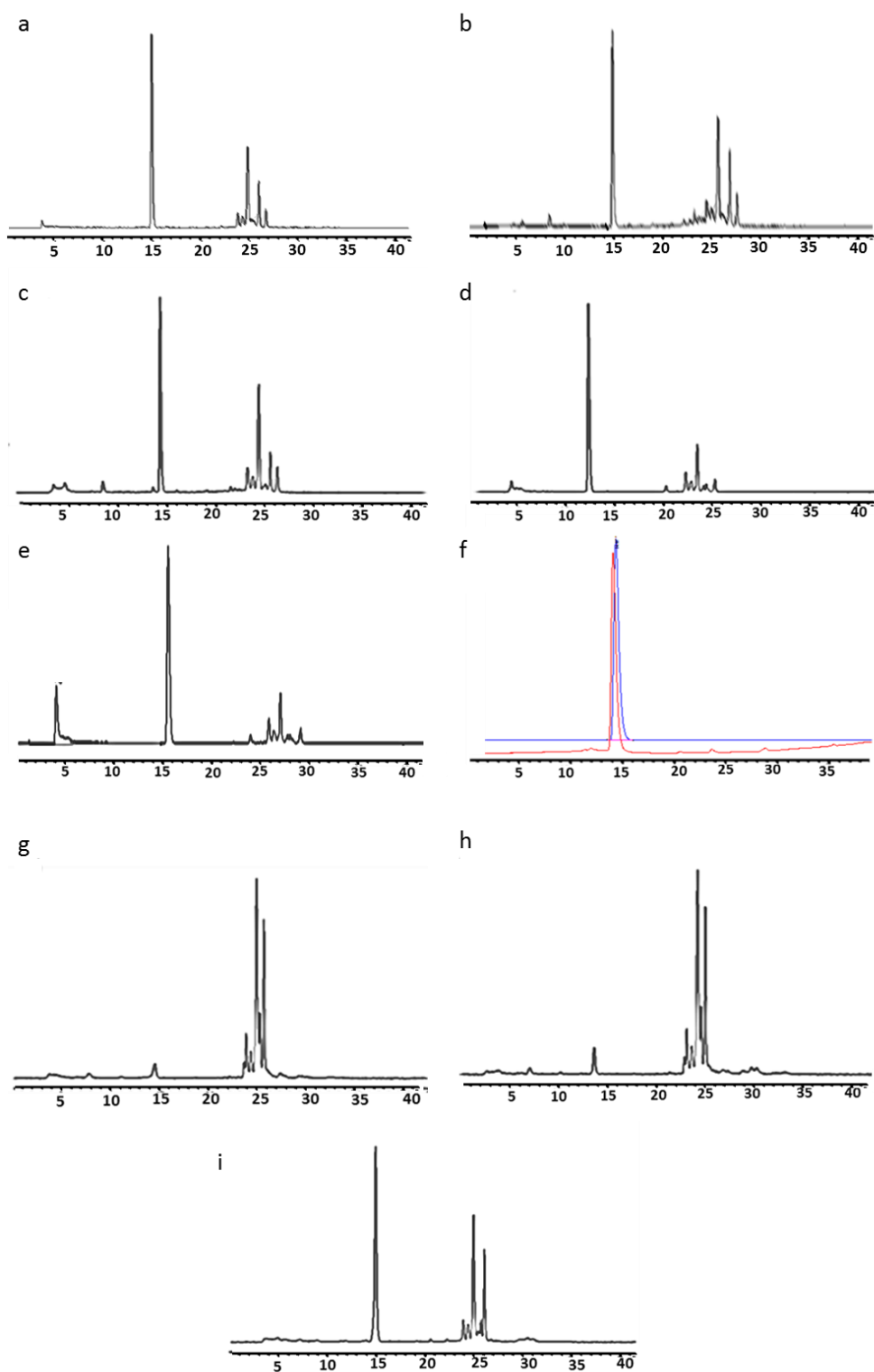


Figure 41. Analytical Radio-HPLC chromatograms for the radiolabelling of CNS-1261. Retention time of $[^{125}\text{I}]\text{CNS-1261}$ = 15 min. The radiolabelling reactions represented by each chromatogram are as follows: a: method 1, 10 min reaction time; b: method 1, 30 min reaction time; c: method 2, 10 min reaction time; d: method 2, 60 min reaction time; e: method 2, 30 min reaction time; f: method 2, 30 min reaction time showing both radio (blue) and UV (red) signals for the isolated, purified product co-injected with **19**; g: method 3, 10 min reaction time; h: method 3, 30 min reaction time; i: method 4, 30 min reaction time. Reaction conditions for each method are given in table 5.

6.5.2 Animal Model

All of the rats administered pilocarpine reached stage 5 on the Racine scale and seizure severity alternated between stages 3 and 5 over 90 minutes. None of the animals which received saline in place of pilocarpine exhibited any behavioural change. Two doses of diazepam were sufficient to terminate SE and no overt signs of sustained seizures were observed within the following 24 hours. Over the course of a week, all rats began to feed and drink themselves which resulted in a steady weight increase. However, one of the animals was terminated 3 days post SE as his weight had decreased by more than 20%.

6.5.3 Phosphorimaging

The brains for phosphorimaging were removed 2 hours after tracer injection. In pilocarpine treated rats, the amount of radioactivity measured in discrete brain regions was higher compared to the saline controls (Figure 42). However, this increase was not statistically significant based on an unpaired t-test ($P < 0.05$). Furthermore, there were no significant differences in tracer uptake between the brain regions investigated. There was a large spread in counts recorded between animals in each group ($n = 5$), particularly for the piriform cortex and amygdala.

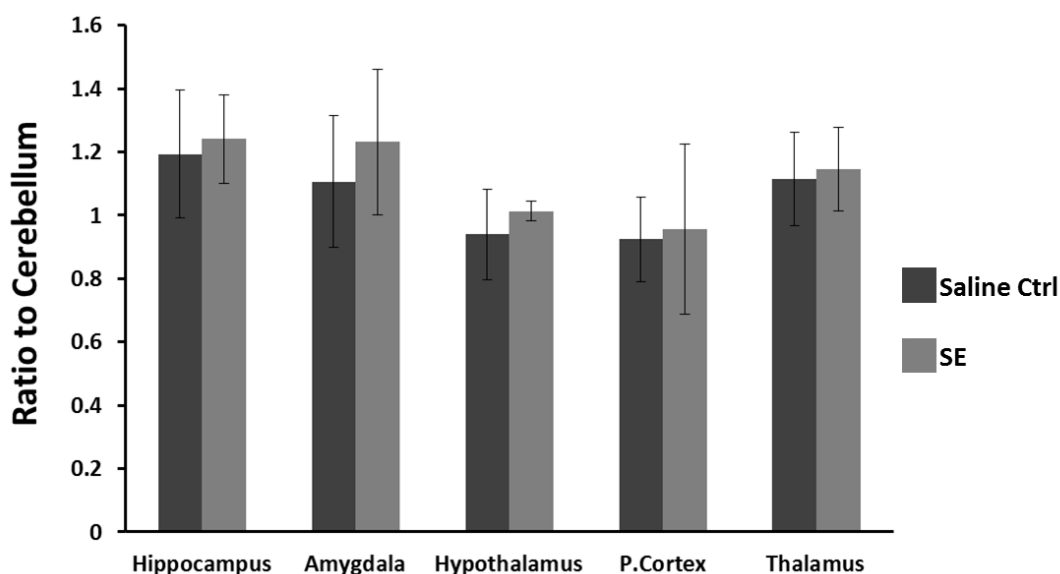


Figure 42. Quantification of the phosphorimaging signals. Quantification was performed using the ROIs shown in Figure 40. For both the SE and control group, $n=5$ with the animals sacrificed two hours after the administration of [125 I]CNS-1261. For all animals, the counts in each brain region are expressed as a ratio to the counts recorded in the cerebellum. Error bars are mean \pm standard error of the mean.

6.6 Discussion

6.6.1 Radiochemistry

In general, electrophilic iodo-destannylation provides an excellent method for the introduction of iodine into organic molecules.^{93, 188} The oxidant, acid and reaction time which gave the highest isolated radiochemical yield (42%) and purity (>98%) of [125 I]CNS-1261, was H_2O_2 , HCl (0.1 M) and 30 minutes (method 2, Figure 41f, specific activity = 21.0 GBq/ μg).

The use of peracetic acid and acetic acid gave considerably lower yields (5%) and purity (method 3, Figure 41g). The major radiolabelled products under these conditions exhibited higher lipophilicity compared to the desired product (Figure 41g, h). Due to the electron donating capability of nitrogen atoms, one of these impurities is likely to be compound [125 I]**20** highlighted in scheme 7. This inductive effect would be less pronounced with strong acids as under such conditions (methods 1 and 2), nitrogen atoms are more likely to become protonated. HCl has a lower pH compared to acetic acid and it is therefore a stronger acid. By definition, this means

that HCl will dissociate completely to form H⁺ ions whereas acetic acid weakly ionizes, so there will be fewer H⁺ ions.

6.6.2 Phosphorimaging

Radioactivity levels in discrete brain regions have been presented as a ratio to the radioactive levels in the cerebellum since relatively low NMDA receptor binding sites have been reported in this structure.^{191, 192} Biodistribution studies have revealed that the hippocampus/cerebellum ratio peaks 2 hours post [¹²³I]CNS-1261 injection in healthy rats.¹⁹³ As a result, this was the time post tracer administration when brains were obtained for phosphorimaging. Nevertheless, the expression pattern of activated NMDARs and so tracer distribution over time in SE models may differ considerably, especially since marked changes in blood flow have been reported in this model at different stages post SE.^{194, 195} This may explain why no significant differences were observed between the control and SE groups. Therefore, future investigations should ascertain time points where NMDA receptor activation is maximised in the lithium-pilocarpine models.

[¹²⁵I]CNS-1261 was administered seven days after the termination of SE and so investigations were conducted in the chronic stage of the disease as studies have reported increases in glutamate levels only at this point.¹⁹⁶

In this study, pilocarpine hydrochloride (30 mg/kg) was administered to induce SE. One notable study found no significant changes in the levels of glutamate following the administration of a higher pilocarpine dose (400 mg/kg) or after the onset of seizures.¹⁹⁷ Only when pilocarpine (10 mM) was delivered focally into the hippocampus did extracellular glutamate concentrations increase. This suggests that a greater local concentration of pilocarpine is required to increase glutamate levels in this model. Furthermore, whilst increases in glutamate concentration in epileptogenic cerebral cortex have been reported, increases in the activity of glutamate dehydrogenase, which is involved in glutamate metabolism, have also been observed.¹⁸⁵ Therefore, insufficient concentrations of pilocarpine, increases in enzyme metabolising activity, and the action of glutamate re-uptake systems indicates there will be reduced levels of agonists for NMDAR activation. This may

explain the lack of activated NMDARs observed in the lithium pilocarpine model.¹⁹⁸ There have also been reports showing increases in glutamate levels preceding seizure onset.¹⁹⁷ However, in this study, [¹²⁵I]CNS-1261 was administered seven days post SE. Therefore, injection of the tracer immediately after pilocarpine administration, and subsequent evaluation of its distribution prior to seizure onset may produce more fruitful results.

High variability was observed in the quantified signals between animals in the same group. One possible explanation for this is that ROIs could not be manually drawn around discrete brain regions, and instead predefined shapes were used as represented in Figure 40. Also, published observations for the lithium pilocarpine model have been inconsistent due to the highly variable nature of the model, especially in terms of the apparent site of origin for electrographic seizures.¹⁴⁵

6.7 Conclusion

Although excessive activation of NMDARs and the accompanying hyperexcitability has been implicated in the pathogenesis of (epileptic) seizures,^{181, 197} this study found no differences in receptor activity between the lithium pilocarpine model and saline controls. To the best of our knowledge, this is only the second study to evaluate the targeting ability of [¹²⁵I]CNS-1261 in a disease model, and the first to do so in the lithium pilocarpine model of SE. Whilst this study was unsuccessful in reflecting the distribution of functionally active NMDARs in distinct brain regions, the potential of this tracer for further investigations remain promising. This is especially true as its *in vivo* evaluations in humans have proven to be successful and its pharmacokinetic properties render it to be a suitable tracer for *in vivo* imaging in the brain.

Chapter 7 Summary and Further Work

Nuclear imaging (PET, SPECT and phosphorimaging) has been instrumental in evaluating the efficacy of therapies and delineating key pathological processes in neurological diseases. The aim of the work described in this thesis entitled: ‘Development of Radiotracers for Neuroimaging’, was to gain further insights into the key pathological processes involved in hyperexcitation and epileptogenesis. Whilst it was beyond the scope to deconstruct the mathematical reconstruction algorithms and the core physics underlying image generation, the principles of radioactivity detection and factors affecting image quality have been discussed. In the latter part of chapter 1, the key properties of a suitable brain radiotracer, and the radiotracer discovery and development pipeline were analysed.

In chapter 2, the experimental methods used to analyse and quantify detected signals were discussed. These methods were based on manufacturers’ recommended calibrations, and the standardisation methods routinely employed both in the pre-clinical and clinical practice.

Nuclear imaging, namely SPECT and phosphorimaging have been used to evaluate the capabilities of radiotracers to target and monitor the expression of neuronal VGSCs (chapter 3), VCAM-1 (chapters 4 and 5) and activated NMDA receptors (chapter 6).

There has been limited success in imaging neuronal VGSC expression despite their role in many life limiting conditions. From the identification of two lead compounds, radiotracers for VGSCs in the brain have been developed and analysed *in vitro*, *in vivo* and *ex vivo*. The WIN17317-3 compound class proved to be un-suitable for *in vivo* imaging and thus should not be pursued for radiotracer development, primarily due to its poor metabolic stability. In contrast, the BNZA family exhibited encouraging results, with moderate brain uptake and excellent metabolic stability.

In the pursuit of developing a novel, neuronal VGSC radiotracer, modifications to the BNZA analogue were attempted with the aim to produce a PET tracer. However, synthesising the desired pre-cursor for radiolabelling was unsuccessful. The reason for this is not known but may involve the formation of a dimer. In order to

circumvent this, future attempts should initially focus on adding **9** to either propane-1,3-diyl bis(4-methylbenzenesulfonate) or propane-1,3-diyl dimethanesulfonate, therefore ensuring that **9** is always the limiting reagent.

In spite of the results obtained thus far, the BNZA compound class cannot yet be ruled out for *in vivo* imaging, largely due to its highly localised uptake observed at regions corresponding to brown adipose fat tissue. Further work should focus on this potential as well as exploring alternative methods to lower the lipophilicity and thus increase brain uptake of BNZA analogues. Overall, to the best of our knowledge, we are the first to develop radioiodinated tracers for neuronal VGSCs and have revealed that a derivative of BNZA exhibits excellent metabolic stability. Therefore, this compound class could be well suited for radiotracer development. On the other hand, the WIN17317-3 structural class should be avoided for tracer development.

The need to identify early biomarkers for neuroinflammation and epileptogenesis has been stressed in the introduction for chapters 4 and 5 respectively. The value of using SPECT for imaging VCAM-1 expression with targeted MPIOs as well as the importance of multimodal imaging and cross validation has been highlighted. Radiolabelling VCAM-1 targeting antibodies conjugated to micron sized particles of iron oxide enabled the kinetics and for the first time, the biodistribution properties of this contrast agent to be determined. Moreover, in both the inflammatory model and in the lithium pilocarpine model of status epilepticus, it has been shown that imaging of inflammation with MRI and SPECT is feasible. To the best of our knowledge, this is the first study whereby dual imaging of VCAM-1 in the brain has been achieved. This novel approach to image neuroinflammation should inspire future studies to adopt a multi-modal imaging methodology, allowing the attributes of various imaging techniques to be combined.

The use of VCAM-1 targeting antibodies, conjugated to MPIOs for imaging studies has been reported previously in the literature.¹¹⁵⁻¹¹⁸ The work presented in this thesis took the extra step of radiolabelling the antibodies to facilitate multimodal imaging. Nevertheless, a limitation in the work presented, and in the studies which have assessed the non-radiolabelled CA, is the lack of CA characterisation. The degree to which the CA polymerises, (illustrated in Figure 43) can have profound effects on its

targeting ability, clearance rate and hence toxicity. Future studies should determine the size and make-up of this CA before administration into subjects.

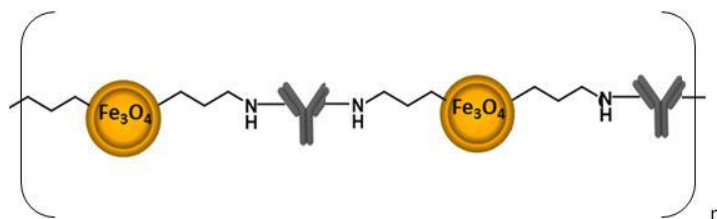


Figure 43. Polymerisation of VCAM-MPIO.

Whilst it would be of interest to determine how the targeting ability of radiolabelled antibodies compared to radiolabelled antibodies conjugated to MPIOs, the main focus of this work has been to develop a dual, MRI/SPECT imaging agent for VCAM-1 expression.

In chapters 4 and 5, despite the good agreement in CA distribution between SPECT and MRI, there were notable differences that needed addressing. Primarily, SPECT signals could be detected using a low dose of iron oxide and with relatively low activity levels of a weak gamma emitting radionuclide. This showcases the superior sensitivity of the technique and warrants further investigations. Such investigations should initially focus on reproducing the results presented in chapter 5 with a larger cohort to determine the significance of CA uptake in the disease animals compared to controls. This would justify using a more expensive, higher energy gamma emitting radioisotope in future experiments. Moreover, radioisotopes, such as I-123 will allow imaging of deeper brain tissues and so would determine how faithfully SPECT detects the neuronal damages known to occur after status epilepticus.

The results presented in chapters 4 and 5 have shown that SPECT and MRI are complimentary methods for detecting inflammation. A future study using this CA could ascertain if SPECT is more powerful in identifying earlier diagnostic markers for epileptogenesis. This is because [¹²⁵I]VCAM-MPIO is a versatile CA which enables SPECT and MRI to be conducted in the same animal, within a suitable time frame for imaging. For a fair comparison, the imaging protocol should feature

instances whereby animals initially undergo MRI post CA administration followed by SPECT or PET. Whilst this may be a challenge for shorter – lived radionuclides, it would nevertheless be feasible for commonly used radioisotopes of iodine (e.g. I-123, half-life = 13 hours) for SPECT or longer-lived radionuclides for PET (e.g. zirconium-89, half-life = 3.3 days).

The commercial MPIOs that have been used are non-biodegradable due to their polyurethane coat, and are thus not suitable for human applications. For clinical translation, it should be possible to synthesize biodegradable MPIOs with suitable modification of the surface coat, and this is currently being explored.¹⁹⁹⁻²⁰¹

Imaging of NMDAR expression in the brain by SPECT or PET could provide useful information on the role of these receptors in epileptogenesis as discussed in the introduction of chapter 6. The study detailed in chapter 6 was designed to image the distribution of [¹²⁵I]CNS-1261, and thus assess changes in NMDAR expression between healthy rats and in rats at the chronic period of epileptogenesis, (7 days after a 90 minutes status epilepticus seizure). Unfortunately, this goal was not accomplished. Indeed, a limitation was the fact that ROIs for quantification were not selected around the entire discrete locations, due to the restrictions imposed by the software analysis programme (Image Quant TL 7.0) used. Nevertheless, based on qualitative comparisons, there were no changes in radiotracer uptake between the disease model and the control group.

Moving forward, in this study a single time point was selected for investigation (7 days post SE). Changes in NMDAR expression may become significant at a different time point. With a radiotracer exhibiting appropriate kinetics and half-life, monitoring NMDAR expression over a period of time may identify the stage at which changes in receptor expression become optimal. Contextually, targeting and imaging of NMDA receptor expression is an active area of research in pre-clinical and clinical settings. This portrays the consensus that NMDA receptors play a vital role in neurological diseases and are potential therapeutic targets. Of value are the recent structure activity relationships that have been explored to identify more suitable scaffolds for radiolabelling and imaging NMDA receptors. A promising lead is the PET tracer ¹⁸F-Ge-179, which has exhibited favourable kinetics in initial studies conducted on healthy patients.²⁰²

As in all research practices, the success of radiotracers is dependent on multiple factors ranging from chemical and radiolabelling reactions to biological examinations. For this reason, the development and assessment of radiotracers is challenging and in most cases, met with limited success. This has certainly been the case for the studies outlined in chapters 3 and 6. Nevertheless, the showpiece from this body of work is the results presented in chapters 4 and 5. Accordingly, future attention should focus primarily on this work, to help establish a multi-modal radiotracer and an early biomarker for epileptogenesis. It is noteworthy that the results presented in chapter 5 were included in a successful grant to pursue this work further.

Chapter 8 Materials and Methods

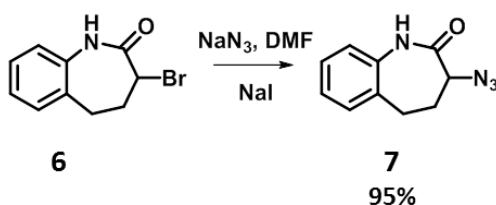
8.1 Chemistry

All reagents were purchased from Sigma Aldrich (Dorset, U.K.) except for 3-bromo-1,3,4,5-tetrahydro-benzo[b]azepin-2-one (**6**), which was purchased from Fluorochem (Derbyshire, U.K.) and Propane-1,3-diyl bis(4-methylbenzenesulfonate), which was kindly donated by Dr Eva Galante. Unless stated otherwise, all reagents were purchased and used without further purification. Column chromatography was performed on silica-gel (VWR BDH-Prolabo 40–63 μm). ^1H and ^{13}C NMR spectra were recorded at room temperature on Bruker Avance 300 or 600 instruments operating at the frequency of 300 or 600 MHz for ^1H , and 150 MHz for ^{13}C . All NMR signals are reported as chemical shifts (δ) in ppm downfield from the internal standard tetramethylsilane and were internally referenced to the residual solvent peak, CDCl_3 (7.26 ppm) or DMSO-d_6 (2.49 ppm) for ^1H , CDCl_3 (δ 77.0 ppm) or DMSO-d_6 (39.5 ppm) for ^{13}C . Melting points were determined using a Gallenkamp Sanyo melting point apparatus. IR spectra were obtained using a PerkinElmer Spectrum 100 FT-IR spectrometer. High resolution mass data were recorded on a thermo Finnigan MAT900xp (CI/EI) or a Waters LCT Premier XE (ES) mass spectrometers.

The analytical data presented for compounds **7**²⁰³, **8**²⁰⁴, **9**²⁰⁵ and **10**²⁰⁶ are in good agreement with published results, whilst **11** is a novel compound.

The following section describes the synthetic procedures to obtain a precursor for an [^{18}F]-derivative of BNZA, the results of which are presented in chapter 3, (section 3.4.3.1), pp. 69 – 72, scheme 4.

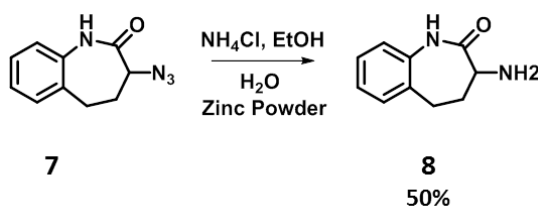
8.1.1 3-azido-4,5-dihydro-1H-benzo[b]azepin-2(3H)-one (**7**)



Scheme 9.

A solution of 3-bromo-1,3,4,5-tetrahydrobenzo[b]azepin-2-one (**6**), (10 g, 42 mmol), sodium azide (4.1 g, 1.5 equivalent) and sodium iodide (6.2 g, 1 equivalent) in Dimethyl formamide (DMF, 20 mL) was stirred under argon for 24 hours at room temperature. Upon addition of water, a solid was formed which was filtered and washed with water. After drying, **7** was obtained as a white solid (95%), mp 142 °C (lit.²⁰³ mp 142-145 °C); IR (neat): 3187, 1669, 1486, 1399, 1246 cm⁻¹; ¹H NMR (600 MHz, CDCl₃) δ in ppm: 8.14 (s, 1H), 7.29 (m, 2H), 7.12 (dd, ³J = 7.4, ⁴J = 1.0 Hz, 1H), 7.08 (d, ³J = 7.8 Hz, 1H), 3.87 (dd, ³J = 11.3, ³J = 8.0 Hz, 1H), 2.98 (m, 1H), 2.72 (m, 1H), 2.53 (m, 1H), 2.34 (m, 1H). ¹³C-NMR (150 MHz, CDCl₃) δ in ppm: 28.4 (CH₂), 35.0 (CH₂), 59.2 (CH), 122.5 (CH), 126.7 (CH), 128.2 (CH), 129.9 (CH), 133.6, 136.1, 171.3. HRMS-CI [(M+H)⁺]: 203.1048 (Calculated for C₁₀H₁₁N₄O 203.0933).

8.1.2 3-amino-4,5-dihydro-1H-benzo[b]azepin-2(3H)-one (**8**)

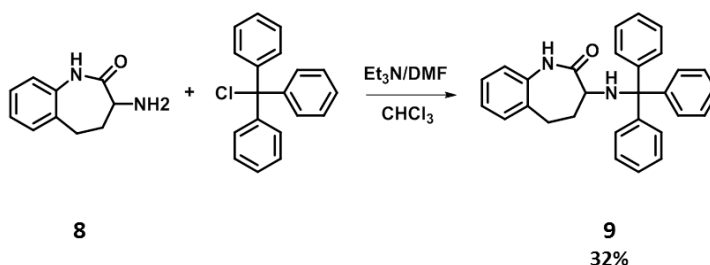


Scheme 10.

To a solution of **7** (9 g, 45 mmol) and ammonium chloride (6 g, 2.3 equivalents) in ethanol (80 ml) and water (50 ml), was added zinc powder (4 g, 1.3 equivalents). The mixture was stirred vigorously at 80 °C for 20 minutes. After cooling down to room temperature, ethyl acetate (100 ml) and aqueous ammonia (10 ml) were added. The mixture was filtered and the filtrate was washed with brine (x 3). The organic layers were combined, dried, and concentrated to leave behind a white solid, (50%), mp 145 °C (lit.²⁰⁴ mp 147-149 °C); IR (neat): 1662, 1489, 1401, 1273 cm⁻¹; ¹H-NMR (600 MHz, DMSO) δ in ppm: 8.12 (s, 1H), 7.20 (m, 2H), 7.06 (m, 1H), 6.94 (m, 1H), 2.50 (dd, ³J = 11.4, ³J = 8.0 Hz, 1H), 2.30 (m, 2H), 2.12 (dd, ²J = 13.7, ³J = 6.9 Hz, 1H), 1.88 (m, 1H), 1.7 (bs, 2H). ¹³C-NMR (150 MHz, DMSO) δ in ppm: 28.6 (CH₂), 38.9 (CH₂), 51.0 (CH), 121.9 (CH), 125.0 (CH), 127.1 (CH), 129.3 (CH),

134.2, 137.9, 175.8. HRMS-EI [(M+H)⁺]: 176.0924 m/z (calculated for C₁₀H₁₂N₂O 176.0944).

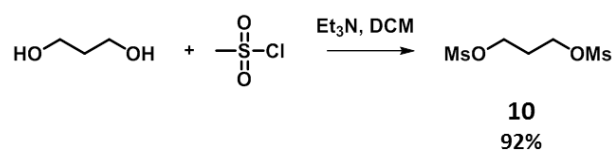
8.1.3 3-(tritylamino)-4,5-dihydro-1H-benzo[b]azepin-2(3H)-one (**9**)



Scheme 11.

Over a solution of **8** (0.7 g, 3.9 mmol) in anhydrous DMF (5 mL) was added triethylamine (TEA, 0.8 g, 1.1 mL, 2 equiv.), followed by trityl chloride (recrystallized from hexane, 1.2 g, 1.1 equiv.), dissolved in chloroform 30 mL). The mixture was stirred under argon for 20 hours, after which time, water was added (25 mL). The organic layer was collected and washed with water (x 2), dried over magnesium sulphate and the solvent removed under reduced pressure. The resulting syrupy residue was treated with methanol/water 1:1 (50 mL) in an ultrasound bath for an hour. Filtration of the mixture afforded **9** as a white solid which was purified by crystallisation using ethyl acetate (32%), mp 98 °C; IR (neat): 3055, 2858, 1667, 1447, 1384 cm⁻¹; ¹H-NMR (600 MHz, CDCl₃) δ in ppm: 7.32 (m, 6H), 7.07-7.16 (m, 12H), 6.65 (d, 7.6, 1H), 3.30 (m, 1H), 3.22 (m, 1H), 2.71 (m, 1H), 2.57 (m, 1H), 2.23 (m, 1H). ¹³C-NMR (150 MHz, CDCl₃), δ in ppm: 29.1 (CH₂), 38.9 (CH₂), 53.0 (CH), 71.6 (CH), 122.1 (CH), 126.1 (CH), 126.3 (CH), 127.5 (CH), 127.7 (CH), 128.8 (CH), 129.9 (CH), 134.8, 136.7, 146.5, 175.4. HRMS-ES [(M+Na)⁺]: m/z 441.1895 (calculated for C₂₉H₂₆N₂ONa 441.1943).

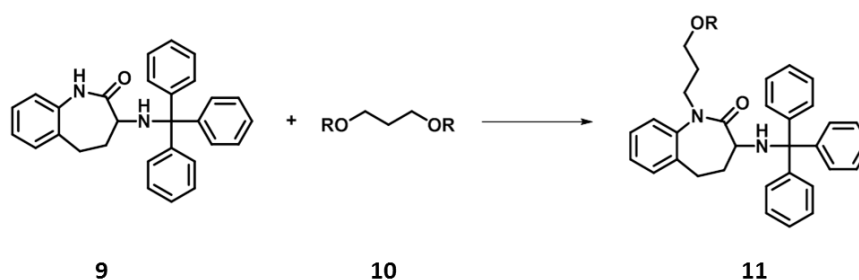
8.1.4 Propane-1,3-diyl dimethane sulfonate (10)



Scheme 12.

Propane-1,3-diol (1.5 g, 19.7 mmol) dissolved in anhydrous dichloro-methane (DCM, 20 mL) was added to a flask and placed in an ice/salt bath. Following drop-wise addition of TEA (6 g, 8.3 mL, 59 mmol, 3 equiv.) and methanesulfonyl Chloride, (5 g, 3.4 mL, 43.4 mmol, 2.2 equiv.), the mixture was stirred for 30 minutes, then for 10 minutes at room temperature. Ice cold water, (50 mL) quenched the reaction and the aqueous layer was extracted with cold DCM (x 3). The combined organic layers were washed with cold brine, dried and concentrated to leave behind a pale yellow oil (92%). IR (neat): 1328, 1167, 1024 cm^{-1} ; ^1H NMR (600 MHz, CDCl_3) δ in ppm: 4.31 (t, $J = 6.00$ Hz, 4H), 3.00 (s, 6H), 2.12 (hept. $J = 5$ Hz, 2H). ^{13}C -NMR (150 MHz, CDCl_3) δ in ppm: 27.2 (CH_2), 38.2 (CH_3), 38.2 (CH_3), 67.2 (CH_2), 67.2 (CH_2). HRMS-CI $[(\text{M}+\text{H})^+]$: 232.178 m/z (calculated for $\text{C}_5\text{H}_{12}\text{O}_6\text{S}_2$).

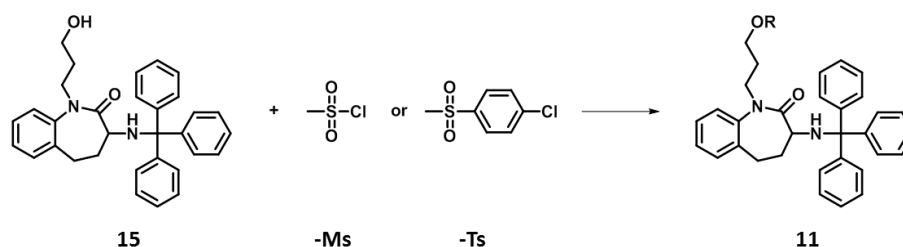
8.1.5 Attempts to synthesise the precursor (11) for ^{18}F - Radiolabelling



Scheme 13. R = -Ms, -Ts.

A two necked round bottomed flask was flame dried. Once cooled to room temperature, **9** dissolved in anhydrous DMF was added and the flask was immersed in an ice/water bath. Under a steady flow of argon, sodium hydride (NaH) (1.1

equiv.) was added. Thirty minutes later, propane-1,3-diyl bis(4-methylbenzenesulfonate) or propane-1,3-diyl dimethanesulfonate (1.5 equiv.) dissolved in anhydrous DMF was added drop wise. The reaction was left to stir at room temperature overnight and was then quenched with water. The resulting precipitate was filtered and washed further with water. Efforts to purify the solid involved column chromatography, using an eluent of petroleum and ethyl acetate, which reached a final gradient of (7:3). The analytical results for the obtained product revealed an amalgamation of structures including **9**, **10**, **15** and only a small fraction of **11**.



Scheme 14.

15 dissolved in anhydrous DCM was added to a cooled two necked round bottomed flask which had been flame dried. The flask was then immersed in an ice/water bath to which TEA, (3 equiv.) and methane- or toluene- sulfonyl chloride (MsCl or TsCl, 2.2 equiv.) was added drop wise. The mixture was stirred for 90 minutes at room temperature and then quenched with ice cold water. The aqueous layer was separated from the organic layer and was washed thrice with cold DCM. The organic fractions were then washed with cold brine (x 3), dried over magnesium sulphate and concentrated. Analysis of the crude mixture by LC-MS revealed a mixture of substances and large amounts of impurities whose identities were difficult to determine.

8.1.6 VCAM-MPIO (used in the studies described in chapters 4 and 5).



Scheme 15.

Monoclonal antibodies specific to rat VCAM-1 (MR106) (ebioscience, USA) were conjugated to micron sized particles of iron oxide (MPIOs, 1 μm diameter, iron content: 26%, Invitrogen, Life Technologies, U.K.). In general, 40 μg of antibody were reacted per mg of iron/MPIO (Fe-MPIO) via a tosyl alkylation reaction following the manufacturers' guidelines and as previously reported.¹¹⁵ First, MPIOs were washed: the beads in the original vial were resuspended by vortexing for > 30 seconds. The beads (5 mg of Fe per Kg of animal weight, 19.2 mg MPIO, 38 μl) were then placed in an eppendorf tube to which sodium borate buffer solution (1000 μl , 0.1 M, pH 9.5) was added and vortexed for > 30 seconds. The eppendorf was placed next to a magnet (0.5 T, nickel plated, K&J Magnetics Inc. USA) to immobilise the particles and the supernatant was removed with a Gilson pipette (Gilson Scientific LTD. U.K.). After removing the tube from the magnet, to the washed beads was then added sodium borate solution (415 μl , 0.1 M, pH 9.5) followed by the antibodies (approx. 154 μg , 154 μl). Finally, ammonium sulphate solution (138 μl , 3 M, pH 9.4) was added and the mixture was incubated overnight at 37 $^{\circ}\text{C}$ with slow stirring to ensure the beads did not settle during the incubation period. Following antibody conjugation, a magnet was used to immobilise VCAM-MPIO. The supernatant containing unbound antibodies was removed and VCAM-MPIO was re-suspended in heparinised PBS (0.1%, 100 μL).

8.2 Radiochemistry

[¹²⁵I]NaI was purchased from Perkin Elmer Life and Analytical Sciences (MA, USA) as a non-carrier added solution in reductant free 10⁻⁵ M aqueous sodium hydroxide

solution (pH 8 - 11). Non-carrier refers to samples that have no non-radioactive additives but may contain naturally occurring isotopic dilutions. The SA of this solution was reported to be 629 GBq mg⁻¹.

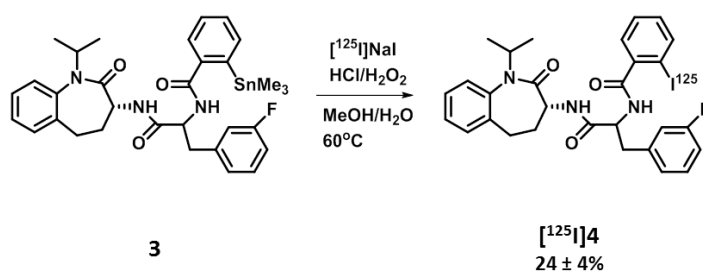
HPLC analysis and purification were performed on an Agilent 1200 HPLC system equipped with a 1200 Series Diode Array Detector. Runs were monitored with a 254 UV detector and a Raytest Gabi Sodium Iodide (NaI) detector.

Isolated Radiochemical Yields (RCY) were measured using a Curiemontor 4 ion chamber (PTW, Germany).

8.2.1 Radioiodinated BNZA Analogue ([¹²⁵I]4) – (Evaluated in the study discussed in chapter 3 (section 3.4.1), pp. 61- 69)

For HPLC purification and analytical runs, a C18 Agilent Eclipse Plus column (4.6 x 150 mm, 5 μm) was used. The solvent systems used were water (0.1% TFA, solvent A), and methanol (0.1% TFA, solvent B) with a flow rate of 1 mL min⁻¹.

The precursor (N-(3-(3-fluorophenyl)-1-(((R)-1-isopropyl-2-oxo-2,3,4,5-tetrahydro-1H-benzo[b]azepin-3-yl)amino)-1-oxopropan-2-yl)-2-(trimethylstannyl)benzamide, **3**) to obtain the radioiodinated BNZA analogue ([¹²⁵I]4) was synthesised by Dr Perèz-Medina.



Scheme 16.

Hydrochloric acid (HCl, 60 μL, 0.4 M), hydrogen peroxide (H₂O₂, 50 μL, 6%) and [¹²⁵I]NaI (5 μL, 130 MBq), were sequentially added to **3** (50 μg) dissolved in methanol (100 μL). The mixture was left to stir for 30 minutes at 60°C. The cooled

mixture was then diluted with MeOH/water 1:1 (500 μ L) and injected into the HPLC system. The two diastereoisomer products of [125 I]**4** were separated by radio-HPLC with the following gradient: 60 % B to 90 % B over 32 min. Each diastereoisomer obtained was then diluted with water (10 mL) and passed through a Sep-Pak C18 light cartridge (Waters) activated with methanol (5 mL) and water (10 mL). The radioactive diastereoisomers were eluted with ethanol (0.5 mL) which was removed under a stream of nitrogen. Prior to administration into the animals, the radioactive diastereoisomers were formulated in 10% ethanol/saline solution and filtered using a Millex-GV 0.22 μ m filter.

8.2.2 [125 I]VCAM-MPIO (Assessed in a rat model of cerebral inflammation: Chapter 4 (pp. 81 – 94) and in the lithium pilocarpine model of SE: Chapter 5 (pp. 102 – 108))

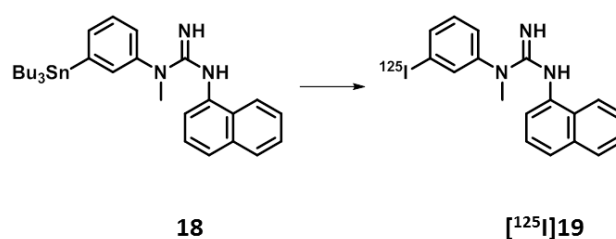
VCAM-MPIO (19.2 mg MPIO, approx. 40 μ l), suspended in heparinised PBS (100 μ L, pH 7.4), was transferred to pre-coated 1,3,4,6-tetrachloro-3 α ,6 α -diphenylglycouril (Iodogen) tubes (Thermo Fischer Scientific, USA). To this, [125 I]NaI (30-150 MBq) was added and the mixture was left to incubate at room temperature for 30 minutes. After this time, the radioactive mixture was transferred into an eppendorf tube and radiolabelled VCAM-MPIO ([125 I]VCAM-MPIO) was purified by magnetic immobilisation (RCY = 85 \pm 5% (n = 11)). The particles were washed with heparinised PBS (1 mL, x 5) prior to their administration into rats.

Using this same protocol, [125 I]IgG-MPIO was synthesised using non-specific IgG antibodies (Southern Biotech. USA) (RCY = 82% (n = 11)).

8.2.3 [125 I]CNS- 1261 ([125 I]19**)** – Investigated in the lithium pilocarpine model of SE (chapter 6, pp. 113 – 121)

The tri-butylstannyl precursor (**18**) and non-radiolabelled CNS-1261 (**19**) were purchased from ABX-advanced biochemical compounds (Radeberg, Germany). Upon arrival, the compounds were separated into 50 μ g fractions using DCM, which was removed under a stream of nitrogen. The fractions were stored under nitrogen at - 4 $^{\circ}$ C.

HPLC analysis and purification was performed with a semi preparative C18 Agilent Eclipse Plus column (4.6 x 150 mm, 5 μm particle size) and a solvent system of water (0.1% TFA, solvent A) and methanol (0.1% TFA, solvent B) with a flow rate of 3 mL min⁻¹. Purification and analytical runs were carried out using a gradient elution of 40% to 70% solvent B over 15 min, then up to 95% within 5 min, at 95% for 8 min before returning to 40% of solvent B in 12 min.



Scheme 17.

Method 1: **18** (50 μg) was dissolved in MeOH (100 μl). To this was added HCl (60 μl , 0.4 M), H₂O₂ (50 μl , 6%) and [¹²⁵I]NaI in water (25 μl , 2.6 MBq). The mixture was vortexed and left to stand at room temperature. After 10 and 30 min, an aliquot (quenched with H₂O/MeOH 60:40, 500 μL) was co-injected with **19** diluted in H₂O/MeOH (60:40, 500 μL) for HPLC analysis, (Figure 41 a and b)

Method 2: HCl (250 μl , 0.1 M), followed by a solution of **18** (50 μg) in ethanol (100 μl), was added to [¹²⁵I]NaI in water (2-4 MBq, 25-35 μl). H₂O₂ (50 μl , 3%) was then added and the resulting mixture was vortexed and left to stand at room temperature. 10 and 60 min later, an aliquot of the reaction mixture was diluted with H₂O and MeOH (60:40, 500 μL) and co-injected with **19** diluted in H₂O/MeOH (60:40, 500 μL) for HPLC analysis (Figure 41 c and d).

An aliquot, obtained 30 min after incubation, was diluted with H₂O/MeOH (60:40, 500 μL) and injected for HPLC analysis (Figure 41 e). The eluent containing the radioiodinated product ([¹²⁵I]**19**) was collected and diluted with water (10 mL) before passing through a Sep-Pak C18 light cartridge (Waters, Herts., U.K.), which had been activated with MeOH (5 mL) and H₂O (10 mL). The loaded cartridge was washed with water (10 mL) and [¹²⁵I]**19** was released with ethanol (0.4 mL, > 99%

recovery, n =5). The ethanol was then removed by a stream of nitrogen. Prior to administration into the animals, [¹²⁵I]**19** was formulated in 10% ethanol/saline solution and filtered using a Millex-GV 0.22 µm filter (Fischer Scientific, Loughborough, U.K.). The purity of the product fraction was determined by co-injection with the non-radiolabelled compound **19** into the HPLC system (Figure 41 f).

Method 3: Peracetic acid was prepared 2 hours prior to use from 30% H₂O₂ (1.7 mL) and glacial acetic acid (1 mL). In a vial containing **18** (50 µg) was added acetic acid (130 µl), [¹²⁵I]NaI in water (30 µl, 3 MBq) and peracetic acid (20 µl). The mixture was vortexed and left to stand at room temperature. After 10 and 30 min, aliquots of the reaction mixture were diluted with H₂O/MeOH (60:40, 500 µL) and co-injected with **19** for HPLC analysis (Figure 41 g and h).

Method 4: To a vial containing **18** (50 µg) was added 5% acetic acid diluted in MeOH (34 µl) and 0.2% peracetic acid diluted in acetic acid (10 µl). [¹²⁵I]NaI in water (30 µl, 3 MBq) was then added and 30 min later, H₂O/MeOH (60:40, 500 µL) quenched the solution which was then co-injected with **19** for HPLC analysis (Figure 41 i).

8.3 Biological Evaluations

8.3.1 General

All animal work conducted as part of this PhD was performed in accordance with the U.K. Animal (Scientific Procedures) 1986 Act and institutional ethics regulations. Upon arrival, animals were housed in a controlled environment: temperature = 21 °C ± 2 °C, humidity = 55% ± 10%, 12 hour light/dark cycle with 30 min twilight between the switch to light and to dark. Food and water was provided *ad libitum*.

The species used for the studies presented in chapter 3 were female Balb/C mice (6–10 weeks old and 15–20 g of weight), which were obtained from Charles River, UK. Adult male Sprague-Dawley rats, used for the studies discussed in chapters 4-6 (170 – 270 g) were obtained from the animal facility breeding colony of University College London (UCL).

SPECT/CT imaging was performed on a Nano-SPECT/CT small animal *in vivo* scanner (Mediso, Hungary). MRI imaging was performed using a 9.4 Tesla horizontal bore scanner (Agilent Technologies, USA) with a shielded gradient system (Agilent Technologies) and a 4-channel rat head phased-array coil (Rapid Biomedical GmbH, Germany). For the duration of *in vivo* imaging, a physiological monitoring system (SA Instruments, USA) was used to monitor respiration rate and rectal temperature whilst isoflurane (1% in pure oxygen) was used to maintain anaesthesia. Temperature was maintained at 37 ± 0.5 °C using an air and water tubing warming system.

The amounts of radioactivity for dosing was measured in a Curiementor 4 ion chamber (PTW, Germany) whilst radioactivity in tissues of interest was measured in a Wizard² 2470 Automatic Gamma Counter (Perkin Elmer, U.K.).

For phosphorimaging, the animals were euthanized, their brains were removed and fixed overnight in 4% paraformaldehyde (PFA) in PBS (pH 7.4). The brains were then cryoprotected overnight in sucrose solution (45%) and sectioned coronally. Brains were sectioned using a cryostat (Bright Instrument Co Ltd. U.K.) in which the chamber and specimen temperature was set at -15 °C \pm 3 °C. The sections were mounted on polysine coated glass slides (25 x 75 x 1.0 mm, VWR international LTD. U.K.) and placed onto unmounted GP 20 x 25 cm phosphor screens (VWR international LTD, U.K.), which were scanned on a Typhoon 9410 Trio⁺ Phosphorimager (GE Healthcare, U.K.). The phosphorimages were analysed using the Typhoon Image Quant software or Image J. MIN-R Screen cleaner wipes were purchased from Carestream Dental LTD. U.K.

Optical images of the brain sections were captured on a bright field AxioSkop 2 system (Gottingen, Germany) at x 5 magnification. Images of the brain sections were processed using the tiling and stitching method (www.mediacy.com, Application Highlights – Stitching and Tiling Images) on the Zeiss Axio Vision 4.8 software (Imaging Associates, Germany).²⁰⁷

Animal Models

Cerebral Inflammation (For the studies discussed in chapter 4, pp.81 – 94)

Adult male Sprague-Dawley rats were anaesthetised using a combination of isoflurane (1% in pure oxygen) and urethane (administered intraperitoneally, 1.5 g/kg). TNF- α (300 ng, Life Technologies LTD. U.K.) in saline (5 μ L) was injected into the right striatum (coordinates from bregma: -0.5 mm anteroposterior, 3 mm mediolateral, 4 mm dorsoventral from dura) using a Hamilton syringe (Hamilton Company, USA) attached to a 31G needle. Saline (5 μ L) was administered in place of TNF- α for the control group.

Lithium Pilocarpine Model of Status Epilepticus (Used in the studies presented in chapter 5, pp.102 – 108 and chapter 6, pp. 113 – 121)

All drugs were administered intraperitoneally. Adult, male Sprague Dawley rats were injected with lithium chloride (3 mEq/kg) 3 h prior to methyl scopolamine nitrate (5 mg/kg) administration. Methyl scopolamine nitrate was administered to reduce the peripheral effects of pilocarpine.²⁰⁸ 30 min later, pilocarpine hydrochloride (30 mg/kg) was administered in order to induce SE. Animals were behaviourally assessed and the onset of SE was defined as stage 3 on the Racine scale. Diazepam (10 mg/kg, Hameln Pharmaceuticals, U.K.) was administered 90 min after SE onset to terminate the seizures. Further injections of diazepam were administered as required. The control group (SALINE_{VCAM}) received lithium chloride, methyl scopolamine nitrate and saline in place of pilocarpine hydrochloride.

All animals induced with SE were monitored daily. Animals whose weight had decreased by more than 20% of their initial weight were not included in the studies.

8.3.2 Radioiodinated BNZA and WIN17317-3 Analogues *(results of which are presented in chapter 3, pp. 61 - 78)*

Upon arrival, female Balb/C mice were allowed to acclimatise for at least 5 days in a room with constant temperature and humidity. The radiotracers (suspended in 150 –

300 μ L saline solution (5–7% ethanol)) were administered intravenously via the lateral tail vein by Mr M Robson, who also performed the cardiac punctures to obtain blood.

Biodistribution (*results shown in Table 3, p. 65 and in Table 4, p. 75*)

Following administration of the radiotracer (0.2–0.4 MBq), the mice were anesthetized at predetermined time points with isoflurane. Blood was obtained and the animals were then sacrificed by cervical dislocation. The radioactivity content in the tissues of interest, (large and small intestine, stomach, kidneys, brain, bone (femur), liver, lungs, heart, skin, spleen, bladder, tail) was measured. For each time point, $n = 4$ and the radioactivity uptake was calculated as the mean percentage injected dose per gram of tissue \pm S.D.

Metabolite Analysis (*results shown in Figure 20, p. 66 and in Figure 24, p. 76*)

In collaboration with Dr C. Perèz-Medina

Female Balb/C mice were injected with 2.4–3.4 MBq of the radiotracer. The mice were then anesthetized using isoflurane 5, 15, 30 and 60 min post tracer injection. Blood and brains were obtained.

Blood Preparation

Blood was collected into heparised tubes and centrifuged at 13 000 rpm for 1 min to separate plasma. 300 μ L of plasma were mixed with 1200 μ L of cold acetonitrile, vortexed and centrifuged at 13 000 rpm for 1 min. The supernatant was then mixed with 900 μ L of water.

Brain Preparation

Brain tissues were mixed with 1.5 mL acetonitrile–water (2 : 1) and homogenized, vortexed and centrifuged at 13 000 rpm for 1 min. The resulting supernatant was then mixed with 500 μ L of water and the solution was centrifuged as described above. Pellets and supernatants were separated and counted for radioactivity to determine recovery efficiency.

An aliquot (1000 μL) of the supernatant from the plasma and brain extracts was analysed by reverse-phase HPLC (Agilent C18 XDB column, 4.6×150 mm, $5 \mu\text{m}$) using a gradient elution from 50 to 90% Methanol (0.1% formic acid) over 15 minutes at a flow rate of 1 mL min^{-1} . Results are expressed as percentages of the total activity administered into the animals \pm S.D.

SPECT/CT Imaging (*Figure 21, p. 67 and Figure 25, p. 76*)

Female Balb/C mice (4–10 weeks old) were injected with 20–35 MBq of radiotracer via the lateral tail vein. Animals were then anaesthetised with isoflurane (4% in oxygen) and placed in a prone position. Scans were performed approximately 20 min post tracer administration using 1 mm pinhole apertures. Whole body scans consisted of sixteen projections of varying duration (10-60 seconds per projection) and CT were recorded once the SPECT scans were completed. SPECT images were reconstructed using HiSPECT software (Bioscan, USA) with the following parameters: smoothing = 35%, iterations = 9 and *In Vivo* Scope software was used for CT image reconstruction.

8.3.3 [^{125}I]VCAM-MPIO (*Assessed in the studies presented in chapter 4 and 5*)

[^{125}I]VCAM-MPIO or [^{125}I]IgG-MPIO, suspended in heparinised PBS (0.1%, 1 mL), was administered via a cannula implanted in the external right jugular vein of anaesthetised rats. The CA was administered approximately 7 hours after the administration of TNF- α and 20 hours after the termination of SE. After each administration, the cannula was flushed with PBS (1 mL) to remove residual radioactivity.

Blood Clearance and Biodistribution (*results represented in Figure 26, p. 83*)

Blood samples ($n = 3$) were collected via a jugular vein cannula at predetermined time points (approximately: 85, 120, 170, 230, 290 s) following [^{125}I]VCAM-MPIO administration in rats anaesthetised using a combination of isoflurane and urethane. For biodistribution studies, [^{125}I]VCAM-MPIO in PBS (8-10 MBq, 1 mL) was

administered via the lateral tail vein (n = 3). 10 minutes later, the rats were anaesthetised with isoflurane (4% in pure oxygen) and blood was sampled through cardiac puncture. Animals were then sacrificed by cervical dislocation and the organs of interest were removed. The radioactivity content in the blood samples and organs was measured and results are expressed as injected dose per gram of tissue \pm S.D.

In Vivo Imaging (images displayed on p. 85 - Figure 27, p. 86- Figure 28, p. 104 - Figure 35 and p. 105- Figure 36)

In vivo SPECT/CT was performed approximately 20 min post CA administration. A CT scan was conducted with the following parameters: radial field of view (FOV) = 40.5 mm², axial FOV = 40.9 mm, exposure time per projection = 1 s, 360 projections and 55 KvP tube voltage, which resulted in an acquisition time of 6 minutes. Helical SPECT was performed across the same FOV using 2.5 mm pinhole apertures with 20 projections and an exposure time of 15 s per projection. For dynamic imaging, 5 scans were performed in succession resulting in a total acquisition time of 25 min. All SPECT/CT images shown are from the first frames captured 20 min post CA administration. To show the *in vivo* distribution of the CA, a scan was performed across the entire FOV of the animal with 2.5 mm pinhole apertures and an imaging time of 40 min.

In vivo MRI was performed immediately after SPECT/CT imaging, approximately 1 h following administration of [¹²⁵I]VCAM-MPIO or [¹²⁵I]IgG-MPIO (disease models and control groups). Iron oxide was detected using a 3D gradient echo sequence (TR = 100 ms, TE = 11 ms, matrix = 192×192×160, FOV = 25×25×25 mm³, acquisition time \approx 51 min).

Phosphorimaging

Sectioning (20 μ m) of the brain commenced close to the bregma. The sections were subsequently exposed on phosphor screens for 15 minutes. After this time, the screens were scanned by the Phosphorimager, (25 μ m resolution, acquisition time =

2 h 30 min) and the resulting images were processed by Image J (Softonic, Spain). The relative distance of the slices displayed either anterior or posterior from the bregma are estimated in mm based on the stereotaxic coordinates determined by Paxinos and Watson.¹²¹

As the radioactivity levels in the brain sections were above the optimal range for phosphorimaging, one animal in the TNF- α group was administered a reduced dose of [¹²⁵I]VCAM-MPIO (3 mg of Fe/kg, 30 KBq/g). The animal was sacrificed 1 h post CA administration, the brain was removed and treated with PFA and sucrose as previously described. Coronal sections (20 μ m) of the brain were exposed on a phosphor screen for 1 week, which was then scanned using the parameters described above. Images from this study are displayed on p. 90, Figure 32).

Image Analysis

SPECT images were reconstructed in HiSPECT using the following parameters: smoothing = 45%, resolution = 67%, number of iterations = 10. CT reconstruction was performed in *InVivo* Quant.

MRI data were processed and quantified in MATLAB 2013a (MathWorks, USA). ROIs were defined over the left or right cerebral hemisphere surrounding the injection site. These consisted of 30 consecutive slices (\approx 3 mm) anterior and 30 consecutive slices posterior to the injection site. Hypointense regions are expressed as the percentage contrast void across the brain volume.

Coregistration of MRI and CT images shown in chapter 4, Figure 28, p. 86 was performed in AMIRA® (Visualization Sciences Group, USA), on the gradient images of the brain extracted MRI magnitude data and the CT intensity images using normalised correlation as the cost function. This was performed by Dr B Duffy.

For the SPECT quantification presented in chapter 4, p.88, Figure 30 ROIs as defined on MRI images were propagated to the SPECT/CT native space using the same transformation matrix. In this way, identical ROIs were used for both the MRI and SPECT analysis. Background signal intensity was defined as the mean signal intensity across all non-brain tissue in the entire field of view. The binding of CA is

expressed as the signal-to-background ratio to normalise for body weight and the amount of radioactivity that was administered in each animal.

Statistical analysis was performed in MATLAB by Dr B Duffy. All error bars are shown as mean \pm standard error of the mean (SEM). Statistical significance was assigned at $p < 0.05$.

For the results presented in chapter 5, p. 106. Figure 38, SPECT signals in each image frame were quantified from the re-constructed images using *InVivo* Quant (Mediso, Hungary). Regions of interest (ROIs) were manually drawn across the whole brain. Identical ROIs were used to analyse the frames ($n = 5$) for each animal.

8.3.4 [¹²⁵I]CNS-1261 (*Results of which are discussed in chapter 6, pp. 113 - 121*)

Phosphorimaging

Brain slices (16 μ m) were exposed on a phosphor screen along with a set of [¹²⁵I]NaI standards (0.5 - 0.0001 MBq) for one week, after which the screen was scanned, (25 μ m resolution, acquisition time = 2 h 30 min).

HE Staining (Represented on Figure 40, p. 114)

Brain slices (16 μ m) were stained with Hematoxylin and Eosin (HE) using a protocol similar to Zeller et al.²⁰⁹ Tissue sections were re-hydrated by agitation in H₂O for 30 seconds. The slides were then dipped into Harris' hematoxylin and agitated for 5 minutes. The slides were rinsed in H₂O for 1 minute and staining intensity was determined under the microscope. Further agitation in hematoxylin was performed if required. The slides were next immersed in Eosin solution (1%) for 4-5 minutes. The sections were then dehydrated by 30 second incubations in 70%, and 100% (x 2) ethanol. The alcohol was extracted with 10 second immersions in histoclear (III to I) (Fischer Scientific, U.K.). Using Xylene, the sections were then cover slipped (VWR International LTD.).

References

1. Piccini, P.; Whone, A. Functional brain imaging in the differential diagnosis of Parkinson's disease. *Lancet Neurol.* **2004**, *3*, 284-290.
2. Davila-Roman, V. G.; Vedala, G.; Herrero, P.; de las, F. L.; Rogers, J. G.; Kelly, D. P.; Gropler, R. J. Altered myocardial fatty acid and glucose metabolism in idiopathic dilated cardiomyopathy. *J. Am. Coll. Cardiol.* **2002**, *40*, 271-277.
3. Engler, H.; Forsberg, A.; Almkvist, O.; Blomquist, G.; Larsson, E.; Savitcheva, I.; Wall, A.; Ringheim, A.; Langstrom, B.; Nordberg, A. Two-year follow-up of amyloid deposition in patients with Alzheimer's disease. *Brain* **2006**, *129*, 2856-2866.
4. Juweid, M. E.; Cheson, B. D. Positron-emission tomography and assessment of cancer therapy. *N. Engl. J. Med.* **2006**, *354*, 496-507.
5. Townsend, D. W. Multimodality imaging of structure and function. *Phys. Med. Biol.* **2008**, *53*, R1-R39.
6. Lang, T. F.; Hasegawa, B. H.; Liew, S. C.; Brown, J. K.; Blankespoor, S. C.; Reilly, S. M.; Gingold, E. L.; Cann, C. E. Description of a prototype emission-transmission computed tomography imaging system. *J. Nucl. Med.* **1992**, *33*, 1881-1887.
7. Hasegawa, B. H.; Iwata, K.; Wong, K. H.; Wu, M. C.; Da Silva, A. J.; Tang, H. R.; Barber, W. C.; Hwang, A. H.; Sakdinawat, A. E. Dual-modality imaging of function and physiology. *Acad. Radiol.* **2002**, *9*, 1305-1321.
8. Kalki, K.; Blankespoor, S. C.; Brown, J. K.; Hasegawa, B. H.; Dae, M. W.; Chin, M.; Stillson, C. Myocardial perfusion imaging with a combined x-ray CT and SPECT system. *J. Nucl. Med.* **1997**, *38*, 1535-1540.
9. Townsend, D. W. Positron emission tomography/computed tomography. *Semin. Nucl. Med.* **2008**, *38*, 152-166.
10. Garlick, P. B. Simultaneous PET and NMR--initial results from isolated, perfused rat hearts. *Br. J. Radiol.* **2002**, *75 Spec No*, S60-S66.
11. Wehrl, H. F.; Judenhofer, M. S.; Wiehr, S.; Pichler, B. J. Pre-clinical PET/MR: technological advances and new perspectives in biomedical research. *Eur. J. Nucl. Med. Mol. Imaging* **2009**, *36 Suppl 1*, S56-S68.
12. Groch, M. W.; Erwin, W. D. SPECT in the year 2000: basic principles. *J. Nucl. Med. Technol.* **2000**, *28*, 233-244.
13. Chatziioannou, A. F. Instrumentation for molecular imaging in preclinical research: Micro-PET and Micro-SPECT. *Proc. Am. Thorac. Soc.* **2005**, *2*, 533-11.

14. Cho, Z. H.; Farukhi, M. R. Bismuth germanate as a potential scintillation detector in positron cameras. *J. Nucl. Med.* **1977**, *18*, 840-844.
15. Khalil, M. M.; Tremoleda, J. L.; Bayomy, T. B.; Gsell, W. Molecular SPECT Imaging: An Overview. *Int. J. Mol. Imaging* **2011**, *2011*, 796025.
16. Cheng, D.; Wang, Y.; Liu, X.; Pretorius, P. H.; Liang, M.; Rusckowski, M.; Hnatowich, D. J. Comparison of ¹⁸F PET and ^{99m}Tc SPECT imaging in phantoms and in tumored mice. *Bioconjug. Chem.* **2010**, *21*, 1565-1570.
17. Moses, W. W. Fundamental Limits of Spatial Resolution in PET. *Nucl. Instrum. Methods Phys. Res. A* **2011**, *648 Supplement 1*, S236-S240.
18. Tai, Y. C.; Ruangma, A.; Rowland, D.; Siegel, S.; Newport, D. F.; Chow, P. L.; Laforest, R. Performance evaluation of the microPET focus: a third-generation microPET scanner dedicated to animal imaging. *J. Nucl. Med.* **2005**, *46*, 455-463.
19. Johnstrom, P.; Bird, J. L.; Davenport, A. P. Quantitative phosphor imaging autoradiography of radioligands for positron emission tomography. *Methods Mol. Biol.* **2012**, *897*, 205-220.
20. Johnstrom, P.; Davenport, A. P. Imaging and characterization of radioligands for positron emission tomography using quantitative phosphor imaging autoradiography. *Methods Mol. Biol.* **2005**, *306*, 203-216.
21. Blaufox, M. D.; Dubovsky, E. V.; Hilson, A. J.; Taylor, A., Jr.; de, Z. R. Report of the Working Party Group on Determining the Radionuclide of Choice. *Am. J. Hypertens.* **1991**, *4*, 747S-748S.
22. Braghirolli, A. M.; Waissmann, W.; da Silva, J. B.; dos Santos, G. R. Production of iodine-124 and its applications in nuclear medicine. *Appl. Radiat. Isot.* **2014**, *90*, 138-148.
23. Wyszomirska, A. Iodine-131 for therapy of thyroid diseases. Physical and biological basis. *Nucl. Med. Rev. Cent. East Eur.* **2012**, *15*, 120-123.
24. Yalow, R. S. Radioimmunoassay. *Annu. Rev. Biophys. Bioeng.* **1980**, *9*, 327-345.
25. Schwarz, S. B.; Thon, N.; Nikolajek, K.; Niyazi, M.; Tonn, J. C.; Belka, C.; Kreth, F. W. Iodine-125 brachytherapy for brain tumours--a review. *Radiat. Oncol.* **2012**, *7*, 30.
26. Lin, J.; Sahakian, D. C.; de Moraes, S. M.; Xu, J. J.; Polzer, R. J.; Winter, S. M. The role of absorption, distribution, metabolism, excretion and toxicity in drug discovery. *Curr. Top. Med. Chem.* **2003**, *3*, 1125-1154.
27. Rowland, M.; Benet, L. Z.; Graham, G. G. Clearance concepts in pharmacokinetics. *J. Pharmacokinet. Biopharm.* **1973**, *1*, 123-136.
28. Lee, S. Y.; Choe, Y. S.; Kim, D. H.; Park, B. N.; Kim, S. E.; Choi, Y.; Lee, K. H.; Lee, J.; Kim, B. T. A simple and efficient in vitro method for metabolism studies of radiotracers. *Nucl. Med. Biol.* **2001**, *28*, 391-395.

29. Lipinski, C. A.; Lombardo, F.; Dominy, B. W.; Feeney, P. J. Experimental and computational approaches to estimate solubility and permeability in drug discovery and development settings. *Adv. Drug Deliv. Rev.* **2001**, *46*, 3-26.
 30. Longmire, M.; Choyke, P. L.; Kobayashi, H. Clearance properties of nano-sized particles and molecules as imaging agents: considerations and caveats. *Nanomedicine. (Lond)* **2008**, *3*, 703-717.
 31. Mannhold, R.; Poda, G. I.; Ostermann, C.; Tetko, I. V. Calculation of molecular lipophilicity: State-of-the-art and comparison of log P methods on more than 96,000 compounds. *J. Pharm. Sci.* **2009**, *98*, 861-893.
 32. Purser, S.; Moore, P. R.; Swallow, S.; Gouverneur, V. Fluorine in medicinal chemistry. *Chem. Soc. Rev.* **2008**, *37*, 320-330.
 33. Smith, D. A.; Di, L.; Kerns, E. H. The effect of plasma protein binding on in vivo efficacy: misconceptions in drug discovery. *Nat. Rev. Drug Discov.* **2010**, *9*, 929-939.
 34. Valko, K.; Nunhuck, S.; Bevan, C.; Abraham, M. H.; Reynolds, D. P. Fast gradient HPLC method to determine compounds binding to human serum albumin. Relationships with octanol/water and immobilized artificial membrane lipophilicity. *J. Pharm. Sci.* **2003**, *92*, 2236-2248.
 35. Weiland, G. A.; Molinoff, P. B. Quantitative analysis of drug-receptor interactions: I. Determination of kinetic and equilibrium properties. *Life Sci.* **1981**, *29*, 313-330.
 36. Maguire, J. J.; Kuc, R. E.; Davenport, A. P. Radioligand binding assays and their analysis. *Methods Mol. Biol.* **2012**, *897*, 31-77.
 37. Cheng, Y.; Prusoff, W. H. Relationship between the inhibition constant (K₁) and the concentration of inhibitor which causes 50 per cent inhibition (I₅₀) of an enzymatic reaction. *Biochem. Pharmacol.* **1973**, *22*, 3099-3108.
 38. Nunn, A. D. Molecular imaging and personalized medicine: an uncertain future. *Cancer Biother. Radiopharm.* **2007**, *22*, 722-739.
 39. Adriana Alexandre dos Santos Tavares. Development of Novel Radiotracers as Tools for Imaging the Human Brain. 2011. University of Glasgow.
- Ref Type: Thesis/Dissertation
40. de Kemp, R. A.; Epstein, F. H.; Catana, C.; Tsui, B. M.; Ritman, E. L. Small-animal molecular imaging methods. *J. Nucl. Med.* **2010**, *51 Suppl 1*, 18S-32S.
 41. Hildebrandt, I. J.; Su, H.; Weber, W. A. Anesthesia and other considerations for in vivo imaging of small animals. *ILAR. J.* **2008**, *49*, 17-26.
 42. Wong, D. F.; Pomper, M. G. Predicting the success of a radiopharmaceutical for in vivo imaging of central nervous system neuroreceptor systems. *Mol. Imaging Biol.* **2003**, *5*, 350-362.

43. Hargreaves, R. J. The role of molecular imaging in drug discovery and development. *Clin. Pharmacol. Ther.* **2008**, *83*, 349-353.
44. Ballabh, P.; Braun, A.; Nedergaard, M. The blood-brain barrier: an overview: structure, regulation, and clinical implications. *Neurobiol. Dis.* **2004**, *16*, 1-13.
45. Pike, V. W. PET radiotracers: crossing the blood-brain barrier and surviving metabolism. *Trends Pharmacol. Sci.* **2009**, *30*, 431-440.
46. Donohue, S. R.; Krushinski, J. H.; Pike, V. W.; Chernet, E.; Phebus, L.; Chesterfield, A. K.; Felder, C. C.; Halldin, C.; Schaus, J. M. Synthesis, ex vivo evaluation, and radiolabeling of potent 1,5-diphenylpyrrolidin-2-one cannabinoid subtype-1 receptor ligands as candidates for in vivo imaging. *J. Med. Chem.* **2008**, *51*, 5833-5842.
47. Eckelman, W. C.; Paik, C. H.; Reba, R. C. Radiolabeling of antibodies. *Cancer Res.* **1980**, *40*, 3036-3042.
48. Fraker, P. J.; Speck, J. C., Jr. Protein and cell membrane iodinations with a sparingly soluble chloroamide, 1,3,4,6-tetrachloro-3a,6a-diphrenylglycoluril. *Biochem. Biophys. Res. Commun.* **1978**, *80*, 849-857.
49. Bolton, A. E.; Hunter, W. M. The labelling of proteins to high specific radioactivities by conjugation to a ¹²⁵I-containing acylating agent. *Biochem. J.* **1973**, *133*, 529-539.
50. Krohn, K. A.; Knight, L. C.; Harwig, J. F.; Welch, M. J. Differences in the sites of iodination of proteins following four methods of radioiodination. *Biochim. Biophys. Acta* **1977**, *490*, 497-505.
51. Eersels, J. L.; Mertens, J.; Herscheid, J. D. The Cu(+)-assisted radioiodination Kit: Mechanistic study of unexplored parameters concerning the acidity and redox properties of the reaction medium. *Appl. Radiat. Isot.* **2010**, *68*, 309-313.
52. Wilbur, D. S.; Hamlin, D. K.; Srivastava, R. R.; Burns, H. D. Synthesis and radioiodination of N-Boc-p-(tri-n-butylstannyl)-L-phenylalanine tetrafluorophenyl ester: preparation of a radiolabeled phenylalanine derivative for peptide synthesis. *Bioconjug. Chem.* **1993**, *4*, 574-580.
53. McPherson, D. W.; Luo, H.; Kropp, J.; Knapp, F. F., Jr. Improved radioiodination of 1,2-dipalmitoyl-3-IPPA via a tributyltin intermediate. *Appl. Radiat. Isot.* **1999**, *51*, 411-417.
54. Vaidyanathan, G.; Zalutsky, M. R. No-carrier-added synthesis of meta-[¹³¹I]iodobenzylguanidine. *Appl. Radiat. Isot.* **1993**, *44*, 621-628.
55. Katsifis, A.; Mardon, K.; McPhee, M.; Mattner, F.; Dikic, B.; Ridley, D. Synthesis and evaluation of [¹²³I]labelled analogues of the partial inverse agonist Ro 15-4513 for the study of diazepam-insensitive benzodiazepine receptors. *Nucl. Med. Biol.* **1999**, *26*, 641-649.

56. Wilson, A. A.; Dannals, R. F.; Ravert, H. T.; Frost, J. J.; Wagner, H. N., Jr. Synthesis and biological evaluation of [125I]- and [123I]-4-iododexetimide, a potent muscarinic cholinergic receptor antagonist. *J. Med. Chem.* **1989**, *32*, 1057-1062.
57. Baldas, J.; Bonnyman, J.; Ivanov, Z. Use of high performance liquid chromatography for the structural identification of technetium-99m radiopharmaceuticals at the NCA level. *J. Nucl. Med.* **1989**, *30*, 1240-1248.
58. Chen, Y.; Mehok, A. R.; Mant, C. T.; Hodges, R. S. Optimum concentration of trifluoroacetic acid for reversed-phase liquid chromatography of peptides revisited. *J. Chromatogr. A* **2004**, *1043*, 9-18.
59. Lapi, S. E.; Welch, M. J. A historical perspective on the specific activity of radiopharmaceuticals: what have we learned in the 35years of the ISRC? *Nucl. Med. Biol.* **2013**, *40*, 314-320.
60. Franc, B. L.; Acton, P. D.; Mari, C.; Hasegawa, B. H. Small-animal SPECT and SPECT/CT: important tools for preclinical investigation. *J. Nucl. Med.* **2008**, *49*, 1651-1663.
61. Patton, J. A.; Turkington, T. G. SPECT/CT physical principles and attenuation correction. *J. Nucl. Med. Technol.* **2008**, *36*, 1-10.
62. Yu, F. H.; Yarov-Yarovoy, V.; Gutman, G. A.; Catterall, W. A. Overview of molecular relationships in the voltage-gated ion channel superfamily. *Pharmacol. Rev.* **2005**, *57*, 387-395.
63. Marban, E.; Yamagishi, T.; Tomaselli, G. F. Structure and function of voltage-gated sodium channels. *J. Physiol* **1998**, *508 (Pt 3)*, 647-657.
64. Hodgkin, A. L.; Huxley, A. F. A quantitative description of membrane current and its application to conduction and excitation in nerve. *J. Physiol* **1952**, *117*, 500-544.
65. Craner, M. J.; Hains, B. C.; Lo, A. C.; Black, J. A.; Waxman, S. G. Co-localization of sodium channel Nav1.6 and the sodium-calcium exchanger at sites of axonal injury in the spinal cord in EAE. *Brain* **2004**, *127*, 294-303.
66. Goldin, A. L.; Barchi, R. L.; Caldwell, J. H.; Hofmann, F.; Howe, J. R.; Hunter, J. C.; Kallen, R. G.; Mandel, G.; Meisler, M. H.; Netter, Y. B.; Noda, M.; Tamkun, M. M.; Waxman, S. G.; Wood, J. N.; Catterall, W. A. Nomenclature of voltage-gated sodium channels. *Neuron* **2000**, *28*, 365-368.
67. Tarnawa, I.; Bolcskei, H.; Kocsis, P. Blockers of voltage-gated sodium channels for the treatment of central nervous system diseases. *Recent Pat CNS. Drug Discov.* **2007**, *2*, 57-78.
68. Payandeh, J.; Scheuer, T.; Zheng, N.; Catterall, W. A. The crystal structure of a voltage-gated sodium channel. *Nature* **2011**, *475*, 353-358.
69. Narahashi, T. Tetrodotoxin: a brief history. *Proc. Jpn. Acad. Ser. B Phys. Biol. Sci.* **2008**, *84*, 147-154.

70. Craner, M. J.; Newcombe, J.; Black, J. A.; Hartle, C.; Cuzner, M. L.; Waxman, S. G. Molecular changes in neurons in multiple sclerosis: altered axonal expression of Nav1.2 and Nav1.6 sodium channels and Na⁺/Ca²⁺ exchanger. *Proc. Natl. Acad. Sci. U. S. A* **2004**, *101*, 8168-8173.
71. Goldenberg, M. M. Multiple sclerosis review. *P. T.* **2012**, *37*, 175-184.
72. Trapp, B. D.; Peterson, J.; Ransohoff, R. M.; Rudick, R.; Mork, S.; Bo, L. Axonal transection in the lesions of multiple sclerosis. *N. Engl. J. Med.* **1998**, *338*, 278-285.
73. Craner, M. J.; Lo, A. C.; Black, J. A.; Waxman, S. G. Abnormal sodium channel distribution in optic nerve axons in a model of inflammatory demyelination. *Brain* **2003**, *126*, 1552-1561.
74. Bechtold, D. A.; Miller, S. J.; Dawson, A. C.; Sun, Y.; Kapoor, R.; Berry, D.; Smith, K. J. Axonal protection achieved in a model of multiple sclerosis using lamotrigine. *J. Neurol.* **2006**, *253*, 1542-1551.
75. Craner, M. J.; Damarjian, T. G.; Liu, S.; Hains, B. C.; Lo, A. C.; Black, J. A.; Newcombe, J.; Cuzner, M. L.; Waxman, S. G. Sodium channels contribute to microglia/macrophage activation and function in EAE and MS. *Glia* **2005**, *49*, 220-229.
76. Kohling, R. Voltage-gated sodium channels in epilepsy. *Epilepsia* **2002**, *43*, 1278-1295.
77. Scalmani, P.; Rusconi, R.; Armatura, E.; Zara, F.; Avanzini, G.; Franceschetti, S.; Mantegazza, M. Effects in neocortical neurons of mutations of the Na^v1.2 Na⁺ channel causing benign familial neonatal-infantile seizures. *J. Neurosci.* **2006**, *26*, 10100-10109.
78. Lossin, C.; Rhodes, T. H.; Desai, R. R.; Vanoye, C. G.; Wang, D.; Carniciu, S.; Devinsky, O.; George, A. L., Jr. Epilepsy-associated dysfunction in the voltage-gated neuronal sodium channel SCN1A. *J. Neurosci.* **2003**, *23*, 11289-11295.
79. Ragsdale, D. S.; Avoli, M. Sodium channels as molecular targets for antiepileptic drugs. *Brain Res. Brain Res. Rev.* **1998**, *26*, 16-28.
80. Hoyt, S. B.; London, C.; Wyratt, M. J.; Fisher, M. H.; Cashen, D. E.; Felix, J. P.; Garcia, M. L.; Li, X.; Lyons, K. A.; Euan, M. D.; Martin, W. J.; Priest, B. T.; Smith, M. M.; Warren, V. A.; Williams, B. S.; Kaczorowski, G. J.; Parsons, W. H. 3-Amino-1,5-benzodiazepinones: potent, state-dependent sodium channel blockers with anti-epileptic activity. *Bioorg. Med. Chem. Lett.* **2008**, *18*, 1963-1966.
81. Catterall, W. A.; Cestele, S.; Yarov-Yarovoy, V.; Yu, F. H.; Konoki, K.; Scheuer, T. Voltage-gated ion channels and gating modifier toxins. *Toxicon* **2007**, *49*, 124-141.
82. Catterall, W. A. From ionic currents to molecular mechanisms: the structure and function of voltage-gated sodium channels. *Neuron* **2000**, *26*, 13-25.

83. Eijkelkamp, N.; Linley, J. E.; Baker, M. D.; Minnett, M. S.; Cregg, R.; Werdehausen, R.; Rugiero, F.; Wood, J. N. Neurological perspectives on voltage-gated sodium channels. *Brain* **2012**, *135*, 2585-2612.
84. Schmalhofer, W. A.; Calhoun, J.; Burrows, R.; Bailey, T.; Kohler, M. G.; Weinglass, A. B.; Kaczorowski, G. J.; Garcia, M. L.; Koltzenburg, M.; Priest, B. T. ProTx-II, a selective inhibitor of Nav1.7 sodium channels, blocks action potential propagation in nociceptors. *Mol. Pharmacol.* **2008**, *74*, 1476-1484.
85. Ekberg, J.; Jayamanne, A.; Vaughan, C. W.; Aslan, S.; Thomas, L.; Mould, J.; Drinkwater, R.; Baker, M. D.; Abrahamsen, B.; Wood, J. N.; Adams, D. J.; Christie, M. J.; Lewis, R. J. μ O-conotoxin MrVIB selectively blocks Nav1.8 sensory neuron specific sodium channels and chronic pain behavior without motor deficits. *Proc. Natl. Acad. Sci. U. S. A* **2006**, *103*, 17030-17035.
86. Ragsdale, D. S.; McPhee, J. C.; Scheuer, T.; Catterall, W. A. Molecular determinants of state-dependent block of Na⁺ channels by local anesthetics. *Science* **1994**, *265*, 1724-1728.
87. Hille, B. Local anesthetics: hydrophilic and hydrophobic pathways for the drug-receptor reaction. *J. Gen. Physiol* **1977**, *69*, 497-515.
88. Anger, T.; Madge, D. J.; Mulla, M.; Riddall, D. Medicinal chemistry of neuronal voltage-gated sodium channel blockers. *J. Med. Chem.* **2001**, *44*, 115-137.
89. Williams, B. S.; Felix, J. P.; Priest, B. T.; Brochu, R. M.; Dai, K.; Hoyt, S. B.; London, C.; Tang, Y. S.; Duffy, J. L.; Parsons, W. H.; Kaczorowski, G. J.; Garcia, M. L. Characterization of a new class of potent inhibitors of the voltage-gated sodium channel Nav1.7. *Biochemistry* **2007**, *46*, 14693-14703.
90. Catterall, W. A.; Morrow, C. S.; Daly, J. W.; Brown, G. B. Binding of batrachotoxinin A 20- α -benzoate to a receptor site associated with sodium channels in synaptic nerve ending particles. *J. Biol. Chem.* **1981**, *256*, 8922-8927.
91. Albuquerque, E. X.; Daly, J. W.; Witkop, B. Batrachotoxin: chemistry and pharmacology. *Science* **1971**, *172*, 995-1002.
92. Strichartz, G.; Rando, T.; Wang, G. K. An integrated view of the molecular toxinology of sodium channel gating in excitable cells. *Annu. Rev. Neurosci.* **1987**, *10*, 237-267.
93. Perez-Medina, C.; Patel, N.; Robson, M.; Badar, A.; Lythgoe, M. F.; Arstad, E. Evaluation of a ¹²⁵I-labelled benzazepinone derived voltage-gated sodium channel blocker for imaging with SPECT. *Org. Biomol. Chem.* **2012**, *10*, 9474-9480.
94. Wible, B. A.; Kuryshev, Y. A.; Smith, S. S.; Liu, Z.; Brown, A. M. An ion channel library for drug discovery and safety screening on automated platforms. *Assay. Drug Dev. Technol.* **2008**, *6*, 765-780.
95. Goldin, A. L. Resurgence of sodium channel research. *Annu. Rev. Physiol* **2001**, *63*, 871-894.

96. Pajouhesh, H.; Lenz, G. R. Medicinal chemical properties of successful central nervous system drugs. *NeuroRx*. **2005**, *2*, 541-553.
97. Pardridge, W. M. The blood-brain barrier: bottleneck in brain drug development. *NeuroRx*. **2005**, *2*, 3-14.
98. Cannon, B.; Nedergaard, J. Brown adipose tissue: function and physiological significance. *Physiol Rev*. **2004**, *84*, 277-359.
99. Hill, R. J.; Grant, A. M.; Volberg, W.; Rapp, L.; Faltynek, C.; Miller, D.; Pagani, K.; Baizman, E.; Wang, S.; Guiles, J. W.; . WIN 17317-3: novel nonpeptide antagonist of voltage-activated K⁺ channels in human T lymphocytes. *Mol. Pharmacol*. **1995**, *48*, 98-104.
100. Nguyen, A.; Kath, J. C.; Hanson, D. C.; Biggers, M. S.; Canniff, P. C.; Donovan, C. B.; Mather, R. J.; Bruns, M. J.; Rauer, H.; Aiyar, J.; Lepple-Wienhues, A.; Gutman, G. A.; Grissmer, S.; Cahalan, M. D.; Chandy, K. G. Novel nonpeptide agents potently block the C-type inactivated conformation of Kv1.3 and suppress T cell activation. *Mol. Pharmacol*. **1996**, *50*, 1672-1679.
101. Wanner, S. G.; Glossmann, H.; Knaus, H. G.; Baker, R.; Parsons, W.; Rupprecht, K. M.; Brochu, R.; Cohen, C. J.; Schmalhofer, W.; Smith, M.; Warren, V.; Garcia, M. L.; Kaczorowski, G. J. WIN 17317-3, a new high-affinity probe for voltage-gated sodium channels. *Biochemistry* **1999**, *38*, 11137-11146.
102. Perez-Medina, C.; Patel, N.; Robson, M.; Lythgoe, M. F.; Arstad, E. Synthesis and evaluation of a 125I-labeled iminodihydroquinoline-derived tracer for imaging of voltage-gated sodium channels. *Bioorg. Med. Chem. Lett*. **2013**, *23*, 5170-5173.
103. Bartoo, A. C.; Sprunger, L. K.; Schneider, D. A. Expression and distribution of TTX-sensitive sodium channel alpha subunits in the enteric nervous system. *J. Comp Neurol*. **2005**, *486*, 117-131.
104. Waterhouse, R. N. Determination of lipophilicity and its use as a predictor of blood-brain barrier penetration of molecular imaging agents. *Mol. Imaging Biol*. **2003**, *5*, 376-389.
105. Foster, C. A. VCAM-1/alpha 4-integrin adhesion pathway: therapeutic target for allergic inflammatory disorders. *J. Allergy Clin. Immunol*. **1996**, *98*, S270-S277.
106. Brown, G. C.; Neher, J. J. Inflammatory neurodegeneration and mechanisms of microglial killing of neurons. *Mol. Neurobiol*. **2010**, *41*, 242-247.
107. Ramesh, G.; Philipp, M. T.; Vallieres, L.; MacLean, A. G.; Ahmad, M. Mediators of neuroinflammation. *Mediators. Inflamm*. **2013**, *2013*, 314261.
108. Elices, M. J.; Osborn, L.; Takada, Y.; Crouse, C.; Luhowskyj, S.; Hemler, M. E.; Lobb, R. R. VCAM-1 on activated endothelium interacts with the leukocyte integrin VLA-4 at a site distinct from the VLA-4/fibronectin binding site. *Cell* **1990**, *60*, 577-584.

109. Fabene, P. F.; Navarro, M. G.; Martinello, M.; Rossi, B.; Merigo, F.; Ottoboni, L.; Bach, S.; Angiari, S.; Benati, D.; Chakir, A.; Zanetti, L.; Schio, F.; Osculati, A.; Marzola, P.; Nicolato, E.; Homeister, J. W.; Xia, L.; Lowe, J. B.; McEver, R. P.; Osculati, F.; Sbarbati, A.; Butcher, E. C.; Constantin, G. A role for leukocyte-endothelial adhesion mechanisms in epilepsy. *Nat. Med.* **2008**, *14*, 1377-1383.
110. Serres, S.; Soto, M. S.; Hamilton, A.; McAteer, M. A.; Carbonell, W. S.; Robson, M. D.; Ansorge, O.; Khrapitchev, A.; Bristow, C.; Balathasan, L.; Weissensteiner, T.; Anthony, D. C.; Choudhury, R. P.; Muschel, R. J.; Sibson, N. R. Molecular MRI enables early and sensitive detection of brain metastases. *Proc. Natl. Acad. Sci. U. S. A* **2012**, *109*, 6674-6679.
111. Ley, K.; Huo, Y. VCAM-1 is critical in atherosclerosis. *J. Clin. Invest* **2001**, *107*, 1209-1210.
112. Osborn, L.; Hession, C.; Tizard, R.; Vassallo, C.; Luhowskyj, S.; Chi-Rosso, G.; Lobb, R. Direct expression cloning of vascular cell adhesion molecule 1, a cytokine-induced endothelial protein that binds to lymphocytes. *Cell* **1989**, *59*, 1203-1211.
113. Kleen, J. K.; Holmes, G. L. Brain inflammation initiates seizures. *Nat. Med.* **2008**, *14*, 1309-1310.
114. Biomarkers and surrogate endpoints: preferred definitions and conceptual framework. *Clin. Pharmacol. Ther.* **2001**, *69*, 89-95.
115. McAteer, M. A.; Sibson, N. R.; von zur, M. C.; Schneider, J. E.; Lowe, A. S.; Warrick, N.; Channon, K. M.; Anthony, D. C.; Choudhury, R. P. In vivo magnetic resonance imaging of acute brain inflammation using microparticles of iron oxide. *Nat. Med.* **2007**, *13*, 1253-1258.
116. Hoyte, L. C.; Brooks, K. J.; Nagel, S.; Akhtar, A.; Chen, R.; Mardiguian, S.; McAteer, M. A.; Anthony, D. C.; Choudhury, R. P.; Buchan, A. M.; Sibson, N. R. Molecular magnetic resonance imaging of acute vascular cell adhesion molecule-1 expression in a mouse model of cerebral ischemia. *J. Cereb. Blood Flow Metab* **2010**, *30*, 1178-1187.
117. Duffy, B. A.; Choy, M.; Riegler, J.; Wells, J. A.; Anthony, D. C.; Scott, R. C.; Lythgoe, M. F. Imaging seizure-induced inflammation using an antibody targeted iron oxide contrast agent. *Neuroimage*. **2012**, *60*, 1149-1155.
118. Montagne, A.; Gauberti, M.; Macrez, R.; Jullienne, A.; Briens, A.; Raynaud, J. S.; Louin, G.; Buisson, A.; Haelewyn, B.; Docagne, F.; Defer, G.; Vivien, D.; Maubert, E. Ultra-sensitive molecular MRI of cerebrovascular cell activation enables early detection of chronic central nervous system disorders. *Neuroimage*. **2012**, *63*, 760-770.
119. McAteer, M. A.; Schneider, J. E.; Ali, Z. A.; Warrick, N.; Bursill, C. A.; von zur, M. C.; Greaves, D. R.; Neubauer, S.; Channon, K. M.; Choudhury, R. P. Magnetic resonance imaging of endothelial adhesion molecules in mouse atherosclerosis using dual-targeted microparticles of iron oxide. *Arterioscler. Thromb. Vasc. Biol.* **2008**, *28*, 77-83.

120. Akhtar, A. M.; Schneider, J. E.; Chapman, S. J.; Jefferson, A.; Digby, J. E.; Mankia, K.; Chen, Y.; McAteer, M. A.; Wood, K. J.; Choudhury, R. P. In vivo quantification of VCAM-1 expression in renal ischemia reperfusion injury using non-invasive magnetic resonance molecular imaging. *PLoS. One.* **2010**, *5*, e12800.
121. Paxinos G *The Rat Nervous System: Third Edition*; Burlington: Academic Press: 2004; pp 1167-1202.
122. Shapiro, E. M.; Skrtic, S.; Sharer, K.; Hill, J. M.; Dunbar, C. E.; Koretsky, A. P. MRI detection of single particles for cellular imaging. *Proc. Natl. Acad. Sci. U. S. A* **2004**, *101*, 10901-10906.
123. McAteer, M. A.; Akhtar, A. M.; von Zur, M. C.; Choudhury, R. P. An approach to molecular imaging of atherosclerosis, thrombosis, and vascular inflammation using microparticles of iron oxide. *Atherosclerosis* **2010**, *209*, 18-27.
124. Ye, Q.; Wu, Y. L.; Foley, L. M.; Hitchens, T. K.; Eytan, D. F.; Shirwan, H.; Ho, C. Longitudinal tracking of recipient macrophages in a rat chronic cardiac allograft rejection model with noninvasive magnetic resonance imaging using micrometer-sized paramagnetic iron oxide particles. *Circulation* **2008**, *118*, 149-156.
125. Yang, Y.; Yang, Y.; Yanasak, N.; Schumacher, A.; Hu, T. C. Temporal and noninvasive monitoring of inflammatory-cell infiltration to myocardial infarction sites using micrometer-sized iron oxide particles. *Magn Reson. Med.* **2010**, *63*, 33-40.
126. Liu, T. W.; MacDonald, T. D.; Shi, J.; Wilson, B. C.; Zheng, G. Intrinsically copper-64-labeled organic nanoparticles as radiotracers. *Angew. Chem. Int. Ed Engl.* **2012**, *51*, 13128-13131.
127. Hong, H.; Zhang, Y.; Sun, J.; Cai, W. Molecular imaging and therapy of cancer with radiolabeled nanoparticles. *Nano. Today* **2009**, *4*, 399-413.
128. Ghaghada, K. B.; Badea, C. T.; Karumbaiah, L.; Fettig, N.; Bellamkonda, R. V.; Johnson, G. A.; Annapragada, A. Evaluation of tumor microenvironment in an animal model using a nanoparticle contrast agent in computed tomography imaging. *Acad. Radiol.* **2011**, *18*, 20-30.
129. Staub, J. F.; Coutris, G. A technique for multiple, high-rate blood samplings via an external cannula in rats. *J. Appl. Physiol Respir. Environ. Exerc. Physiol* **1979**, *46*, 197-199.
130. Jain, T. K.; Reddy, M. K.; Morales, M. A.; Leslie-Pelecky, D. L.; Labhasetwar, V. Biodistribution, clearance, and biocompatibility of iron oxide magnetic nanoparticles in rats. *Mol. Pharm.* **2008**, *5*, 316-327.
131. Duncan, J. S.; Sander, J. W.; Sisodiya, S. M.; Walker, M. C. Adult epilepsy. *Lancet* **2006**, *367*, 1087-1100.

132. Cendes, F. Progressive hippocampal and extrahippocampal atrophy in drug resistant epilepsy. *Curr. Opin. Neurol.* **2005**, *18*, 173-177.
133. Perucca, E.; French, J.; Bialer, M. Development of new antiepileptic drugs: challenges, incentives, and recent advances. *Lancet Neurol.* **2007**, *6*, 793-804.
134. Rogawski, M. A.; Loscher, W. The neurobiology of antiepileptic drugs. *Nat. Rev. Neurosci.* **2004**, *5*, 553-564.
135. Pitkanen, A.; Sutula, T. P. Is epilepsy a progressive disorder? Prospects for new therapeutic approaches in temporal-lobe epilepsy. *Lancet Neurol.* **2002**, *1*, 173-181.
136. Reddy, D. S.; Kuruba, R. Experimental models of status epilepticus and neuronal injury for evaluation of therapeutic interventions. *Int. J. Mol. Sci.* **2013**, *14*, 18284-18318.
137. Sadleir, L. G.; Scheffer, I. E. Febrile seizures. *BMJ* **2007**, *334*, 307-311.
138. Vezzani, A.; French, J.; Bartfai, T.; Baram, T. Z. The role of inflammation in epilepsy. *Nat. Rev. Neurol.* **2011**, *7*, 31-40.
139. Cherian, A.; Thomas, S. V. Status epilepticus. *Ann. Indian Acad. Neurol.* **2009**, *12*, 140-153.
140. Gastaut, H. *Dictionary of Epilepsy: Definitions, Part 1*; 1973.
141. Wasterlain, C. G.; Fujikawa, D. G.; Penix, L.; Sankar, R. Pathophysiological mechanisms of brain damage from status epilepticus. *Epilepsia* **1993**, *34 Suppl 1*, S37-S53.
142. Hesdorffer, D. C.; Logroscino, G.; Cascino, G.; Annegers, J. F.; Hauser, W. A. Risk of unprovoked seizure after acute symptomatic seizure: effect of status epilepticus. *Ann. Neurol.* **1998**, *44*, 908-912.
143. Shultz, S. R.; O'Brien, T. J.; Stefanidou, M.; Kuzniecky, R. I. Neuroimaging the epileptogenic process. *Neurotherapeutics.* **2014**, *11*, 347-357.
144. Loscher, W. Critical review of current animal models of seizures and epilepsy used in the discovery and development of new antiepileptic drugs. *Seizure.* **2011**, *20*, 359-368.
145. Curia, G.; Longo, D.; Biagini, G.; Jones, R. S.; Avoli, M. The pilocarpine model of temporal lobe epilepsy. *J. Neurosci. Methods* **2008**, *172*, 143-157.
146. Albala, B. J.; Moshe, S. L.; Okada, R. Kainic-acid-induced seizures: a developmental study. *Brain Res.* **1984**, *315*, 139-148.
147. Maytal, J.; Shinnar, S.; Moshe, S. L.; Alvarez, L. A. Low morbidity and mortality of status epilepticus in children. *Pediatrics* **1989**, *83*, 323-331.

148. Blair, R. E.; Deshpande, L. S.; Holbert, W. H.; Churn, S. B.; DeLorenzo, R. J. Age-dependent mortality in the pilocarpine model of status epilepticus. *Neurosci. Lett.* **2009**, *453*, 233-237.
149. Honchar, M. P.; Olney, J. W.; Sherman, W. R. Systemic cholinergic agents induce seizures and brain damage in lithium-treated rats. *Science* **1983**, *220*, 323-325.
150. Clifford, D. B.; Olney, J. W.; Maniotis, A.; Collins, R. C.; Zorumski, C. F. The functional anatomy and pathology of lithium-pilocarpine and high-dose pilocarpine seizures. *Neuroscience* **1987**, *23*, 953-968.
151. Goffin, K.; Nissinen, J.; Van, L. K.; Pitkanen, A. Cyclicity of spontaneous recurrent seizures in pilocarpine model of temporal lobe epilepsy in rat. *Exp. Neurol.* **2007**, *205*, 501-505.
152. Glien, M.; Brandt, C.; Potschka, H.; Voigt, H.; Ebert, U.; Loscher, W. Repeated low-dose treatment of rats with pilocarpine: low mortality but high proportion of rats developing epilepsy. *Epilepsy Res.* **2001**, *46*, 111-119.
153. Loscher, W. Animal models of epilepsy for the development of antiepileptogenic and disease-modifying drugs. A comparison of the pharmacology of kindling and post-status epilepticus models of temporal lobe epilepsy. *Epilepsy Res.* **2002**, *50*, 105-123.
154. Racine, R. J. Modification of seizure activity by electrical stimulation. II. Motor seizure. *Electroencephalogr. Clin. Neurophysiol.* **1972**, *32*, 281-294.
155. Rossi, A. R.; Angelo, M. F.; Villarreal, A.; Lukin, J.; Ramos, A. J. Gabapentin administration reduces reactive gliosis and neurodegeneration after pilocarpine-induced status epilepticus. *PLoS. One.* **2013**, *8*, e78516.
156. Choy, M.; Cheung, K. K.; Thomas, D. L.; Gadian, D. G.; Lythgoe, M. F.; Scott, R. C. Quantitative MRI predicts status epilepticus-induced hippocampal injury in the lithium-pilocarpine rat model. *Epilepsy Res.* **2010**, *88*, 221-230.
157. Marchi, N.; Tierney, W.; Alexopoulos, A. V.; Puvenna, V.; Granata, T.; Janigro, D. The etiological role of blood-brain barrier dysfunction in seizure disorders. *Cardiovasc. Psychiatry Neurol.* **2011**, *2011*, 482415.
158. Chung, Y. L.; Williams, A.; Beech, J. S.; Williams, S. C.; Bell, J. D.; Cox, I. J.; Hope, J. MRI assessment of the blood-brain barrier in a hamster model of scrapie. *Neurodegeneration.* **1995**, *4*, 203-207.
159. Wolf, O. T.; Dyakin, V.; Patel, A.; Vadasz, C.; de Leon, M. J.; McEwen, B. S.; Bulloch, K. Volumetric structural magnetic resonance imaging (MRI) of the rat hippocampus following kainic acid (KA) treatment. *Brain Res.* **2002**, *934*, 87-96.
160. Niessen, H. G.; Angenstein, F.; Vielhaber, S.; Frisch, C.; Kudin, A.; Elger, C. E.; Heinze, H. J.; Scheich, H.; Kunz, W. S. Volumetric magnetic resonance imaging of functionally relevant structural alterations in chronic epilepsy

- after pilocarpine-induced status epilepticus in rats. *Epilepsia* **2005**, *46*, 1021-1026.
161. Blumenfeld, H. Functional MRI studies of animal models in epilepsy. *Epilepsia* **2007**, *48 Suppl 4*, 18-26.
 162. Dedeurwaerdere, S.; Jupp, B.; O'Brien, T. J. Positron Emission Tomography in basic epilepsy research: a view of the epileptic brain. *Epilepsia* **2007**, *48 Suppl 4*, 56-64.
 163. Kornblum, H. I.; Araujo, D. M.; Annala, A. J.; Tatsukawa, K. J.; Phelps, M. E.; Cherry, S. R. In vivo imaging of neuronal activation and plasticity in the rat brain by high resolution positron emission tomography (microPET). *Nat. Biotechnol.* **2000**, *18*, 655-660.
 164. Mirrione, M. M.; Schiffer, W. K.; Siddiq, M.; Dewey, S. L.; Tsirka, S. E. PET imaging of glucose metabolism in a mouse model of temporal lobe epilepsy. *Synapse* **2006**, *59*, 119-121.
 165. Hong, S. B.; Han, H. J.; Roh, S. Y.; Seo, D. W.; Kim, S. E.; Kim, M. H. Hypometabolism and interictal spikes during positron emission tomography scanning in temporal lobe epilepsy. *Eur. Neurol.* **2002**, *48*, 65-70.
 166. Harhausen, D.; Sudmann, V.; Khojasteh, U.; Muller, J.; Zille, M.; Graham, K.; Thiele, A.; Dyrks, T.; Dirnagl, U.; Wunder, A. Specific imaging of inflammation with the 18 kDa translocator protein ligand DPA-714 in animal models of epilepsy and stroke. *PLoS. One.* **2013**, *8*, e69529.
 167. Scarf, A. M.; Kassiou, M. The translocator protein. *J. Nucl. Med.* **2011**, *52*, 677-680.
 168. Dedeurwaerdere, S.; Callaghan, P. D.; Pham, T.; Rahardjo, G. L.; Amhaoul, H.; Berghofer, P.; Quinlivan, M.; Mattner, F.; Loc'h, C.; Katsifis, A.; Gregoire, M. C. PET imaging of brain inflammation during early epileptogenesis in a rat model of temporal lobe epilepsy. *EJNMMI. Res.* **2012**, *2*, 60.
 169. Koepp, M. J.; Hammers, A.; Labbe, C.; Woermann, F. G.; Brooks, D. J.; Duncan, J. S. ¹¹C-flumazenil PET in patients with refractory temporal lobe epilepsy and normal MRI. *Neurology* **2000**, *54*, 332-339.
 170. Duffy, B. A.; Chun, K. P.; Ma, D.; Lythgoe, M. F.; Scott, R. C. Dexamethasone exacerbates cerebral edema and brain injury following lithium-pilocarpine induced status epilepticus. *Neurobiol. Dis.* **2014**, *63*, 229-236.
 171. Kaminski, R. M.; Rogawski, M. A.; Klitgaard, H. The potential of antiseizure drugs and agents that act on novel molecular targets as antiepileptogenic treatments. *Neurotherapeutics.* **2014**, *11*, 385-400.
 172. Fernandes, M. J.; Dube, C.; Boyet, S.; Marescaux, C.; Nehlig, A. Correlation between hypermetabolism and neuronal damage during status epilepticus induced by lithium and pilocarpine in immature and adult rats. *J. Cereb. Blood Flow Metab* **1999**, *19*, 195-209.

173. Choy, M.; Wells, J. A.; Thomas, D. L.; Gadian, D. G.; Scott, R. C.; Lythgoe, M. F. Cerebral blood flow changes during pilocarpine-induced status epilepticus activity in the rat hippocampus. *Exp. Neurol.* **2010**, *225*, 196-201.
174. Dong, X. X.; Wang, Y.; Qin, Z. H. Molecular mechanisms of excitotoxicity and their relevance to pathogenesis of neurodegenerative diseases. *Acta Pharmacol. Sin.* **2009**, *30*, 379-387.
175. Mark, L. P.; Prost, R. W.; Ulmer, J. L.; Smith, M. M.; Daniels, D. L.; Strottmann, J. M.; Brown, W. D.; Hacein-Bey, L. Pictorial review of glutamate excitotoxicity: fundamental concepts for neuroimaging. *AJNR Am. J. Neuroradiol.* **2001**, *22*, 1813-1824.
176. Woodruff, G. N.; Foster, A. C.; Gill, R.; Kemp, J. A.; Wong, E. H.; Iversen, L. L. The interaction between MK-801 and receptors for N-methyl-D-aspartate: functional consequences. *Neuropharmacology* **1987**, *26*, 903-909.
177. Molinuevo, J. L.; Llado, A.; Rami, L. Memantine: targeting glutamate excitotoxicity in Alzheimer's disease and other dementias. *Am. J. Alzheimers. Dis. Other Demen.* **2005**, *20*, 77-85.
178. Danysz, W.; Parsons, C. G. The NMDA receptor antagonist memantine as a symptomatological and neuroprotective treatment for Alzheimer's disease: preclinical evidence. *Int. J. Geriatr. Psychiatry* **2003**, *18*, S23-S32.
179. Ghasemi, M.; Schachter, S. C. The NMDA receptor complex as a therapeutic target in epilepsy: a review. *Epilepsy Behav.* **2011**, *22*, 617-640.
180. Mathern, G. W.; Pretorius, J. K.; Kornblum, H. I.; Mendoza, D.; Lozada, A.; Leite, J. P.; Chimelli, L. M.; Fried, I.; Sakamoto, A. C.; Assirati, J. A.; Levesque, M. F.; Adelson, P. D.; Peacock, W. J. Human hippocampal AMPA and NMDA mRNA levels in temporal lobe epilepsy patients. *Brain* **1997**, *120* (Pt 11), 1937-1959.
181. Chapman, A. G. Glutamate and epilepsy. *J. Nutr.* **2000**, *130*, 1043S-1045S.
182. Kraus, J. E.; Yeh, G. C.; Bonhaus, D. W.; Nadler, J. V.; McNamara, J. O. Kindling induces the long-lasting expression of a novel population of NMDA receptors in hippocampal region CA3. *J. Neurosci.* **1994**, *14*, 4196-4205.
183. Castel-Branco, M. M.; Alves, G. L.; Figueiredo, I. V.; Falcao, A. C.; Caramona, M. M. The maximal electroshock seizure (MES) model in the preclinical assessment of potential new antiepileptic drugs. *Methods Find. Exp. Clin. Pharmacol.* **2009**, *31*, 101-106.
184. Rowley, H. L.; Marsden, C. A.; Martin, K. F. Generalised seizure-induced changes in rat hippocampal glutamate but not GABA release are potentiated by repeated seizures. *Neurosci. Lett.* **1997**, *234*, 143-146.
185. Sherwin, A. L. Neuroactive amino acids in focally epileptic human brain: a review. *Neurochem. Res.* **1999**, *24*, 1387-1395.

186. Viviani, B.; Bartesaghi, S.; Gardoni, F.; Vezzani, A.; Behrens, M. M.; Bartfai, T.; Binaglia, M.; Corsini, E.; Di, L. M.; Galli, C. L.; Marinovich, M. Interleukin-1beta enhances NMDA receptor-mediated intracellular calcium increase through activation of the Src family of kinases. *J. Neurosci.* **2003**, *23*, 8692-8700.
187. Wang, S.; Cheng, Q.; Malik, S.; Yang, J. Interleukin-1beta inhibits gamma-aminobutyric acid type A (GABA(A)) receptor current in cultured hippocampal neurons. *J. Pharmacol. Exp. Ther.* **2000**, *292*, 497-504.
188. Owens, J.; Tebbutt, A. A.; McGregor, A. L.; Kodama, K.; Magar, S. S.; Perlman, M. E.; Robins, D. J.; Durant, G. J.; McCulloch, J. Synthesis and binding characteristics of N-(1-naphthyl)-N'-(3-[(125)I]-iodophenyl)-N'-methylguanidine ([125I]-CNS 1261): a potential SPECT agent for imaging NMDA receptor activation. *Nucl. Med. Biol.* **2000**, *27*, 557-564.
189. Owens, J.; Wyper, D. J.; Patterson, J.; Brown, D. R.; Elliott, A. T.; Teasdale, G. M.; McCulloch, J. First SPET images of glutamate (NMDA) receptor activation in vivo in cerebral ischaemia. *Nucl. Med. Commun.* **1997**, *18*, 149-158.
190. Stone, J. M.; Erlandsson, K.; Arstad, E.; Bressan, R. A.; Squassante, L.; Teneggi, V.; Ell, P. J.; Pilowsky, L. S. Ketamine displaces the novel NMDA receptor SPET probe [(123)I]CNS-1261 in humans in vivo. *Nucl. Med. Biol.* **2006**, *33*, 239-243.
191. Bowery, N. G.; Wong, E. H.; Hudson, A. L. Quantitative autoradiography of [3H]-MK-801 binding sites in mammalian brain. *Br. J. Pharmacol.* **1988**, *93*, 944-954.
192. Suzuki, T.; Yamamoto, T.; Hori, T.; Abe, S.; Moroji, T.; Shiraishi, H.; Ito, T.; Ho, I. K. Quantitative autoradiographic localization of [3H]3-OH-PCP (1-(1(3-hydroxyphenyl)cyclohexyl)piperidine) binding sites in rat brain. *Brain Res. Bull.* **1995**, *37*, 431-435.
193. Knol, R. J.; de, B. K.; van Eck-Smit, B. L.; Pimlott, S.; Wyper, D. J.; Booij, J. In vivo [(123)I]CNS-1261 binding to D-serine-activated and MK801-blocked NMDA receptors: A storage phosphor imaging study in rats. *Synapse* **2009**, *63*, 557-564.
194. Choy, M.; Wells, J. A.; Thomas, D. L.; Gadian, D. G.; Scott, R. C.; Lythgoe, M. F. Cerebral blood flow changes during pilocarpine-induced status epilepticus activity in the rat hippocampus. *Exp. Neurol.* **2010**, *225*, 196-201.
195. Dube, C.; Boyet, S.; Marescaux, C.; Nehlig, A. Progressive metabolic changes underlying the chronic reorganization of brain circuits during the silent phase of the lithium-pilocarpine model of epilepsy in the immature and adult Rat. *Exp. Neurol.* **2000**, *162*, 146-157.
196. Chapman, A. G. Glutamate receptors in epilepsy. *Prog. Brain Res.* **1998**, *116*, 371-383.
197. Millan, M. H.; Chapman, A. G.; Meldrum, B. S. Extracellular amino acid levels in hippocampus during pilocarpine-induced seizures. *Epilepsy Res.* **1993**, *14*, 139-148.

198. Obrenovitch, T. P.; Urenjak, J.; Zilkha, E. Evidence disputing the link between seizure activity and high extracellular glutamate. *J. Neurochem.* **1996**, *66*, 2446-2454.
199. Hamoudeh, M.; Fessi, H. Preparation, characterization and surface study of poly-epsilon caprolactone magnetic microparticles. *J. Colloid Interface Sci.* **2006**, *300*, 584-590.
200. Zhu, D.; White, R. D.; Hardy, P. A.; Weerapreeyakul, N.; Sutthanut, K.; Jay, M. Biocompatible nanotemplate-engineered nanoparticles containing gadolinium: stability and relaxivity of a potential MRI contrast agent. *J. Nanosci. Nanotechnol.* **2006**, *6*, 996-1003.
201. Chen, H. H.; Le, V. C.; Qiu, B.; Du, X.; Ouwerkerk, R.; Leong, K. W.; Yang, X. MR imaging of biodegradable polymeric microparticles: a potential method of monitoring local drug delivery. *Magn Reson. Med.* **2005**, *53*, 614-620.
202. McGinnity, C. J.; Hammers, A.; Riano Barros, D. A.; Luthra, S. K.; Jones, P. A.; Trigg, W.; Micallef, C.; Symms, M. R.; Brooks, D. J.; Koeppe, M. J.; Duncan, J. S. Initial evaluation of 18F-GE-179, a putative PET Tracer for activated N-methyl D-aspartate receptors. *J. Nucl. Med.* **2014**, *55*, 423-430.
203. Watthey, J. W.; Stanton, J. L.; Desai, M.; Babiarz, J. E.; Finn, B. M. Synthesis and biological properties of (carboxyalkyl)amino-substituted bicyclic lactam inhibitors of angiotensin converting enzyme. *J. Med. Chem.* **1985**, *28*, 1511-1516.
204. Jackso, R. F. W.; Moore, R. J.; Dexter, C. S.; Elliot, J.; Mowbray, C. E. Concise Synthesis of Enantiomerically Pure Phenylalanine, Homophenylalanine, and Bishomophenylalanine Derivatives Using Organozinc Chemistry: NMR Studies of Amino Acid-Derived Organozinc Reagents. *J. Org. Chem.* **1998**, *63*, 7875-7884.
205. Hoyt, S. B.; Parsons, W. H.; London, C.; OK, D. Benzazepinones as Sodium Channel Blockers. PCT/US2007/013202[WO2007/145922 A2]. 21-12-2007.
Ref Type: Patent
206. Hanes, R. E.; Ellingsworth, E. C.; Griffin, S. T.; Rogers, R. D.; Bartsch, R. A. Polybenzocrown ethers: synthesis by cesium-assisted cyclization and solid-state structures. *ARKIVOC* **2010**, *7*, 217-237.
207. Lundin, M.; Lundin, J.; Helin, H.; Isola, J. A digital atlas of breast histopathology: an application of web based virtual microscopy. *J. Clin. Pathol.* **2004**, *57*, 1288-1291.
208. Tetz, L. M.; Rezk, P. E.; Ratcliffe, R. H.; Gordon, R. K.; Steele, K. E.; Nambiar, M. P. Development of a rat pilocarpine model of seizure/status epilepticus that mimics chemical warfare nerve agent exposure. *Toxicol. Ind. Health* **2006**, *22*, 255-266.
209. Fischer, A. H.; Jacobson, K. A.; Rose, J.; Zeller, R. Hematoxylin and eosin staining of tissue and cell sections. *CSH. Protoc.* **2008**, *2008*, db.

